UNIVERSITY OF SOUTHAMPTON

Dynamic Modelling and Computed Torque Control of Flexible-Joint Thrust Vector Control System

by

Ahmet Aydogan

A thesis for the degree of
Doctor of Philosophy

in the

Faculty of Engineering and Physical Sciences
School of Electronics and Computer Science

April 2023

UNIVERSITY OF SOUTHAMPTON

ABSTRACT

FACULTY OF ENGINEERING AND PHYSICAL SCIENCES
SCHOOL OF ELECTRONICS AND COMPUTER SCIENCE

Doctor of Philosophy

by Ahmet Aydogan

Thrust Vector Control (TVC) is one means of controlling air vehicles and spacecraft to follow a desired flight path. Of the currently available systems, the Flexible-Joint Thrust Vector Control (FJ-TVC) is currently the most feasible, especially for space applications. Reasons for this include its longer lifespan, increased energy efficiency, less thrust loss and lower maintanance costs. Often, the dynamics of these systems are modeled using an universal gimbal joint mechanism that neglects uncertainties such as the displacement of the pivot point of the nozzle in the vertical motion. The research reported in this thesis first gives a new approach to the dynamic modelling of FJ-TVC systems that includes one more degree of freedom compared to the conventional models and hence enables the flexible joint structure to move in the vertical direction in addition to the rotational motion of the nozzle in the yaw and pitch-axes. Then the classical control structure is designed and also an alternative that includes Computed Torque Control Law (CTCL) action. It is confirmed, however, that these designs lack robustness even though such a control law gives better performance than the classical control law arrangement. This motivates the last major control law development in this thesis in the form of an $\mathcal{H}_\infty$ law with norm bounded model uncertainty where the Monte-Carlo based simulations are used to construct the numerical representation of the uncertainties. Finally, an experimental system is designed, built and used to verify the predicted performance of the designs.

Contents

List of Figures

List of Tables

Nomenclature

Capital Roman Letters

$C(\cdot)$	Coriolis/centripetal matrix
$F(\cdot)$	Friction matrix in joint space dynamics
F_y, F_z	Applied forces on yaw and pitch axes, respectively
$G(\cdot)$	Gravity vector
$K_f(\cdot)$	Feedback matrix
$L(\cdot)$	Lagrangian equation
$M(\cdot)$	Mass matrix
$T(\cdot)$	Kinetic energy of the system
$V(\cdot)$	Potential energy of the system

Lowercase Roman Letters

d	Vertical displacement of the nozzle
$e(\cdot)$	Tracking error
k_i	Stiffness coefficient of i-th spring
m_i	Mass of i-th link
$r(.)$	Position vector of the nozzle
$u(\cdot)$	Input signal
$q(\cdot)$	Generalised coordinate
$x(\cdot)$	State vector

Greek Letters

$\bar{\sigma}(\cdot)$	Maximum singular value
θ_y, θ_z	Angular displacement of the nozzle in yaw and pitch axes
τ_d	Disturbance torque
τ_i	External torque acting on the i-th generalised coordinate

Miscellaneous

$\cdot \succ$	Symmetric positive definite property
$\cdot \prec$	Symmetric negative definite property
$\|\cdot\|_\infty$	Infinity norm

Acronyms

ABS	Acrylonitrile Butadiene Styrene
BA	Bees Algorithm
BLDC	Brushless DC
CoG	Centre of Gravity
CTCL	Computed Torque Control Law
DoF	Degrees of Freedom
ECU	Electronic Control Unit
FJ-TVC	Flexible-Joint Thrust Vector Control
GJ-TVC	Gimbal-Joint Thrust Vector Control
GUI	Graphical User Interface
HWIL	Hardware-in-the-Loop
I/O	Input Output
IMU	Inertial Measurement Unit
KYP	Kalman Yakubovich Popov
LMI	Linear Matrix Inequality
LTI	Linear Time Invariant
MIMO	Multiple Input Multiple Output
MOSFET	Metal Oxide Semiconductor Field Effect Transistor
PD	Proportional Derivative
PD-CTCL	Proportional Derivative - Computed Torque Control Law
PI	Proportional Integral
PID	Proportional Integral Derivative
PID-BB	PID Controller with Phase-Lead Compensator and Bang-Bang Control
PWM	Pulse Width Modulation
QEP	Quadrature Encoder Pulse
RMS	Root Mean Square
TVC	Thrust Vector Control

Declaration of Authorship

I, **Ahmet Aydogan**, declare that the thesis entitled

Dynamic Modelling and Computed Torque Control of Flexible-Joint Thrust Vector Control System

and the work presented in the thesis are both my own, and have been generated by me as the result of my own original research.

I confirm that:

- this work was done wholly or mainly while in candidature for a research degree at this University;
- where any part of this thesis has previously been submitted for a degree or any other qualification at this University or any other institution, this has been clearly stated;
- where I have consulted the published work of others, this is always clearly attributed;
- where I have quoted from the work of others, the source is always given. With the exception of such quotations, this thesis is entirely my own work;
- I have acknowledged all main sources of help;
- where the thesis is based on work done by myself jointly with others, I have made clear exactly what was done by others and what I have contributed myself;
- Some of this work has been published before submission can be found in introduction.

Signed:.....

Date:.....

Acknowledgements

I would like to express my great appreciation to Prof. Eric Rogers for his valuable and constructive suggestions during the planning and development of this research work. His willingness to give his time so generously has been very much appreciated.

I extend my gratitude to Roketsan Inc. company and its executives who allowed me to carry out this research, not only supporting financially, but also for encouraging to guide and keep me on the correct path. I would also like to thank my dear friend and colleague, Dr. Ozgur Hasturk, for his invaluable guidance.

Finally, I would like to express my deep and sincere gratitude to my dear wife Dr. Tugba Aydogan and my family for their continuous and unparalleled love, help and support.

To my family.

Thank you for your continued love and support...

Chapter 1

Introduction

This chapter gives a review of the Thrust Vector Control (TVC) systems and discusses the significant features of a Flexible-Joint TVC (FJ-TVC) type which is the subject of increasing interest. Particular attention is given to currently open problems whose solution would greatly advance progress to applications. The aims and objectives of the thesis are defined. Moreover, the original research contributions are discussed. Lastly, the thesis structure is given.

1.1 Motivation

All aircraft, spacecraft and launcher systems require an orientation to follow a desired flight path, where depending on the application, different control methods are developed to maneuver the vehicles. The most common control method for air vehicles is implemented using aerodynamic surfaces. By deflection of these surfaces, a moment is applied about the centre of gravity of the vehicle, with the aim of achieving the orientation required for the desired angle of attack. However, the aerodynamic surfaces are less effective as the performance requirements, such as high agility and maneuverability increase. Moreover, the control capability of these surfaces reduces at high altitudes because of the reduction in air density. Also, exo-atmospheric vehicles require high control capability in the space environment. It is for these systems that the TVC method is widely recognised as the best solution (Lazić and Ristanović, 2007).

TVC systems consist of many different methods and examples are generally divided into two groups as movable or fixed nozzle. In both methods, thrust vector, which is generated by supersonic flow, applies a moment around the centre of gravity of the vehicle depending on the thrust vector angle, θ, as shown in Figure 1.1. The general objective of the TVC methods is to make an aircraft follow a specified trajectory.

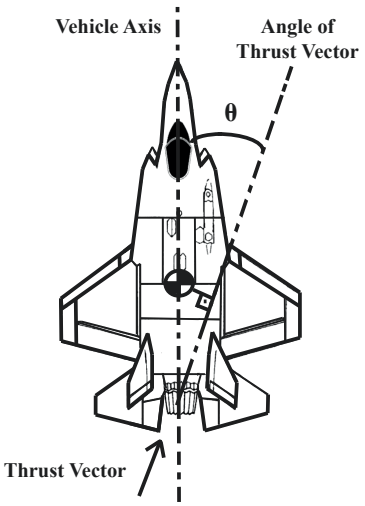

FIGURE 1.1: The control of thrust vector (Aircav, 2008)

According to the working principle, TVC systems can also be classified as (1) the manipulation of exhaust gas by mechanical deflectors, (2) the changing of internal pressure distribution in the nozzle by injecting secondary fluid, (3) the steering of the nozzle by actuators.

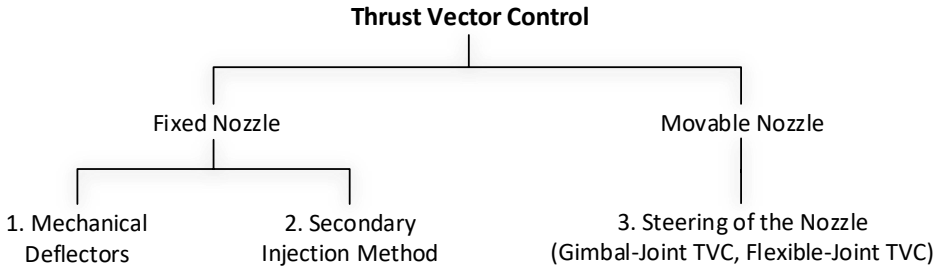

FIGURE 1.2: The classification of TVC systems

Among the methods enumerated above, the first includes heat resistant mechanical deflectors to change the direction of exhaust gas, i.e., the direction of thrust vector. However, the lifespan of mechanical deflectors is limited by its resistance to the exposed supersonic flow and therefore is not recommended for systems that require high operation time, such as satellite systems and spacecraft. Additionally, mechanical deflectors increase the drag force and hence cause a decrease on the net thrust force (Söğütcü and Sümer, 2019).

The second method for TVC systems is based on the injection of secondary fluid into the nozzle to change the internal pressure distribution and hence the exhaust gas flow by generating chemical reactions and shock waves (Schaefermeyer, 2011). In this working principle the secondary fluid reservoir must be present to supply the required flow.

However, the control of chemical reactions is a complicated process as it generates an unsteady flow inside the nozzle and contributes to the exhaust flow. Another disadvantage of this method is the significant loss of thrust.

Lastly, the movable nozzle provides a longer lifespan and is a widely accepted system with minimal thrust loss and robust controlling techniques. The Gimbal-Joint TVC (GJ-TVC) and FJ-TVC methods are amongst the most commonly used systems. For specific fields such as space applications, where longer lifespan, less maintenance and energy efficiency are essential, both GJ-TVC and FJ-TVC are the preferred systems.

When low amounts of steering angle are required, FJ-TVC offers a high-power efficiency. The reason is due to the lower torque requirements for paths with minimal steering. Conversely, GJ-TVC demands consistent torque levels for both high and low steering, therefore, overall power consumption is always greater when less steering is required. Additionally, GJ-TVC is used when the liquid propellant engine is the case where the injector, combustion chamber and nozzle are gimballed, however, the tank for the liquid propellant and oxidizer are fixed to the chasis of the vehicle and connected to the injector by flexible pipes. If the solid propellant is used in the system, then, FJ-TVC is prefered as the gimballing of the components in GJ-TVC requires great amount of torque for steering. As a result, FJ-TVC systems are of great interest due to negligible thrust loss, longer operational lifespan, minimal maintenance and greater energy efficiency (subject to minimal steering, maximum $\pm 10^{\circ}$).

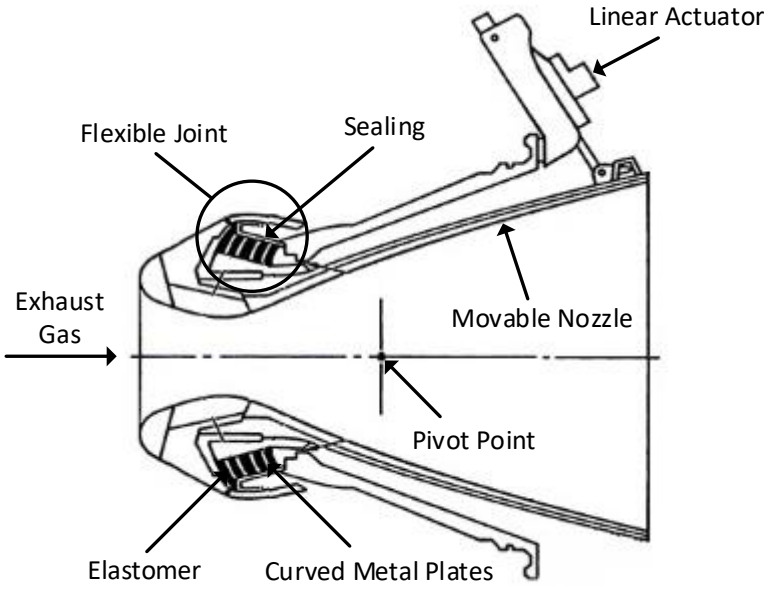

FIGURE 1.3: The section view of the FJ-TVC system (Prescott and Macocha, 1996).

In Figure 1.3, the section view of an FJ-TVC system is given. Even though the engine which supplies the exhaust gas through the nozzle is not shown in the figure, the other sub-components, such as movable nozzle, flexible-joint including elastomer material and curved metal plates, sealing and linear actuators are shown. The movable nozzle is used

to accelerate hot exhaust gas and thereby generates the thrust force. The magnitude of the thrust force depends on the mass flow rate through the engine, the exit velocity of the flow, and the pressure at the exit of the engine. The most crucial part of this system is known as the flexible-joint mechanism since it is made of moulded elastomer structure reinforced with curved metal plates and provides the rotational motion of the nozzle. Although the flexible joint mechanism is covered by a sealing metarial to preserve it against severe environmental conditions, the literature review given in the next chapter concludes that its characteristic behaviour is variable under different loads and environmental changes (Lampani et al., 2012). One of the example is the relocation of the pivot point depending on the motor pressure and hence causing misalignments issues on the nozzle angle which negatively affects the trajectory tracking control of the vehicle. There are also some uncertainties due to the aerodynamic flows, which are considered as internal and external aerodynamic torques exposed to inner and outer surfaces of the nozzle. However, the internal torque, caused by the asymmetric flow through the movable nozzle has a minor effect on the controlling of the nozzle angle when compared to the misalignment issues arising from the pivot point translation. Additionally, the external aerodynamic torque can be minimised by a structural component, i.e., exit cone, which is fixed to the chasis of the air vehicle and covers the nozzle from the external aerodynamic flows (Elegante and Bowman, 2012).

Although the problems explained above have been previously discussed in (Lampani et al., 2012; Chunguang et al., 2020), the literature on accounting for these effects is fragmented. Most publications on TVC systems assume a universal joint mechanism, see (Li et al., 2011; Yu and Shu, 2017), which is a simplification that takes no account of the model uncertainties in the vertical motion of the nozzle. Therefore, the designs in the literature eliminate the translational motion of the nozzle and the design of robust controllers has not been considered.

Additionally, the performance of a controller is another crucial concern where an application requires high precision, speed and efficiency, simultaneously. Hence, this research uses a model-based design, the Computed Torque Control Law (CTCL) method, to meet the requirements of the FJ-TVC system. This control strategy is mainly used for high precision robots operating within, for example, the field of robot-assisted surgery, assembly of critical electronic components, disposal of toxic materials and handling of nuclear material. The main advantage of the CTCL method is that if the dynamic model of the system is known to be reasonably accurate, then the nonlinearities in the system model can be well compensated, thereby achieving excellent tracking control (Shang et al., 2012).

1.2 Aims and Objectives

The overall objective of this research aim is to develope a prototype test-rig for an FJ-TVC system that replicates the misalignments having crucial effects on the dynamic model and controller design. This experimental test-rig will then provide the basis for the performance evaluation of the developed controller designs. The main objectives to achieve this goal are:

- Defining and evaluating modelling uncertainties due to the misalignments existing in the FJ-TVC system that forms the design criteria of the prototype test-rig. The uncertainties that will have a crucial effect over the controller performance will be included in the prototype design, i.e., the translational motion of the nozzle in flight axes.;
- Deriving mathematical model of the test-rig that covers crucial dynamic behaviours of the FJ-TVC system.;
- Designing conventional and model-based controllers in the MATLAB® Simulink environment that gives tracking performance of the controllers based on implemented specified uncertainties.;
- Developing an experimental test setup that includes the test-rig and necessary electronic equipment, and provides a test interface for the benchmarking of the different controller designs for different positions of the pivot point.; and
- Verifying simulation-based test results with the experimental tests.

1.3 Research Contributions

The research considers a prototype test-rig for an FJ-TVC system, derives its dynamic model and designs model-based controllers to achieve excellent tracking control performance. The results obtained are based on developing and integrating improvements in the real-time hardware and custom-design FJ-TVC prototype. An experimental system is used to assess the performance of the developed control methods available within this specific field. Current technological developments such as the dSPACE real-time HardWare-In-the-Loop (HWIL) system are integrated within this experiment.

Specific contributions are summarised as follows:

- **An Overview of the FJ-TVC System:** There are several methods for the controlling of thrust vector which are classified as movable and fixed nozzle in TVC systems. This research, firstly, gives an overview of these varieties. Then, it

specifically focuses on the FJ-TVC system as it has a number of advantages over the other approaches to the TVC method, which are discussed in detail. Also the gaps in the current literature are identified, including the current status on robust control design and experimental validation (Li et al., 2011; Yu and Shu, 2017).

- **A Derivation of the Dynamic Modelling of the FJ-TVC System Test-Rig:** It has been concluded from the literature review that the dynamic models developed for the FJ-TVC system neglect some important dynamic behaviour of the system which are mainly the nozzle misalignments due to the displacement of pivot point and parametric uncertainties in the plant model. Since the studies in the literature have not been experimentally tested, their control performance with an inaccurate dynamic model have not been verified. Therefore, one of the contributions of this thesis is to derive the mathematical model of the FJ-TVC system test-rig including previously neglected terms with the aim of improved control performance.

- **A Custom Design of the FJ-TVC Prototype Test-Rig:** An experimental setup is an important aspect of the performance verification process. Therefore, a prototype test-rig of the FJ-TVC system is developed within this research which is a unique design for this specific field. In the prototype design, instead of using a combination of molded elastomer and curved metal plates for the flexible-joint mechanism, equally distributed linear springs are used to have similar counter loads. Most of the parts in the prototype were manufactured by a 3D-printer. However, parts that require precise finish and are exposed to heavy loads are manufactured in aluminium using a Computer Numerical Control (CNC) machine. This experimental prototype also includes various sensors such as potentiometer, encoder, current sensor and laser displacement sensor to collect the data for the benchmarking of test results from the developed controllers. Additionally, a real-time HWIL system has been set up to update the controller parameters online and observe the results more effectively.

- **An Implementation of the Conventional Control Algorithm:** The main core of this research is to develop a controller that has excellent trajectory tracking performance for the FJ-TVC test-rig. When the conventional control algorithms are reviewed, one of the example developed for the GJ-TVC system come into prominence, which is the combination of Proportional plus Integrator plus Derivative controller with phase-lead compensator and Bang-Bang control (PID-BB), see Li et al. (2011). The phase-lead compensator in this controller improves the system's stability and decreases the response time. Additionally, the bang-bang controller is used to enhance the rapidity of the dynamic response of the GJ-TVC system. Due to the adequate performance of the controller over the GJ-TVC

system, this study implements the same approach for the FJ-TVC system as a conventional control algorithm.

- **An Implementation of the Model-Based Controller Design:** As a model-based controller, the CTCL method is developed which is a very powerful control technique for the robotic systems and ensures globally asymptotic stability. If the mathematical model of a system is known, it enables the achievement of excellent tracking control. The significant advantage of the CTCL method is that it evaluates the nonlinear inverse dynamics equations of the system. Therefore, the actuator applies the required force/torque depending on the evaluated inverse dynamics equations, which, therefore, gives very precise and reliable output when the system dynamics derived accurately. Although it is known that model based controllers are quite successful for systems that have an accurate dynamic model, an implementation of the CTCL method for the FJ-TVC test-rig is the first study within this research.

- **An Improvement of Control Performance:** This research also benchmarks the test results from the developed controllers. The implementation of a CTCL-based cascade control system on the prototype requires various processes to increase the control performance. Some practical approaches such as Monte-Carlo simulation are used to improve the control performance of the system by modelling the effects of the uncertainties. Additionally, the Bees algorithm is used for the tuning of parameters in the controller to reduce the over-shoot, steady-state error and rising time. The Bees algorithm is capable of solving many complex multi-variable optimisation problems in more robust and efficient ways than existing algorithms (Pham et al., 2005). Therefore, an improved trajectory tracking control performance is achieved. Experimental tests are also conducted and the test results are verified.

These contributions indicate that the FJ-TVC system is an effective way for the trajectory tracking control of the launchers and spacecrafts when the uncertainties, such as the displacement of pivot point, are included in the dynamic modelling of the system and the controller design. Early results from this research are reported in the following conference papers:

- Aydogan, A., Hasturk, O. and Rogers, E., (2018) Dynamic modeling and computed torque control of flexure jointed TVC systems. *ASME Dynamic Systems and Control Conference*, Atlanta, Georgia, USA, doi:10.1115/DSCC2018-8987.

- Aydogan, A., Hasturk, O. and Rogers, E., (2019) Robust $\mathcal{H}_\infty$ computed torque control of flexible joint TVC systems. *IFAC Symposiom on Automatic Control in Aerospace*, Cranfield, UK, 52:454-459, doi:10.1016/j.ifacol.2019.11.285.

1.4 Thesis Structure

This thesis is structured as follows:

In Chapter 2, a general review of the TVC method is given, and the motivation of this research is described by reviewing the relevant studies of the FJ-TVC system. Moreover, the significant features of the FJ-TVC system are reported by considering its advantages and disadvantages. Additionally, the related studies with the FJ-TVC system are discussed and hence the current gaps in this specific field are defined.

Chapter 3 introduces the commonly known dynamic modelling methods. Then, it develops a new approach to dynamic modelling of the FJ-TVC system which includes previously neglected important terms. The mathematical model is derived by using Lagrange's energy equation method. This chapter also gives the differences between the conventional and developed dynamic modelling of the FJ-TVC system.

Chapter 4 develops three different control methods for the FJ-TVC system, which can be grouped as conventional and model-based controllers. The developed conventional controller is PID-BB, whereas model-based controllers are PD-CTCL and robust $\mathcal{H}_\infty$-CTCL, respectively. The advantages, limitations, and up-to-date research based on these control methods are discussed in this chapter.

In Chapter 5, MATLAB/Simulink implementation results are given from the control of trajectory tracking of the FJ-TVC system. Firstly, the system description and requirements are defined, then the previously developed controllers in Chapter-4 are designed in the MATLAB/Simulink environment. As a next step, simulation studies are carried out with two different system models where the initial model uses the nominal plant model, whereas the second model includes the uncertainties in addition to nominal plant model. The simulation results are discussed in detail.

Chapter 6 gives the design steps for developing the FJ-TVC experimental test system. This includes the design of the FJ-TVC prototype test-rig matching the dynamic behaviour of the flexible-joint mechanism. Additionally, the experimental test setup within the real-time HWIL system and feedback sensors are explained, including the calibration processes in the MATLAB/Simulink model.

In Chapter 7, experimental test results are given and discussed for the initial assessment of the controllers against core system requirements. Moreover, some improvements on the experimental tests are reported which are the tuning of the controller parameters by using the Bees algorithm and the further Monte-Carlo simulations for the modelling of the uncertainties. Additionally, benchmarking of the experimental test results are discussed.

In Chapter 8, the conclusions of this research are drawn. Additionally, possible future research areas are given.

Chapter 2

Literature Review of the TVC System

The previous chapter provides a brief introduction on TVC methods and its trending FJ-TVC type. This chapter additionally gives an extensive overview of current knowledge about the same, allowing to identify relevant methods, and gaps in the existing research. The motivation for research in the FJ-TVC systems are also discussed in this chapter.

2.1 What is Thrust Vector Control?

The TVC method, in principle, uses the thrust generated by the combustion of propellant in a chamber. As a result of combustion, exhaust gas is produced which is then used to control the vehicle using manipulators that are perpendicular to the thrust vector, or steering the propulsion system to keep the vehicle on its desired flight path (Jiméneze and Icaza, 2000; Ensworth, 2013).

Aircraft in many applications require a suitably robust controller to follow flight paths that includes high maneuvers, and TVC undertakes a crucial role in the orientation of these vehicles in addition to thrust force. As seen in Figure 2.1, the vehicle has a total of 6-Degrees of Freedom (DoF) where 3-DoF are translational and the other DoF are rotational motion about x-, y- and z-axes, termed as roll, pitch and yaw. Roll is the rotation of the vehicle about its longitudinal axis, pitch is the rotation of the vehicle about the new y-axis when it climbs up or down and yaw is its rotation about the new z-axis. This is the reference coordinate system used in the thesis. The same coordinate system established over the nozzle is given in Section 2.2 where the displacement of pivot point and its affect over the misalignment of the nozzle are discussed.

TVC is only efficient when the propulsion system operates and generates an exhaust gas output. For instance, if a rocket does not have any propulsion system for combustion

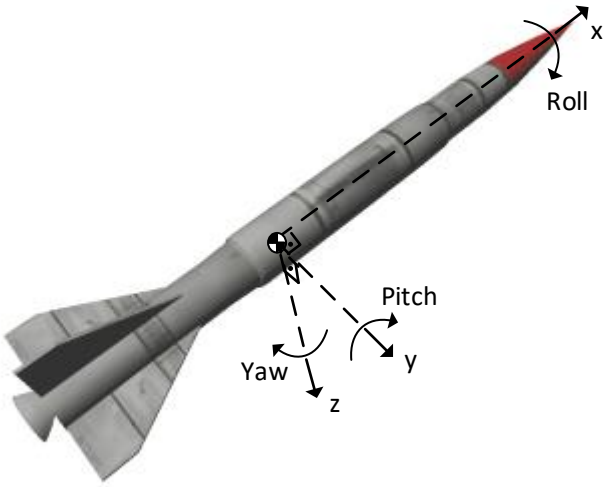

FIGURE 2.1: The reference coordinate system of the vehicle (Althaffathan, 2019)

process, TVC cannot be used. For such systems, a separate mechanism is required to achieve control over its attitude. An example of the same is aerodynamic fins, which are ideal for controlling most air vehicles, including anti-aircraft missiles, air-to-surface missiles, and weather rockets. Although aerodynamic control surfaces provide additional drag, their effectiveness in terms of vehicle weight, hinge moment, and actuating power consumption has advantages over other flight control methods. In general, there is a relationship between system requirements and control methods. If the system is operating in a space environment or in a case of high altitudes where the dynamic pressure is too low or the performance requirements, such as high agility and maneuverability requirements increase, then TVC plays a major role.

TVC falls under two headings, fixed and movable nozzle systems, which are considered in turn next.

2.1.1 Fixed Nozzle TVC Systems

Fixed nozzle TVC systems implement the computed control action using either mechanical deflectors or the injection of secondary fluid. Even though both methods deflect the direction of supersonic flow, their approach is different in practice. The mechanical deflector method includes moving mechanical parts situated at the exit point of the nozzle to manipulate the supersonic gas, and these parts must be resistant to heat for a longer lifespan.

Secondary fluid injection is another technique used for fixed nozzle TVC systems. It uses asymmetric wall forces caused by lateral injection of a fluid into the divergent portion of the nozzle.

Both methods have high thrust loss and short lifespan when compared to fixed nozzle TVC systems. The main cause of the thrust loss is the manipulation of exhaust gas and the reduction of its effectiveness. The reason for such short lifespan is due to the mechanical deflector being directly exposed to supersonic flow. Additionally, the amount of fluid reservoir provided for the injection of secondary fluid limits its control capability.

2.1.1.1 Mechanical Deflectors

Mechanical deflector methods have three different forms i.e., jet vane, jet tab and jet deflector as illustrated in Figure 2.2.

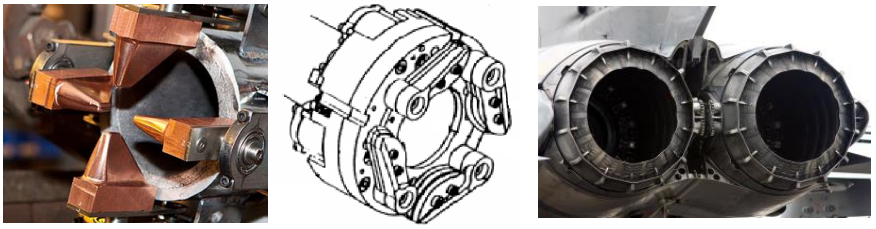

FIGURE 2.2: Mechanical deflector methods, jet vane (wired.com, 2019), jet tab (Facciano et al., 1999) and jet deflector (Pictures, 2019)

Amongst these devices, the jet vane is the most common way of controlling thrust vector in missile systems. The most common substance used within a jet vane is graphite due to its high resistance to extreme temperatures. It has a similar shape to an aerodynamic wing surface and is assembled to the exit point of a nozzle. This is then rotated on its axis to manipulate thrust flow according to the flight path of a vehicle. In this situation the drag force can reach up to 2 to 5% as the deflection of the jet vane increases. Furthermore, this technique was also used by both the German V-2 missile and Soviet Union Scud missile see Figure 2.3.

FIGURE 2.3: Jet vane mechanism used in German V-2 and Scud missiles, (Wikipedia, 2021b,a)

The second form of mechanical deflector is known as a jet tab. It is a compact mechanism for the TVC systems and outputs low torque compared to other techniques. Despite its

straightforward design for low-area-ratio nozzles, thrust loss is too high when the tabs are in the full open position. Consequently, jet tab positions are mostly operated at very small angles where thrust loss is kept to a minimal level. An example of its use is the Tomahawk cruise missile as shown in Figure 2.4.

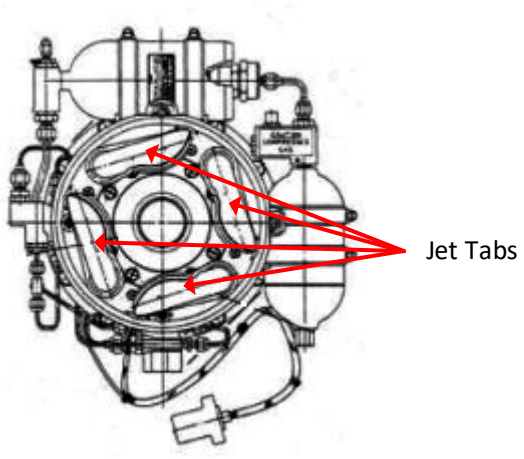

FIGURE 2.4: Jet tab mechanism in Tomahawk cruise missile. (Sutton and Biblarz, 2016)

The final form of mechanical deflector is known as jet deflector. This method in principle uses the same technique as jet tab. The key difference between two methods is that a jet deflector is located around the outer surface of nozzle and manipulates the flow in a parallel manner rather than jet vanes being in the flow at the end of the nozzle. Its component must also be resistant to high temperatures. The main advantage of this method is that the deflection of a jet deflector is linearly related to the deflection of the thrust vector. As the pressure on the deflector increases, it forms shock waves and a resultant side force applies a moment over the vehicle. Conversely, the drawbacks of this method can be listed as existence of high thrust loss, heavy system mechanism and restriction on the exit diameter of nozzle. This method was used in F-16 and the Polaris A-1. Figure 2.5 shows the system in an F-16 aircraft.

FIGURE 2.5: TVC system, F-16. (wikimedia.org, 2021)

2.1.1.2 Secondary Fluid Injection

As an alternative form of mechanical deflectors for fixed nozzle TVC systems, the secondary fluid injection technique changes the flow in the nozzle by injecting secondary fluid from a fluid reservoir into the nozzle. In this method, the secondary fluid can be in the form of liquid or gas. It generates an unsteady flow inside the nozzle and this local high density flow causes a manipulation on the exhaust gas, therefore, it operates the direction of flow as shown in Figure 2.6.

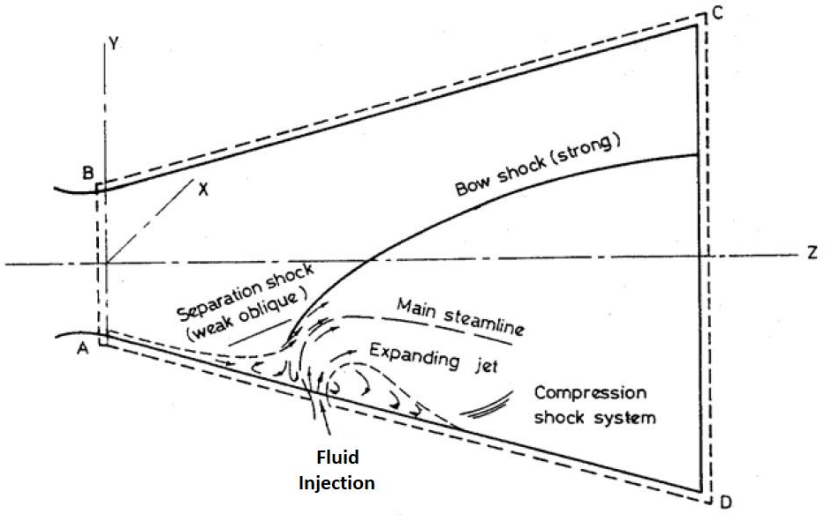

FIGURE 2.6: Secondary injection method (Balu et al., 1991)

There are three primary techniques for the secondary injection method which are known as the shock vector, counter flow and throat shifting, respectively (Schaefermeyer, 2011). These techniques are mostly separated from each other in terms of the vectoring efficiency. It is important to note that the vectoring efficieny is only used for the secondary injection methods. It is defined as the degrees of vectoring achieved per percent of secondary flow required as compared to the primary nozzle flow.

The first approach to secondary fluid injection is shock vector control. Its operating principle is based on generating shock barriers in the supersonic flow. These shock barriers are very effective at manipulating the flow, however they cause a high rate of thrust loss. This method is capable of vectoring efficiencies of up to 3.3°/% injection with thrust ratios ranging from 86% to 94%.

The second technique is the counter-flow method that uses suction between the trailing edge of the nozzle and aft collar. The suction operates reversed flow along the collar. As a result, there is a decrease in pressure and increase in velocity near the reversed flow

area that supplies a thrust differential. The efficiency of this technique is higher with thrust ratios between 92% and 97%.

The final fluidic throat shifting technique uses jets of secondary flow to form a new geometry at the throat. It benefits from minimal thrust loss, but suffers from low performance. The efficiency of this method is up to 2°/% injection while maintaining thrust ratios between 94% and 98%.

To conclude, the methods utilised for secondary fluid injection technique can be compared in terms of the vectoring efficiency and provides a brief summary of its performance. Also, high thrust loss is an inevitable reality of these methods. Lastly, the manipulation of exhaust flow by fluid injection mainly relies on a controlling of shock barriers and chemical reactions which are challenging tasks since it generates an unsteady flow through the nozzle in addition to the supersonic exhaust flow.

For the reasons mentioned above, instead of fixed nozzle, movable nozzle systems are more often used for thrust vectoring which is detailed in the next section.

2.1.2 Movable Nozzle TVC Systems

Movable nozzles are amongst the recently developed and most preferred systems for thrust vectoring. They change the orientation of the nozzle instead of manipulating the flow by mechanical deflectors or generating shock effects by injecting secondary fluid into the nozzle. Movable nozzle systems are very efficient as the thrust loss is much less than the fixed nozzle systems.

Movable nozzle TVC systems are mainly classified into two groups, FJ-TVC and GJ-TVC. Although each system has comparable working principles, there are significant differences in their field of application. This section firstly introduces GJ-TVC with its advantages and disadvantages. Then, FJ-TVC is discussed with its characteristic features such as having a longer lifespan, absence of moving parts, demanding less maintenance and the requirement of less power for low steering angles.

2.1.2.1 Gimbal-Joint TVC

GJ-TVC is used for the systems where the engine and auxiliary components (combustion chamber, nozzle, etc.) are in a small amount of mass and inertia. Liquid propellant engine is the best example of the GJ-TVC system. It is because the fuel and oxidizer tanks are usually of very lightweight construction since they operate at low pressure. Liquid propellant engines mostly include an oxidizer for the combustion of the propellant, however, in some systems such as air breathing engines, outside oxygen from the air is used and therefore, they do not employ an oxidizer in its components. As a disadvantage,

air breathing engines cannot travel in the vacuum of space as they must be able to 'breathe' in order to operate. Alternatively, solid propellant engines provide higher thrust force than liquid propellant engines and are mostly used for long-range travels with small steering angle, e.g. launcher systems. For the solid propellant engines, consequently, the FJ-TVC system is prefered which is detailed in the next section.

A GJ-TVC system consists of two gimbal frames which are termed the inner and outer frames. They are connected to each other at 90° and bearings are used in its rotation axis to manage the vectoring of nozzle on yaw and pitch axes. In gimbal mechanism design, the nozzle is assembled respectively to the inner frame which enables rotation in yaw axis, whereas the outer frame is used to rotate the inner frame and nozzle together in pitch axis. The outer frame is also linked to the vehicle by fixed structures. Figure 2.7 indicates the general design of a GJ-TVC system.

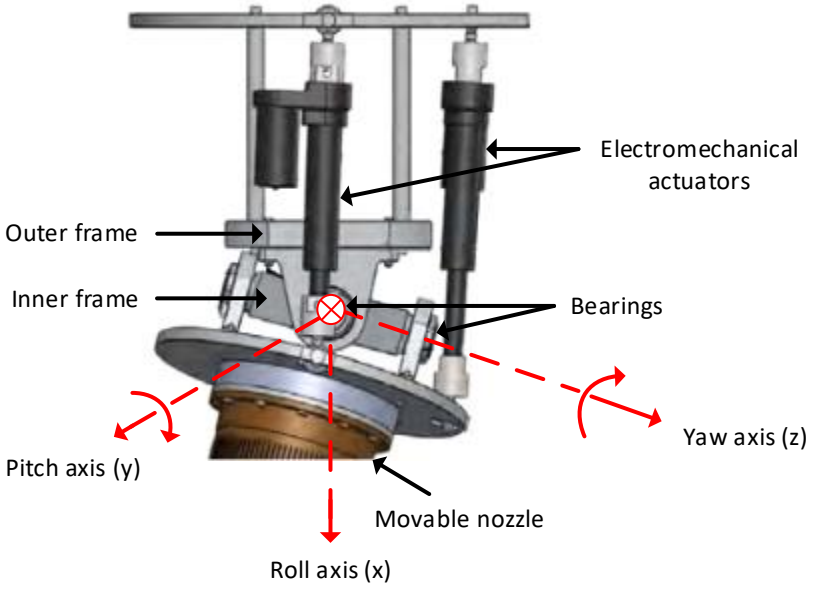

FIGURE 2.7: Gimbal joint thrust vector control (Melo et al., 2013).

As seen from Figure 2.7, there are two actuators that apply a moment about the rotation axes of the nozzle. This moment changes the orientation of nozzle in 2D space and hence allows the vehicles to follow the required trajectory. In GJ-TVC systems, there are some manufacturing errors which cause a thrust off-set and centering issues on the nozzle position. The off-set error becomes more critical when the system has only one engine. However, if the vehicle has more than one gimballed engines, the thrust off-set on one of the nozzle might be compensated by the others.

The GJ-TVC has certain advantages and disadvantages. Its advantages are that it has negligible thrust loss resulting in power efficiency. Secondly, if the trajectory of vehicle specifically requires high steering within the range of $10° - 25°$, then the GJ-TVC technique becomes more feasible as it requires similar torque for higher angles.

Its disadvantages are that since it requires similar level of torque value for lower nozzle angles too, it makes the system inefficient in terms of power consumption. Furthermore, some of the mechanical parts of this system such as the bearings require a maintenance procedure to be undertaken. Hence, if a long-term working schedule is a crucial feature of the system, then the identification and the lubrication of bearings becomes more important. Finally, the assembly of mechanism can be challenging with many precise mechanical parts with tight tolerances.

2.1.2.2 Flexible-Joint TVC

As a second approach to movable nozzle TVC systems, FJ-TVC systems are designed and used within satellite launcher systems and also for tactical systems that require a maximum $\pm 10^{\circ}$ vector angle. It is worth noting that for high steering angles greater than 10°, the spring torque in the flexible joint dramatically increases and requires more powerful actuators which are not feasible in practice. The first usage of this system was reported in the 1970s (Herbert and Reinhardt, 1974; Woodberry, 1975) where the leading concept design of the FJ-TVC system has been developed as seen in Figure 2.8.

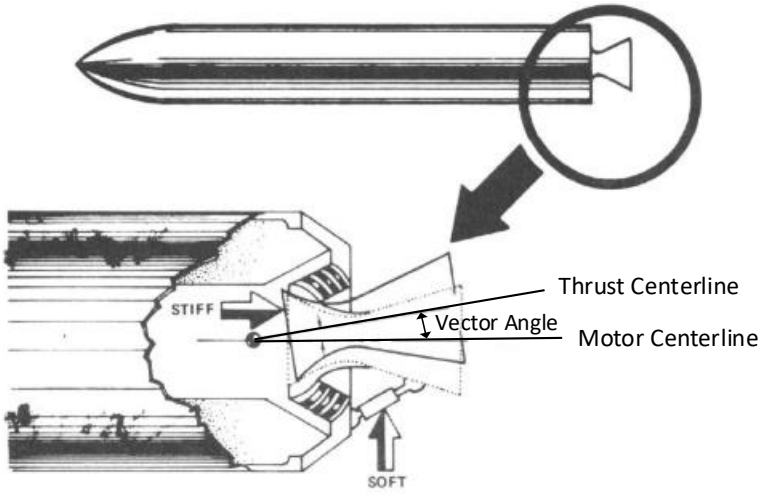

FIGURE 2.8: Consept design of the FJ-TVC system (Herbert and Reinhardt, 1974)

In the mechanism of an FJ-TVC, the structure of the elastomer material is crucial as the counter torque is varied according to its polymeric structure and environmental conditions. The elastomer materials used for the flexible joint are synthetic polymers, natural rubber and silicon depending on the requirements of the system. Curved metal layers are also used to reinforce the elastomer and keep the mechanism at the vehicle centre line. Furthermore, the flexible-joint is isolated from the outer space by sealing material to maintain a suitable temperature range.

An FJ-TVC system is weight-competitive with other types of TVC systems. In addition to its compact design, there are two approaches to using a flexible joint on TVC systems which are designed based on downstream and upstream pivot points. The difference between these two designs are the locations of the pivot point, see Figure 2.9. In this figure, only four elastomeric layers are illustrated, however, many FJ-TVC systems have 10 to 20 layers. In the downstream pivot point design, the axial deformation of the flexible joint in the x-axis is higher than the deformation in the same axis in the upstream pivot point design. However, it should also be noted in the downstream pivot point design that the deformation of flexible joint in y-axis is less than the deformation in the same axis in the upstream pivot point design. It is concluded that if the deformation in the x-axis is more critical, then, the upstream pivot point design is prefered, whereas if the deformation in the y-axis is more critical, the downstream pivot point design is chosen. Consequently, both designs are applicable for the FJ-TVC system, nevertheless, the axial and radial loads, design parameters and system requirements are crucial for high quality control performance (Sutton and Biblarz, 2016).

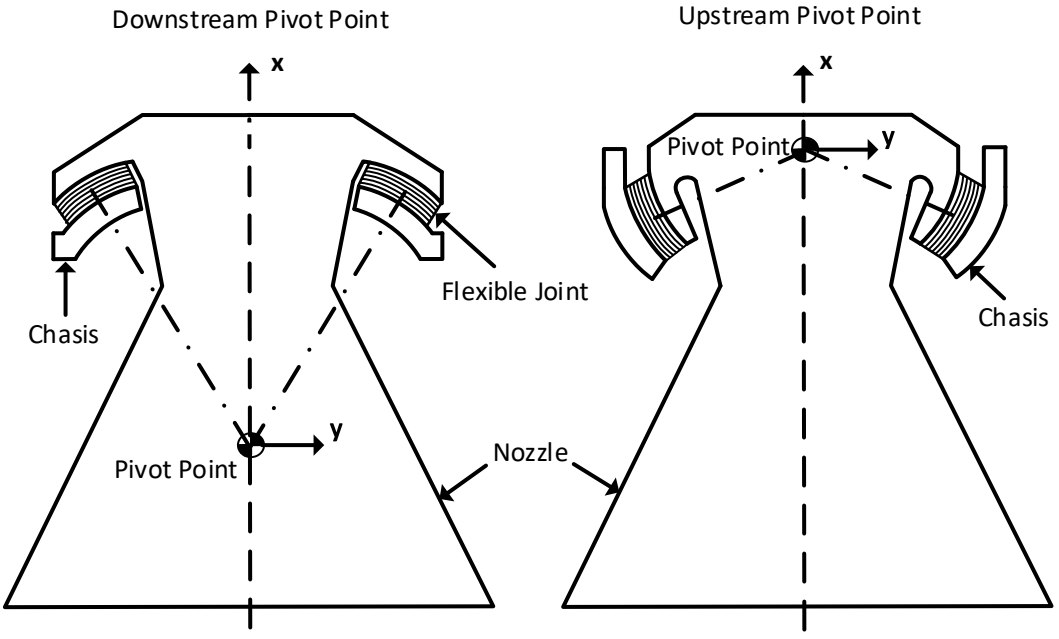

FIGURE 2.9: FJ-TVC with downstream and upstream pivot point.

There are several distinguishing features of FJ-TVC that makes it a unique solution for specific control applications. Initially, it provides a longer lifespan due to the absence of moving mechanical parts within its structure. Also, thrust loss is negligible and it requires less torque at low nozzle angles. This is because, the counter load in the flexible joint is significantly lower at small angles and increases simultaneously with the nozzle angle. However, GJ-TVC demands consistent torque for both high and low level steering as the major parameter in the required torque is the inertia of payload and the misalignment error on the pivot point of the nozzle. In other words, the required torque

is almost the same at low and high rotation angles in the gimbaled mechanism as the payload is exposed to uniform counter-load unlike the variable stiffness torque in the FJ-TVC system. When there is a misalignment error, the required torque increases since the thrust force applies additional counter torque over the nozzle. Therefore, FJ-TVC systems are of great interest due to their longer operational lifespan, negligible thrust loss, minimal maintenance and energy consumption (subject to minimal steering which corresponds to the rotation angle with a maximum $\pm 10^{\circ}$) (Mohan et al., 2011; Sutton and Biblarz, 2016).

Conversely, there are two concerns about the dynamic model and control of FJ-TVC systems (Swain et al., 2019; Chunguang et al., 2020). Firstly, the behaviour of the flexible joint changes significantly under different environmental conditions when in high temperature and low pressure. As a solution to maintain performance, various elastomer and sealing materials are used. However, it is not possible to eliminate misalignments due to the deformation of the flexible joint ompletely because there is a trade-off between power requirement and misalignment error such that if the system requirement desires low power consumption, then the elastomer material for flexible joint should be designed as flexible as possible accordingly to be more sensitive for low counter torques as well as low power consumption, however, it results in misalignment issues. Also, the misalignment issues, due to the deformation of flexible joint or the displacement of pivot point, are not fixed as in GJ-TVC system. Therefore, the dynamic modelling of the FJ-TVC system is a challenging task as it must be in a suitable mathematical form for assessing misalignment errors.

In addition to the above-mentioned concerns, uncertainties need to be defined carefully in the controller design to achieve excellent tracking performance (Yu and Shu, 2017).

The motivation for this research is covered in the next section in detail.

2.2 Motivations for Research in FJ-TVC

This research focuses on the dynamic modelling and robust control of FJ-TVC systems considering the failures in the relevant studies. It is because there are still open fields in the FJ-TVC system to develop for an excellent tracking control. As a motivation of this research, firstly, the working principle of FJ-TVC is introduced and the challenges in the system are defined respectively. Then, the studies in literature review are discussed and where FJ-TVC studies have come to.

In FJ-TVC system, although each component is crucial in terms of functionality, modelling of flexible joint is more critical to achieve high accuracy and reliability (Sutton and Biblarz, 2016). This is because a major part of the flexible joint is made from a rubber material that exhibits different behaviours as the loads and temperatures vary.

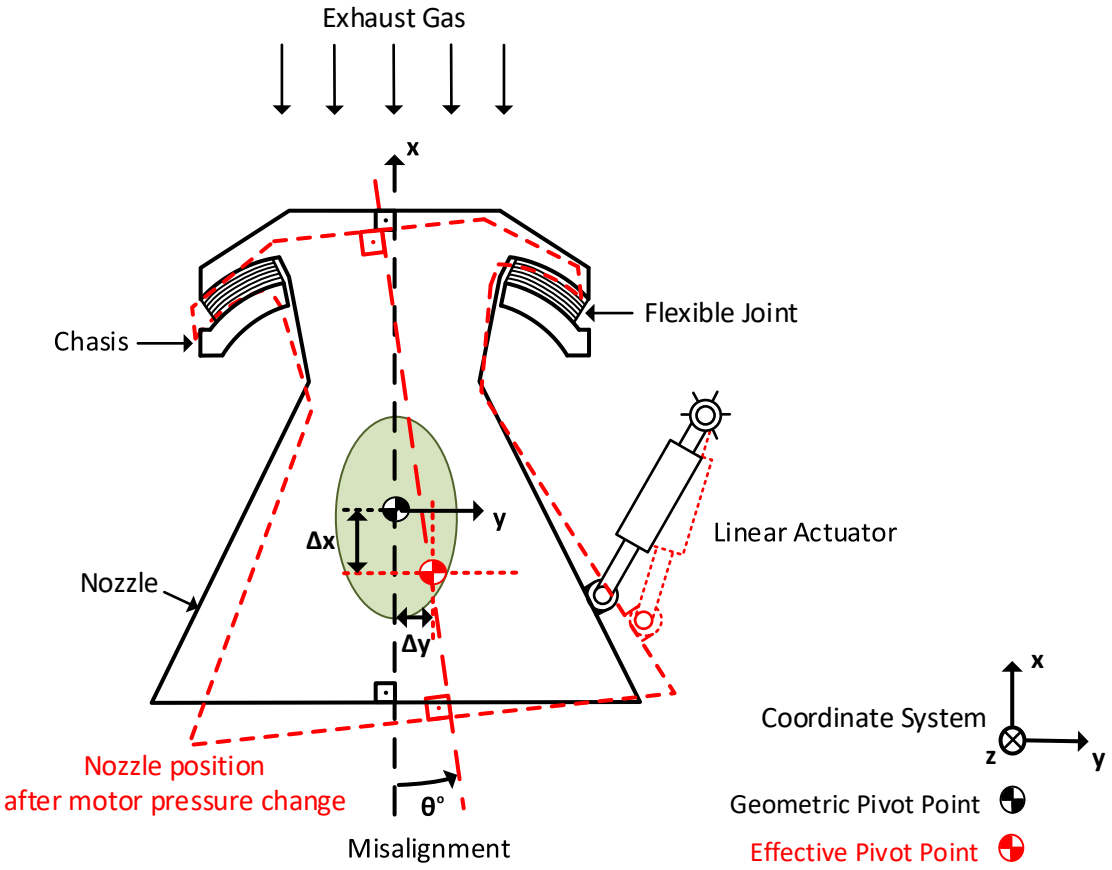

FIGURE 2.10: The position of nozzle after motor pressure is changed.

The pressure change on the nozzle affects the position of pivot point as flexible joint expands to the direction of the thrust. In three-dimensional space, the displacement of the pivot point in FJ-TVC occurs in an elipsoid geometry and in Figure 2.10 its variation in two-dimensional space is given, Δx and Δy, which are exaggerated in the figure to explain the directions more clearly. Additionally, the displacement of the pivot point in the z-axis is defined as Δz which is not shown in the figure. In the thesis, the displacement of pivot point in the x-axis is termed as axial deformation, whereas in y- and z-axes are radial deformation of flexible joint. The misalignment of the nozzle angle is also identified as θ degree in the figure. As a result, modelling of the flexible joint and its uncertainties within different physical and environmental conditions enables it to deliver more reliable, accurate and robust FJ-TVC system.

The uncertainties listed above have been reported in the literature, however, no study has been undertaken where these effects are modelled and experimentally tested to enhance control performance. Most publications on FJ-TVC system assume a universal joint mechanism, which is a simplification that takes no account of the model uncertainties.

This research focuses on the control performance of FJ-TVC system within an estimated range of nozzle misalignment by developing a novel approach to dynamic modelling of

system and implementing different robust controllers.

Next, an overview of the relevant research in this area over the last ten years is given. The notations used in the relevant research are given in accordance with the notations in Figure 2.10.

1. Li et al. (2011) has dealt with the dynamic modelling and control of a GJ-TVC system for aircraft engines. The controller used, known as a hybrid controller, is a combination of a PID controller with lead compensation and bang-bang control. A dynamic model derived for GJ-TVC system has been designed with 2-DoF where the rotational motion of the nozzle about y- and z-axes are evaluated. A real-time experimental study of the hybrid controller has been carried out in the dSPACE HWIL system and claims excellent tracking control performance over the GJ-TVC system.

As a criticism of Li et al. (2011), the misalignment of nozzle angle due to the centering issues in x-, y- and z-axes, corresponds to Δx, Δy and Δz, have not been considered since the design has assumed a fixed pivot point at origin. For this reason, tracking performance of controller is not reliable for in-service TVC systems. Secondly, various experimental test data such as the current data have not been provided even though it plays a vital role on the power requirements. Nevertheless, it is considered that the controller developed in this study is a good alternative to implement in the studies of this thesis after the uncertainties are included in the mathematical model.

2. Lampani et al. (2012) has conducted a finite element analysis of the flexible joint mechanism for a TVC system. The difficulties encountered during the analysis and experiments of the FJ-TVC system due to the strong nonlinear behaviour of rubber under pressure and actuation loads has been discussed. The FJ-TVC system has been designed with 3-DoF where in addition to the rotational motion of the nozzle about the y- and z-axes, the displacement of the pivot point in the x-axis is included. It has been also stated that the flexible joint is subject to two different actions and both are critical on the analysis.

One of the actions is due to the high pressure produced in the combustion chamber. It generates a compression stress on the flexible joint and the off-set on the geometric pivot point is the result of this pressure load. This off-set corresponds to Δx shown in Figure 2.10. The second important action on the FJ-TVC analysis is reported that the flexible joint is exposed to a thermal flux coming through the nozzle. Although there is a thermal protection cover, thermo-mechanical stresses occur and results in deflection on elastomer structure. The analysis performed in the study identifies the temperature distribution along the elastomer and curved metals. It also optimises the thickness and quantity of rubber layers which are reinforced with metal to supply the maximum deflection of flexible joint according to the system requirements. For the finite element analysis of FJ-TVC, several experiments have also been conducted for

the characterisation of the rubber used in the structure. These include simple tension, compression, shear, bulk modulus and equal biaxial extension tests.

The results from the compression stress imposed on the nozzle indicates that the parameter which represents the pivot point displacement over internal diameter of the joint is approximately 6-7 for the FJ-TVC system with 0.25m internal diameter. Therefore, it concludes that the pivot point displacement is 1.7mm in x-axis. This is the main contribution of Lampani et al. (2012) on the modelling of the FJ-TVC system with uncertainties.

Based on Lampani et al. (2012) findings, the pivot point displacement in the x-axis is evaluated, however, the displacement of the pivot point in the y- and z-axes corresponding to the Δy and Δz are neglected. Moreover, this study only focuses on the finite element analysis of FJ-TVC. Therefore, the control design for the FJ-TVC system considering the displacement of pivot point is still an open field to study.

3. Ensworth (2013) has carried out research on the requirements and concepts of TVC systems for representative Nuclear Thermal Rockets (NTR) missions for NASA Glenn Research Centre. Requirements of GJ-TVC systems have been evaluated using three-gimbaled engines, as shown in Figure 2.11, which have 6-DoF in total. Most compatible GJ-TVC systems are listed and its key properties such as mass and power requirements are defined. The main contribution of this study is to define the thrust off-set in the y- and z-axes, corresponds to Δy and Δz, due to manufacturing error in the engine mounting. However, the misalignment on the nozzle angle is handled by the other gimbaled engines.

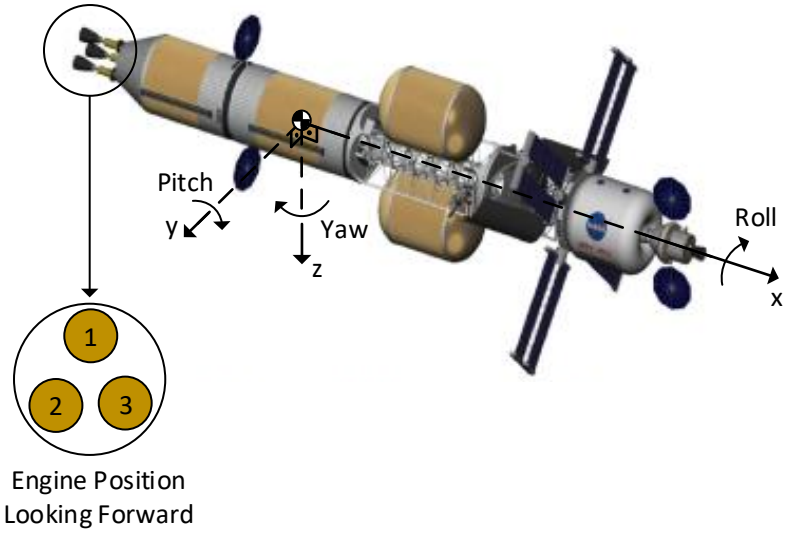

FIGURE 2.11: Crewed vehicle for 600 day Mars orbital mission (Ensworth, 2013).

As a criticism of Ensworth (2013), it is noted that the study only focuses on system requirements of NTR applications. The outputs from this study can be used in sizing of

the systems in accordance with power and mass requirements. Nevertheless, this study only considers some specific uncertainties occurring in GJ-TVC, additional uncertainties in the FJ-TVC system such as the displacement of pivot point in the x-axis are still open to further research.

4. Yu and Shu (2017) has developed a cascaded controller for the GJ-TVC system. This controller is the combination of a Sliding Mode Controller (SMC) with a PID controller. A dynamic model of the GJ-TVC system has been derived which is the same model used in (Li et al., 2011). According to this study, the controller has stronger robustness to parameter uncertainties and therefore achieves a better position tracking performance. The controller has also been compared with a traditional bang-bang controller. Simulation results have been provided to show the outstanding performance of the controller.

The main drawback of the study (Yu and Shu, 2017) is that the misalignment due to the centering issues in the x-, y- and z-axes, Δx, Δy and Δy, have not been considered since the design has assumed a fixed pivot point at the origin. Moreover, experimental verification in addition to simulation studies has not been included and neither has the chattering problem within sliding mode controllers.

5. Swain et al. (2019) has performed experimental tests to characterise the flexible joint of a large solid rocket booster using the 3-D Digital Image Correlation (DIC) method. This study is a novel approach to measure the pivot point displacement as a primary data on FJ-TVC system. The Linear Least Squares (LLS) method has been used for locating the pivot point from the 3-D DIC trajectory. In the experiments, two actuators and a dummy nozzle (referred to as cross beam assembly) were used. During the vectoring tests, this assembly has been exposed to different chamber pressures at 5, 23, 35 and 38,5 bar for the simulation of pivot point displacement. The internal diameter of the nozzle is approximately 1500 mm. Swain et al. (2019) defines the pivot point in two different terms which are geometric and effective as shown in Figure 2.10. This is because the study considers the deformation of the flexible joint under chamber pressure; viscoelastic behaviour of the elastomer; and the asymmetry due to actuator motion. In these circumstances, the effective pivot point is separated from the geometric pivot point.

This study concludes that the displacement of the pivot point is less than 80mm which corresponds to 5% translationin x-axis, Δx, and less than 1% error in the y- and z-axes, Δy and Δz, due to asymmetry in the actuation angle. Also, it is shown that the axial deformation along the flight axis is greater than the asymmetric errors. This is another key contribution to this literature review. However, this study only focuses on the experimental test of an FJ-TVC to determine the pivot point displacement. It has been identified that the dynamic modelling and control of FJ-TVC systems with the behaviours mentioned above are still open to further research.

6. Chunguang et al. (2020) has evaluated the buckling instability of the flexible joint under high pressure in a solid rocket motor. This study points out that FJ-TVC is commonly utilised in solid rocket motors due to its compact structure and mature production technique. It has also been identified that there is between 1-3 degrees of manufacturing deviation at rotation angle of the nozzle. Therefore, when the pressure on combustion chamber increases, the same torque produces greater angular displacement, i.e., requires less torque.

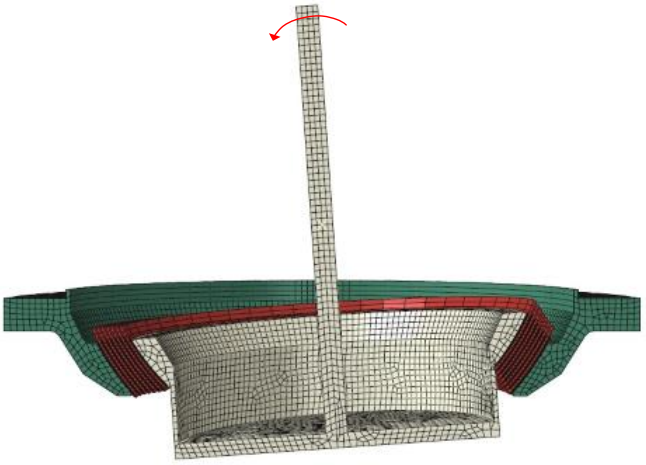

FIGURE 2.12: Finite element model of flexible joint with 1- or 3-degree of manufacturing deviation on rotation angle (Chunguang et al., 2020).

This study validates the variation of spring torque under different pressures obtained through finite element analysis as shown in Figure 2.12. As a contribution of (Chunguang et al., 2020), the deflection on flexible joint model has been formulated in a mathematical equation in terms of change in motor pressure. This was complementary to the simulation and experimental verification process.

The main drawbacks of (Chunguang et al., 2020), are that some parameters in the derived formula and the evaluation of these parameters have not been explained in detail. These parameters include as μ (shape factor), a and n. The estimation of these parameters for different systems are not practicable to make an accurate evaluation.

Secondly, not all flexible-joint behaviours have been covered as previous study (Swain et al., 2019). Moreover, the derived mathematical formula is verified only between 1 - 4 Mpa pressure range in (Chunguang et al., 2020). However, it is known that the pressure on the combustion chamber of solid rocket motor varies between 2-20 MPa, which has not been fully verified within the experimental test.

Lastly, this study just focuses on the mathematical formulation of flexible joint and therefore, the gap on the derivation of dynamic modelling and control of FJ-TVC is still awaiting to be completed.

As a summary, the displacement of pivot point due to the flexible joint behaviour is an important factor for the modelling of the FJ-TVC system. In Table 2.1, previous studies are listed based on DoF, the modelling of the pivot-point off-set whether in axial axis Δx, or radial axis Δy and Δz, the implementing of the controller design and experimental verification.

No	Research	DoF	Δx	Δy, Δz	Controller Design	Experimental Verification
1	Li et al. (2011)	2	x	x	✓	✓
2	Lampani et al. (2012)	3	✓	x	x	x
3	Ensworth (2013)	6	x	✓	✓	x
4	Yu and Shu (2017)	2	x	x	✓	x
5	Swain et al. (2019)	5	✓	✓	x	✓
6	Chunguang et al. (2020)	3	✓	x	x	x

TABLE 2.1: An overview of the previous studies.

Among the previous studies listed in Table 2.1, Lampani et al. (2012); Swain et al. (2019); Chunguang et al. (2020) deal with the FJ-TVC system where none of them includes controller design and its experimental verification. Swain et al. (2019) only evaluates the displacement of pivot point by using 3-D DIC method on an experimental facility and concludes that there occurs 5% translational motion in the x-axis, Δx, and less than 1% radial motion in the y- and z-axes, Δy and Δz, according to the internal diameter of the nozzle. Conversely, Li et al. (2011); Ensworth (2013); Yu and Shu (2017) consider the GJ-TVC system where only the research (Ensworth, 2013) explains the importance of the off-set in the y- and z-axes.

To conclude, after an overview of the previous relevant studies, the research gap is revealed that the dynamic modelling and control design of the FJ-TVC system including the deformation of flexible joint is an open field to research. When axial and radial deformations of flexible joint are analysed, the axial deformation becomes more crucial for the controller design as it is exposed to higher load in axial axis than the radial axis (Swain et al., 2019). Therefore, the dynamic modelling of the FJ-TVC system including the displacement of pivot point in axial axis has been decided to study within this thesis.

2.3 Summary

This chapter has provided a general review of the TVC system, followed by a discussion on common methods based on fixed and movable nozzles. As detailed within the initial section, the movable nozzle method is most recommended due to its negligible thrust

loss. Furthermore, it is not dependent on heat resistance structures nor challenging tasks when controlling the shock barriers and chemical reactions in the supersonic exhaust flow unlike the secondary fluid injection method.

This chapter has also compared the methods for movable nozzle systems which have led to the FJ-TVC system receiving more attention (Lampani et al., 2012; Swain et al., 2019; Chunguang et al., 2020) and making it motivationally appealing for further enhancement.

The key advantages of FJ-TVC are summarised as follows: There is negligible thrust loss; requires less power for low steering; uses a very compact envelope to locate the components; has a longer lifespan because of the absence of moving parts; and demands less maintenance. In the last decade, many results have been obtained while there are still so many of important questions that are awaiting to be answered. These questions can be given as follows: How does the displacement of pivot point in the x-axis affect the control performance of the FJ-TVC system, and can the degradation on trajectory tracking performance be eliminated by using either conventional or model-based controller designs.

One of the main concerns is related with the dynamic modelling of flexible joint used in thrust vectoring. It is known that the behaviour of elastomer material and the position of the pivot point on the nozzle change depending on motor pressure and environmental conditions. These effects have not been considered in the literature (Li et al., 2011; Yu and Shu, 2017) for the controller design. Publications assume that pivot point on the nozzle is fixed by the spherical joint which neglects the displacement of the nozzle in the vertical direction. Moreover, most developed control strategies for FJ-TVC in the literature do not consider parameter uncertainties although it is the essential part of the robust control design (Lampani et al., 2012).

In the next chapter a novel approach to dynamic modelling of a FJ-TVC system including pivot point displacement is developed.

Chapter 3

Dynamic Modelling of the FJ-TVC System

In this chapter, the model for the dynamics of FJ-TVC system considered is developed where each moving component corresponds to a unique link under either rotational or linear motion. In the novel approach to dynamic modelling of an FJ-TVC system, in addition to the rotational motion of nozzle in yaw and pitch axes, the linear displacement of the pivot point is also taken into account. The dynamic model derived in this chapter is for the FJ-TVC test-rig fixed to the ground.

The first section in this chapter introduces the dynamic modelling methods. Following on, the second part gives the formulation of problem. The final part then derives the mathematical model of the FJ-TVC system by using the Lagrange energy equation method.

3.1 A Review of Dynamic Modelling Methods

This section reviews several central concepts used in the derivation of dynamic models. In classical mechanics, there are different approaches to formulate the translational and rotational dynamics of the systems commonly known as, the principle of virtual work, the Newton Euler approach, Hamilton's principle and Langrange's energy equation (Dibenedetto, 2011). There are also some other methods used in the modelling of the dynamic systems such as Boltzmann-Hamel-d'Alembert method which is the extension of the Langrange's energy equation. However, it is suitable for nonholonomic systems. All these methods are briefly introduced in the remaining part of the section.

The principle of virtual work was formulated by Bernoulli in 1700s and this method is efficient for the analysis of multi-link structures that can move relative to each other (Sommerfeld, 1952). In this method, only forces that do work as the system moves

through a virtual displacement are needed to determine the dynamic model of the system. The dynamic version of the principle of virtual work, known as D'Alembert's principle, includes inertial forces in addition to the list of forces that do work (Han and Benaroya, 2002).

The Newton-Euler approach was used in the 18^{th} century to derive the equations of motion for an individual link or body. The motion of a rigid link is decomposed into the translational and rotational motion such that the Newton's dynamic equation describes the translational motion of the Centre of Gravity (CoG) and the Euler's equation evaluates the rotational motion, and the Newton-Euler equation is grouping these motions into a single equation with 6 components, using column vectors and matrices. In the Newton-Euler formulation, as the dynamic equations are written seperately for each link, the derivation of mathematical model for complex systems is more difficult when compared to energy based alternative methods (Canudas-de Wit et al., 1997).

Hamilton's principle is an another way to exhibit the basic laws of mechanics. This approach is also known as Principle of Least Action. The difference in Hamilton's principle and alternatives is that it refers to the entire history of a system's motion between two distinct times. However, there are many mathematical evaluations need to be carried out in this method when compared to the other methods (Cline, 2021).

Lagrange's energy equation method was introduced by the Italian-French mathematician and astronomer Joseph-Louis Lagrange in 1750s. This method offers a systematic approach to formulate the equations of motion of a mechanical system or a flexible structural system with multiple DoF (Morin, 2008). A scalar approach, in this method, is obtained by expressing the scalar quantities of kinetic and potential energy in terms of generalised coordinates.

Lastly, even though it is not a well-know method, Boltzmann-Hamel-d'Alembert approach produces a concise set of dynamic equations which are applied to mechanisms that have nonholonomic constraints. Nonholonomic constraints, nonintegrable motion constraints, typically occur in rolling motions. A charactertistic feature of the system with nonholonomic constraints is that the number of system coordinates required to identify the system's configuration is mostly greater than the number of instantaneous DoF of motion. For such systems, the regular form of Lagrange's equations are not feasible to systems that have nonholonomic constraints (Cameron and Book, 1997).

Overall, the complexity of the system depends entirely on the derivation methods. After the review of the dynamic modelling methods, it was concluded that the most convenient approach for the modelling of the FJ-TVC system in this thesis is Lagrange's energy equation. This is because, the resultant equations are very compact as the multi-body systems are considered as a whole system. It also provides a closed-form expression in terms of joint torques and joint displacements which is directly used in controller design.

Therefore, the next section formulates the problem on the conventional approach to dynamic modelling of FJ-TVC system by using the Lagrange's energy equation method.

3.1.1 Lagrange's Energy Equation

In Lagrange's energy equation potential and kinetic energy are defined in generalised coordinates. It is considered that a system has n DoF and generalised coordinates are denoted by q_i, where $i = 1, 2, ..., n$. Its generalised coordinates are used to specify the potential energy V and kinetic energy T. The potential energy V of a system depends on the position of the system and the kinetic energy T typically depends on velocity, sometimes may be dependent on position. Kinetic energy T and potential energy V can be expressed as functions

$$T = T(q_1, ..., q_n, \dot{q}_1, ..., \dot{q}_n) \tag{3.1}$$

$$V = V(q_1, ..., q_n) \tag{3.2}$$

in terms of generalised coordinates q_i. Then, Lagrange's energy equation is derived by determination of kinetic and potential energy over all generalised coordinates. The dynamic model is formalised as

$$L(q, \dot{q}) = T(q, \dot{q}) - V(q) \tag{3.3}$$

where L represents the Lagrangian function.

The equations of motion for a mechanical system with generalised coordinates are given by

$$\frac{d}{dt}\left(\frac{\partial L}{\partial \dot{q}_i}\right) - \frac{\partial L}{\partial q_i} = \tau_i \tag{3.4}$$

where τ_i is the external force acting on the i_{th} generalised coordinate q_i. As a result, the derivation of (3.4) gives the overall dynamics of a system.

In this method, multi-body systems are considered as a whole system. Therefore, internal reaction forces between the links are automatically eliminated which makes it convenient for multi-body systems. Secondly, the closed-form equations are directly obtained when the differential form of the total energy is solved. Therefore, this method is regarded as the most appropriate technique for the study of dynamic properties and analysis of control schemes.

3.2 Problem Formulation

In FJ-TVC systems, actuators are used to rotate the nozzle in yaw and pitch axes by applying a linear force to overcome the spring torque of the flexible joint. In the literature, the pivot point is assumed as a fixed point at the origin and the nozzle is rotated by using a spherical joint in the TVC system (Li et al., 2011; Yu and Shu, 2017). However, when a fixed point spherical joint is used, it ignores the displacement of pivot point in the x-, y- and z-axes, and therefore neglects misalignments of the nozzle angle. This section examines the consequences of this on the dynamic modelling of the FJ-TVC system.

To derive the conventional dynamic model of the FJ-TVC system, some assumptions have been made which are listed as follows:

- The displacement of the pivot point over the nozzle is neglected and hence, it is assumed that the nozzle only rotates about the y- and z-axes.
- The rotation of the nozzle is limited by ± 5 degrees as the FJ-TVC system is only feasible for small steering angles (Mohan et al., 2011);
- The nozzle is considered as a single body including the auxiliary parts, such as the flexible joint.
- The elastomer material used in the flexible joint is assumed as uniformly distributed, therefore, the counter load in rotation axes, which is modelled as a spring torque with k_1 fixed stiffness contstant in the dynamic model. However, it might have different spring constants at different points and might not exhibit a linear motion.
- The compression length of the spring is determined by using small angle theorem where the displacement of the spring is assumed as $l\theta_1$ which is normally equal to $l \sin \theta_1$.
- The gravity acceleration is taken as a constant in the vertical direction, $g \approx 9.8$ m/s^2.
- The hinge points of the spring and the actuator are designed to be at the same distance from the pivot point, which is decided as a design criteria.
- Friction forces between mechanical parts are neglected.
- Vibrations such as the turbulent eddies generated by the shearing flow are neglected.
- The links are assumed as rigid, however, they have bending modes and behaves as comparatively flexible structures since manufactured by the ABS plastic material.

It might also cause some adverse effects on the controller performance due to the bending forces applied by the actuators.

- The aeroelastic effects, i.e., aerodynamic forces acting on the FJ-TVC system body are neglected.
- Dissipation energy occured between the mechanical parts are ignored.
- When one of the actuators is operating along its longitudinal axis, the other actuator is exposed to rotational motion at radial direction as the actuators are located perpendicular to each other and assembled to the nozzle by a universal joint. For instance, the linear motion of the actuator-1 causes a rotational motion on the actuator-2 about y-axis. However, the total length of the actuator-2 including ballscrew does not vary significantly (measured as 261.94 mm and 262.02 mm at minimum and maximum boundry conditions, which equals to 0.08 mm change) since the nozzle orientation is limited by ± 5 degrees. It is, therefore, the variation on the total length of the actuator due to the rotation of the nozzle around other actuator axis and also the lateral resistance forces at the universal joints are neglected in the dynamic analysis.

3.3 Conventional Dynamic Model of the FJ-TVC System

This section derives the conventional dynamic model of the FJ-TVC system. In the conventional approach, the system is considered as a prototype implemented on the ground.

In Figure 3.1, the dynamic modelling of a TVC system is shown, where the nozzle rotates about y- and z-axes in θ_y and θ_z degrees, where O is the pivot point which is fixed to the ground by spherical joint. The total mass of the nozzle and the flexible joint is m, and the corresponding moment of inertia with respect to y- and z-axes are given by J_{yy} and J_{zz}. Additionally, the CoG of the nozzle is defined by point a and the length between the pivot point O and the CoG is given by l.

Once the nozzle is rotated θ_y degrees in y-axis and θ_z degrees in z-axis, the CoG of the nozzle arrives point a'. To evaluate the exact position of point a' in the reference cartesian coordinate system, the following position vector of the nozzle is used:

$$Oa' = \overrightarrow{r} = \begin{pmatrix} l\cos\theta_z\cos\theta_y \\ l\sin\theta_z \\ -l\cos\theta_z\sin\theta_y \end{pmatrix} \tag{3.5}$$

which can also be represented by

$$\overrightarrow{r} = (l\cos\theta_z\cos\theta_y)e_x + (l\sin\theta_z)e_y + (-l\cos\theta_z\sin\theta_y)e_z \tag{3.6}$$

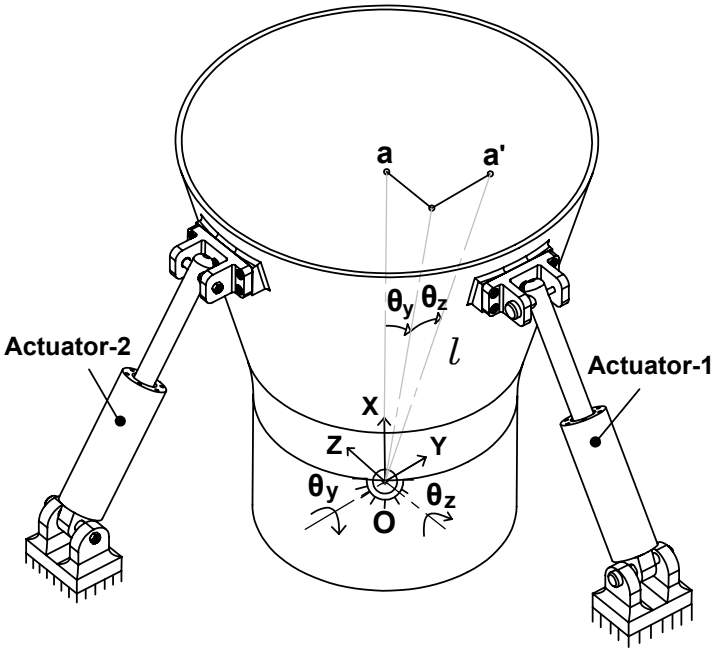

FIGURE 3.1: Conventional approach to dynamic modelling of a TVC system (springs not shown).

where e_x, e_y and e_z correspond to the components of cartesian coordinate system in x-, y- and z-axis, respectively. Given $\overrightarrow{r}$, the corresponding velocity vector is

$$\begin{aligned}\overrightarrow{\dot{r}} =& -(l\dot{\theta}_z \sin\theta_z \cos\theta_y + l\dot{\theta}_y \cos\theta_z \sin\theta_y)e_x + (l\dot{\theta}_z \cos\theta_z)e_y \\ &+ (l\dot{\theta}_z \sin\theta_z \sin\theta_y - l\dot{\theta}_y \cos\theta_z \cos\theta_y)e_z \end{aligned} \tag{3.7}$$

The total kinetic energy of the system is

$$T = \frac{1}{2}m\|\dot{r}\|^2 + \frac{1}{2}J_{yy}\dot{\theta}_y^2 + \frac{1}{2}J_{zz}\dot{\theta}_z^2 \tag{3.8}$$

and the potential energy is

$$V = mg(l\cos\theta_y \cos\theta_z) + \frac{1}{2}k_1(l\theta_y)^2 + \frac{1}{2}k_1(l\theta_z)^2 \tag{3.9}$$

where g is the gravitational constant (upright). The gravitational force is not shown in Figure 3.1, however, it is applied vertically at the CoG of the nozzle as the system considered in the thesis is a test-rig implemented on the ground. Additionally, k_1 is the spring constant of the compression spring which is modelled as a radial counter-load. Therefore, the Lagrangian is

$$\begin{aligned}L =& \frac{1}{2}ml^2(\dot{\theta}_z^2 + \dot{\theta}_y^2\cos^2\theta_z) + \frac{1}{2}J_{yy}\dot{\theta}_y^2 + \frac{1}{2}J_{zz}\dot{\theta}_z^2 - mg(l\cos\theta_y\cos\theta_z) \\ &- \frac{1}{2}k_1 l^2(\theta_y^2 + \theta_z^2) \end{aligned} \tag{3.10}$$

Then, the equations of motion in (3.4) are rewritten in terms of generalised coordinates θ_y and θ_z as follows:

$$\frac{d}{dt}\left(\frac{\partial L}{\partial \dot{\theta}_y}\right) - \frac{\partial L}{\partial \theta_y} = M_{\theta_y} \tag{3.11}$$

$$\frac{d}{dt}\left(\frac{\partial L}{\partial \dot{\theta}_z}\right) - \frac{\partial L}{\partial \theta_z} = M_{\theta_z} \tag{3.12}$$

where

$$\frac{\partial L}{\partial \dot{\theta}_y} = ml^2\dot{\theta}_y \cos^2\theta_z + J_{yy}\dot{\theta}_y \tag{3.13}$$

$$\frac{d}{dt}\left(\frac{\partial L}{\partial \dot{\theta}_y}\right) = ml^2\ddot{\theta}_y \cos^2\theta_z + J_{yy}\ddot{\theta}_y - ml^2\dot{\theta}_y\dot{\theta}_z \sin(2\theta_z) \tag{3.14}$$

$$\frac{\partial L}{\partial \theta_y} = mgl \sin\theta_y \cos\theta_z - k_1 l^2\theta_y \tag{3.15}$$

and

$$\frac{\partial L}{\partial \dot{\theta}_z} = ml^2\dot{\theta}_z + J_{zz}\dot{\theta}_z \tag{3.16}$$

$$\frac{d}{dt}\left(\frac{\partial L}{\partial \dot{\theta}_z}\right) = ml^2\ddot{\theta}_z + J_{zz}\ddot{\theta}_z \tag{3.17}$$

$$\frac{\partial L}{\partial \theta_z} = -\frac{1}{2}ml^2\dot{\theta}_y^2 \sin(2\theta_z) + mgl \cos\theta_y \sin\theta_z - k_1 l^2\theta_z \tag{3.18}$$

and hence, the overall dynamics are described by

$$\begin{bmatrix} M_{\theta_y} \\ M_{\theta_z} \end{bmatrix} = \begin{bmatrix} ml^2\cos^2\theta_z + J_{yy} & 0 \\ 0 & ml^2 + J_{zz} \end{bmatrix} \begin{bmatrix} \ddot{\theta}_y \\ \ddot{\theta}_z \end{bmatrix} + \begin{bmatrix} -ml^2\dot{\theta}_y\dot{\theta}_z \sin(2\theta_z) \\ \frac{1}{2}ml^2\dot{\theta}_y^2 \sin(2\theta_z) \end{bmatrix} + \begin{bmatrix} -mgl \sin\theta_y \cos\theta_z \\ -mgl \cos\theta_y \sin\theta_z \end{bmatrix} + \begin{bmatrix} k_1 l^2\theta_y \\ k_1 l^2\theta_z \end{bmatrix} \tag{3.19}$$

In this conventional approach to modelling a FJ-TVC system, with respect to a given initial position and velocity of the link, (3.19) determines the subsequent motion of the system. It is obvious in this mathematical model that the displacement of the pivot point in the x-axis is not taken into account, where only the rotational motion of the nozzle, θ_y and θ_z are determined. The same situation arises in the studies in the literature (Yu and Shu, 2017; Li et al., 2011). However, neglecting structurally important terms in the mathematical model of FJ-TVC system prevents high quality tracking control performance. For this reason, a novel approach to dynamic modelling of the FJ-TVC system is derived in the next section.

3.4 Derivation of the FJ-TVC Dynamic Model

This section derives the mathematical model of the FJ-TVC test-rig. When deriving the dynamic model of the system, some assumptions defined in Section 3.1 have been improved. These assumptions are listed as follows:

- The displacement of the pivot point in the x-axis is included, which is defined as d, whereas the y- and z-axes are neglected. It is because the studies about the FJ-TVC system in the literature have been concluded that translational motion of the pivot point is around 5% in x-axis and 1% in y- and z-axes with respect to the internal diameter of the nozzle (Swain et al., 2019; Lampani et al., 2012). In the conventional dynamic model, conversely, the displacement of pivot point is ignored at all as discussed in the previous section.
- The dynamic model in this section includes an extra link (link-1) for the translational motion of the nozzle, which is necessary for the FJ-TVC system test-rig to benchmark the controller performance over the pivot point displacement in the x-axis. In the dynamic model of the original system, instead of including *Link-1*, the total energy arising from the translational and rotational motion of the nozzle as a single body is sufficient to evaluate. However, for both cases, the rest of the steps followed in the derivation of the Lagrange's equation are the same.
- In the real FJ-TVC system, the flexible joint elongates in the flight axis as the engine pressure increases and applies more pressure over the nozzle. The elongation of the flexible joint in the x-axis is, therefore, represented by tension springs in the mathematical modelling. It is also assumed that there is a linear relationship between the engine pressure and the pivot point displacement in vertical direction, however, the relationship might be nonlinear. It can be verified by performing adequate tests within a genuine FJ-TVC system including a pressure sensor.

Based on the assumptions listed above, Lagrange's energy equation method is used to formalise the dynamics of the FJ-TVC, where Figure 3.2 specifies all links in the system and their joint types as prismatic or revolute. It can be concluded from Figure 3.2 that *Link-1* is formed by prismatic joint and moves in the x-axis with magnitude d, *Link-2* is formed by a revolute joint and rotates in the y-axis with magnitude of θ_y, lastly, *Link-3* is also formed as a revolute joint and rotates in the z-axis with magnitude θ_z.

To model the counter loads on the FJ-TVC, springs are used. One of the spring is placed through the prismatic joint which is exposed to the tension force in the x-axis. The other four springs are assembled symmetrically to the linear actuators. These springs have not shown in Figure 3.2 to avoid complexity. However, it is worth noting that the four compression springs are assembled to the ground and nozzle at the same heights of the

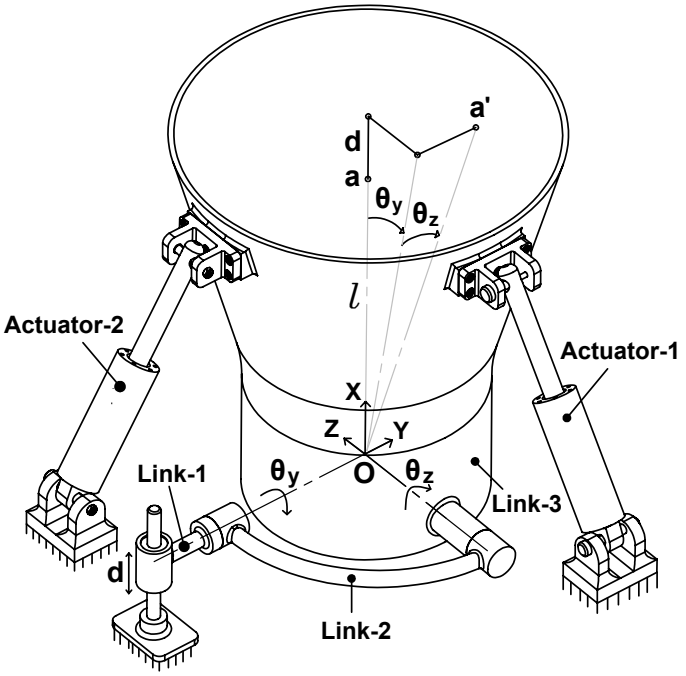

FIGURE 3.2: Representation of the FJ-TVC model (springs not shown and only one quadrant of Link-2 is shown even though it is a circular symmetric link about x-axis.)

actuators in terms of connection points. Additionally, one of the compression spring is assembled symmetrically to the middle of the actuators about the x-axis, where the rest of the compression springs are assembled with 90 degrees of radial clearances between each other about the same axis.

The position vector of the system when it moves in the x-axis with the distance of d is defined as $\overrightarrow{r_x} = de_x$. Therefore, the velocity vector of the system for the corresponding displacement is equal to derivative of $\overrightarrow{r_x}$, i.e., $\dot{\overrightarrow{r_x}} = \dot{d}e_x$. Also, there is a tension spring with a spring constant k_2. Hence the potential energy for the vertical displacement is

$$V_1 = -m_x g d + \frac{1}{2} k_2 (d)^2 \tag{3.20}$$

and the kinetic energy is

$$T_1 = \frac{1}{2} m_x \dot{d}^2 \tag{3.21}$$

where m_x is the total mass of *Link-1*, *Link-2* and *Link-3*, i.e., $m_x = m_1 + m_2 + m_3$, as all the links are moving in the x-axis together. Even though the links are specified in Figure 3.2, it is crucial to clarify that m_1 is the mass of *Link-1*, which is a component that slides up and down in the x-axis, m_2 is the mass of *Link-2*, which is a circular frame that rotates together with the nozzle about the y-axis, and lastly, m_3 is the mass of *Link-3* which corresponds to the nozzle and rotates about the z-axis.

The position vector of the system when it rotates about the y-axis in θ_y is $\overrightarrow{r_y} =$

$(l_y \cos(\theta_y))e_x - (l_y \sin(\theta_y))e_z$ where l_y is the length between the pivot point O and the CoG of the components rotating about the y-axis, which corresponds to the total CoG of the *Link-2* and *Link-3* as they are rotating together about the yaw axis. Also, there is a compression spring with associated constant k_1. The displacement of the spring is given by $l_y\theta_y$. Hence the potential energy of the system when rotating about the yaw axis is

$$V_2 = -m_y g(l_y \cos(\theta_y)) + \frac{1}{2}k_1(l_y\theta_y)^2 \tag{3.22}$$

and the kinetic energy is

$$T_2 = \frac{1}{2}m_y(l_y^2\dot{\theta}_y^2 + l_y^2\dot{\theta}_y^2 \sin(2\theta_y)) + \frac{1}{2}J_{yy}\dot{\theta}_y^2 \tag{3.23}$$

where m_y is the total mass of *Link-2* and *Link-3*. Also, J_{yy} is the total moment of inertia of *Link-2* and *Link-3* with respect to the pivot point O.

The position vector of the system when it rotates about the z-axis is formalised by the similar approach as about the yax axis, i.e., $\overrightarrow{r_z}= (l_z \cos\theta_z \cos\theta_y)e_x + (l_z \sin\theta_z)e_y - (l_z \cos\theta_z \sin\theta_y)e_z$ where l_z corresponds to the length between the pivot point O and the CoG of the nozzle, which is not shown in Figure 3.2 to avoid complexity. Also, there is a compression spring with an associated constant k_1. Hence the potential energy of the system is

$$V_3 = -m_z g(l_z \cos\theta_z \cos\theta_y) + \frac{1}{2}k_1(l_z\theta_z)^2 \tag{3.24}$$

and the kinetic energy is

$$\begin{aligned} T_3 = \frac{1}{2}m_z(l_z^2\dot{\theta}_z^2 + l_z^2\dot{\theta}_y^2 \cos^2\theta_z - 2l_z\dot{\theta}_z \sin\theta_z \cos\theta_y \\ - 2l_z\dot{\theta}_y \cos\theta_z \sin\theta_y) + \frac{1}{2}J_{zz}\dot{\theta}_z^2 \end{aligned} \tag{3.25}$$

where $m_z = m_3$ is the mass of the *Link-3*, i.e., the nozzle, and J_{zz} is the moment of inertia of *Link-3* with respect to the pivot point O.

The *Lagrangian* L for all links is

$$L(q, \dot{q}) = \sum_{i=1}^{i=3} T_i(q_i, \dot{q}_i) - V_i(q_i) \tag{3.26}$$

and hence

$$\begin{aligned} L = &\frac{1}{2}m_x\dot{d}^2 + \frac{1}{2}m_y(l_y^2\dot{\theta}_y^2 + l_y^2\dot{\theta}_y^2\sin(2\theta_y)) + \frac{1}{2}J_{yy}\dot{\theta}_y^2 \\ &+ \frac{1}{2}m_z(l_z^2\dot{\theta}_z^2 + l_z^2\dot{\theta}_y^2\cos^2\theta_z - 2l_z\dot{\theta}_z\sin\theta_z\cos\theta_y \\ &- 2l_z\dot{\theta}_y\cos\theta_z\sin\theta_y) + \frac{1}{2}J_{zz}\dot{\theta}_z^2 + m_xgd \\ &+ m_yg(l_y\cos\theta_y) + m_zg(l_z\cos\theta_z\cos\theta_y) - \frac{1}{2}k_2d^2 \\ &- \frac{1}{2}k_1(l_y\theta_y)^2 - \frac{1}{2}k_1(l_z\theta_z)^2 \end{aligned} \tag{3.27}$$

Next, the equation of motions are derived using each of the generalised coordinates (d, θ_y, θ_z) as given in (3.26). As one case, the equation of motion for *Link-1* is given by

$$\frac{d}{dt}\left(\frac{\partial L}{\partial \dot{d}}\right) - \frac{\partial L}{\partial d} = F_d \tag{3.28}$$

where F_d, given next, governs the required force to obtain a desired position of the system

$$\begin{aligned} F_d = &m_x\ddot{d} + \ddot{\theta}_y(m_yl_y\cos\theta_y \\ &- m_zl_z\cos\theta_z\sin\theta_y) + \ddot{\theta}_z(-m_zl_z\sin\theta_z\cos\theta_y) \\ &- m_yl_y\dot{\theta}_y^2\sin\theta_y - m_zl_z\cos\theta_z\cos\theta_y(\dot{\theta}_y^2 + \dot{\theta}_z^2) \\ &+ 2m_zl_z\dot{\theta}_y\dot{\theta}_z\sin\theta_z\sin\theta_y + m_xg \\ &+ k_2d \end{aligned} \tag{3.29}$$

Repeating this analysis for the remaining generalised coordinates as in (3.12) gives the following model for the complete system

$$\begin{bmatrix} F_d \\ M_{\theta_y} \\ M_{\theta_z} \end{bmatrix} = \begin{bmatrix} M_{11} & M_{12} & M_{13} \\ M_{21} & M_{22} & M_{23} \\ M_{31} & M_{32} & M_{33} \end{bmatrix} \begin{bmatrix} \ddot{d} \\ \ddot{\theta}_y \\ \ddot{\theta}_z \end{bmatrix} + \begin{bmatrix} N_1 \\ N_2 \\ N_3 \end{bmatrix} \tag{3.30}$$

where

$$
\begin{aligned}
M_{11} &= m_x \\
M_{12} &= m_y l_y \sin\theta_y - m_z l_z \cos\theta_z \sin\theta_y \\
M_{13} &= -m_z l_z \sin\theta_z \cos\theta_y \\
M_{21} &= m_y l_y \cos\theta_y - m_z l_z \cos\theta_z \sin\theta_y \\
M_{22} &= m_y l_y^2 + J_{yy} + m_z l_z^2 \cos^2\theta_z \\
M_{23} &= 0 \\
M_{31} &= -m_z l_z \sin\theta_z \cos\theta_y \\
M_{32} &= 0 \\
M_{33} &= m_z l_z^2 + J_{zz}
\end{aligned}
$$

and

$$
\begin{aligned}
N_1 &= -m_y l_y \dot{\theta}_y^2 \cos\theta_y - m_z l_z \cos\theta_z \cos\theta_y (\dot{\theta}_y^2 + \dot{\theta}_z^2) \\
&\quad + 2 m_z l_z \dot{\theta}_y \dot{\theta}_z \sin\theta_z \sin\theta_y + m_x g \\
&\quad + k_2 d \\
N_2 &= -m_z l_z^2 \dot{\theta}_y \dot{\theta}_z \sin(2\theta_z)(1/2) + m_y g l_y \cos\theta_y \\
&\quad + m_z g l_z \cos\theta_z \sin\theta_y + k_1 l_y^2 \theta_y \\
N_3 &= \frac{1}{2} m_z l_z^2 \dot{\theta}_y^2 \sin(2\theta_z) + m_z g l_z \sin\theta_z \cos\theta_y + k_1 l_z^2 \theta_z
\end{aligned}
$$

From (3.30), this dynamic model takes into account the displacement of the pivot point in addition to the rotational motion of the nozzle in the yaw and pitch axes, which is the significant improvement when compared to the conventional model in (3.19).

After evaluating the required force and torques in (3.30), the next step is to converting these variables into the actuator forces. The forces applied by the actuator-1 and -2 at hinge points B and C are defined as F_y and F_z, respectively, as shown in Figure 3.3.

According to the moment of force rule, see Hibbeler (2004), the applied force is multiplied by the perpendicular distance from the pivot point O. Therefore, the required force and torques in (3.30) can be substituted by the following equations:

$$F_d = F_z \sin(\phi_2) - F_y \sin(\phi_1) \tag{3.31}$$

$$M_{\theta_y} = F_y \cos(\phi_1) C_x + F_y \sin(\phi_1) C_z \tag{3.32}$$

$$M_{\theta_z} = F_z \cos(\phi_2) B_x + F_z \sin(\phi_2) B_y \tag{3.33}$$

where ϕ_1 and ϕ_2 are the angles of the actuators with respect to the z- and y-axes, respectively. These angles are dependent on the vertical displacement of the nozzle d and the corresponding nozzle angle θ_y or θ_z. At zero-angle position of the nozzle, ϕ_1 is designed to be equal to ϕ_2 as a design criteria. It should also be noted that B_x, B_y,

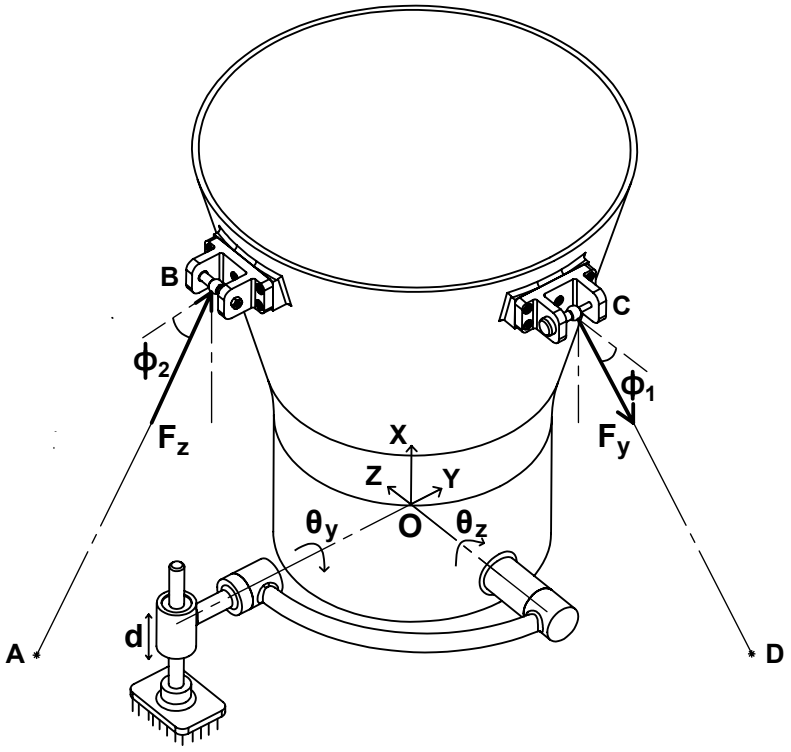

FIGURE 3.3: The forces F_y and F_z applied by the Actuator-1 and -2, respectively.

C_x and C_z are the isometric lengths of the points B and C over the x-, y- and z-axes. For the sake of clarity, a 2-D representation of the system on the xy-plane is shown in Figure 3.4, where at the initial position, see Figure (a), the reference point representing the reference coordinate system is coincident with the origin point O. After the vertical motion of the nozzle along the x-axis in d milimeters and the rotation of the nozzle around z-axis in θ_z degrees, the orientation of the nozzle becomes as in Figure 3.4.

The closed kinematics of the system, i.e., the position equations of the nozzle about yaw and pitch axis can be derived by using Figure 3.3 where the points A and D correspond to the end pivot points of the actuator-2 and -1, respectively. More specifically, the position equation of the nozzle when it is rotated about the yaw axis can be derived more clearly by using the 2-D representation of the nozzle on xy-plane, see Figure 3.4. Therefore, the position equation can be written as

$$\overrightarrow{AB} = \overrightarrow{AR} + \overrightarrow{RO} + \overrightarrow{OB} \tag{3.34}$$

where $\overrightarrow{AB}$ is the vector from the point A to B which corresponds to the linear actuator-2 orientation, $\overrightarrow{AR}$ is the constant vector between the point A and the reference point R at y-axis, $\overrightarrow{RO}$ is the vector representing the vertical displacement of the nozzle d in x-axis and $\overrightarrow{OB}$ is the vector expressing the constant distance between the pivot point O and the hinge point B where α_2 is the angle of the $\overrightarrow{OB}$ with respect to the x-axis. Within the same approach, the position equation of the nozzle in the xz plane (including the

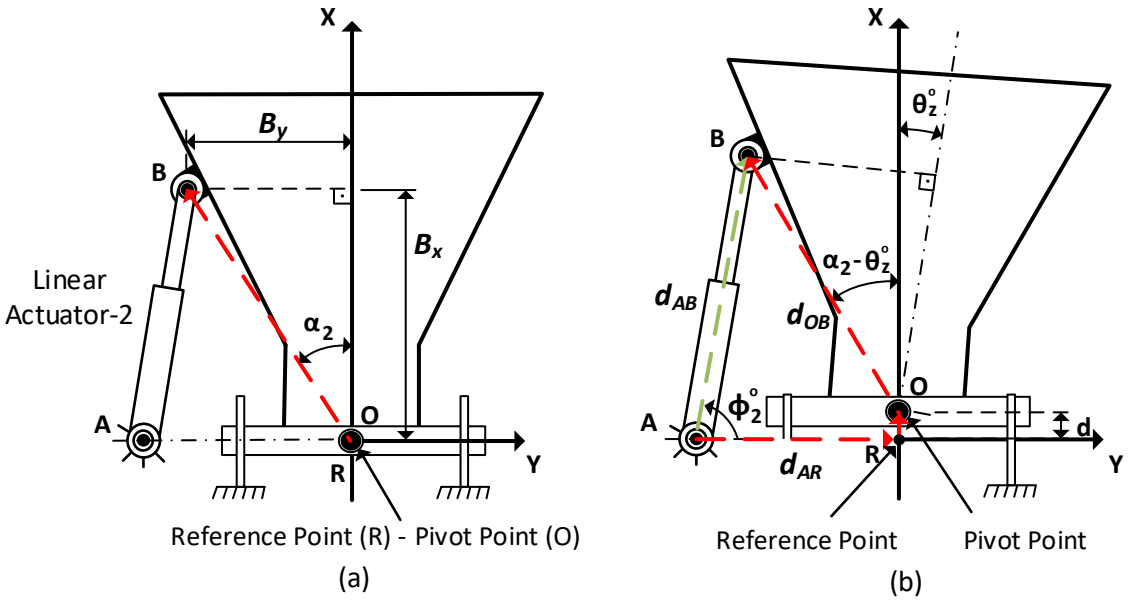

FIGURE 3.4: 2-D representation of the nozzle on xy-plane

linear actuator-1 movement) can be written as well, where the linear actuator-1 position is given between the point C and D. To find out the relationship of the $\sin(\phi_1)$, $\cos(\phi_1)$, $\sin(\phi_2)$ and $\cos(\phi_2)$ in (3.31), (3.32) and (3.33) with respect to d, θ_y and θ_z, the closed kinematics of the system in (3.34) is used, and hence

$$\begin{aligned}
\sin(\phi_1) &= \frac{d + d_{OC}\cos(\alpha_1 - \theta_y)}{d_{CD}} \\
\cos(\phi_1) &= \frac{d_{AR} - d_{OC}\sin(\alpha_1 - \theta_y)}{d_{CD}} \\
\sin(\phi_2) &= \frac{d + d_{OB}\cos(\alpha_2 - \theta_z)}{d_{AB}} \\
\cos(\phi_2) &= \frac{d_{AR} - d_{OB}\sin(\alpha_2 - \theta_z)}{d_{AB}}
\end{aligned} \tag{3.35}$$

are obtained where $\alpha_1 = \alpha_2 = \arctan(B_y/B_x)$ and $d_{OB} = d_{OC}$ due to the rotational symmetry of the nozzle about x-axis. These equations are utilised in the transformation matrix of the system to convert the required force and torques to the actuator forces as shown below:

$$\begin{bmatrix} F_d \\ M_{\theta_y} \\ M_{\theta_z} \end{bmatrix} = \begin{bmatrix} -\sin(\phi_1) & \sin(\phi_2) \\ C_x\cos(\phi_1) + C_z\sin(\phi_1) & 0 \\ 0 & B_x\cos(\phi_2) + B_z\sin(\phi_1) \end{bmatrix} \begin{bmatrix} F_y \\ F_z \end{bmatrix} \tag{3.36}$$

To evaluate the position kinematics of the nozzle, the data obtained from the conceptual design of the FJ-TVC test-rig in 3D-modelling software is used, which are given in Table 3.1. It is concluded from the table that the total length of the actuator is 262.02 mm at zero initial position and it extends to 265.98 mm when the nozzle moves 4 mm at

θ_z (deg)	d (mm)	$\lvert\overrightarrow{AB}\rvert$ (mm)	ϕ_2 (deg)
0	0	262.02	82.87
0	4	265.98	82.98
5	0	275.87	79.10
5	4	279.79	79.25

TABLE 3.1: The total length of the actuator-2 at different nozzle orientations.

x-axis, where the elongation of the actuator is almost equal to the vertical displacement of the nozzle as the actuator is assembled to the nozzle almost vertically. Based on the kinematic analysis, it can also be confirmed that the vertical displacement of pivot point has a crucial effect over the nozzle orientation, where if it is not included in the dynamic analysis, a misalignment occurs on the nozzle angle. To be more precise, when the pivot point translated 4 mm at x-axis, the total length of the actuator has to be 265.98 mm to keep the nozzle at 0° position, where if the actuator hold fixed, i.e., for the 262.02 mm actuator length, the nozzle has 1.4° misalignment according to the zero-angle position, which is a remarkable error when compared to ±5 degrees rotation limit of the FJ-TVC system.

As a next step, the derived mathematical model in (3.30) is rewritten in the general dynamic equation form of a system with rigid links, see (Spong and Vidyasagar, 2008), where the required force and torque is determined by

$$\tau = M(q)\ddot{q} + C(q,\dot{q}) + G(q) + \tau_d \tag{3.37}$$

where $q(t) \in \mathbb{R}^{3x1}$ is the vector of generalised coordinates, $M(q) \in \mathbb{R}^{3x3}$ is the the inertia matrix, $C(q,\dot{q}) \in \mathbb{R}^{3x3}$ is the Coriolis/centripetal matrix, $G(q) \in \mathbb{R}^{3x3}$ is the summation of gravity and spring force vector, $\tau \in \mathbb{R}^{3x1}$ is the vector of required force/torque and $\tau_d \in \mathbb{R}^{3x1}$ is the vector of disturbance. It is concluded that $N(q,\dot{q})$ in (3.30) corresponds to $C(q,\dot{q})+G(q)$ and the disturbance τ_d is zero. The control input vector τ has components of torque for the revolute joints and force for the prismatic joints, which is given by the multiplication of transformation matrix $T \in \mathbb{R}^{3x2}$ and the applied force vector $F \in \mathbb{R}^{2x1}$.

Therefore, when the generalised coordinates of the system are defined as $q = [d, \theta_y, \theta_z]^T$, the overall dynamic model can be written as follows:

$$\underbrace{\begin{bmatrix} T_{11} & T_{12} \\ T_{21} & 0 \\ 0 & T_{32} \end{bmatrix}}_{\boldsymbol{T}} \begin{bmatrix} F_y \\ F_z \end{bmatrix} = \underbrace{\begin{bmatrix} M_{11} & M_{12} & M_{13} \\ M_{21} & M_{22} & 0 \\ M_{31} & 0 & M_{33} \end{bmatrix}}_{\boldsymbol{M}} \begin{bmatrix} \ddot{d} \\ \ddot{\theta}_y \\ \ddot{\theta}_z \end{bmatrix} + \underbrace{\begin{bmatrix} 0 & C_{12} & C_{13} \\ 0 & C_{22} & 0 \\ 0 & C_{32} & 0 \end{bmatrix}}_{\boldsymbol{C}} \begin{bmatrix} \dot{d} \\ \dot{\theta}_y \\ \dot{\theta}_z \end{bmatrix} \tag{3.38}$$

$$+ \underbrace{\begin{bmatrix} G_{11} & 0 & 0 \\ 0 & G_{22} & 0 \\ 0 & 0 & G_{33} \end{bmatrix}}_{\boldsymbol{G}} \begin{bmatrix} d \\ \theta_y \\ \theta_z \end{bmatrix}$$

where

$$\begin{aligned}
T_{11} &= -\frac{d + d_{OC}\cos(\alpha_1 - \theta_y)}{d_{CD}} \\
T_{12} &= \frac{d + d_{OB}\cos(\alpha_2 - \theta_z)}{d_{AB}} \\
T_{21} &= C_x \frac{d_{AR} - d_{OC}\sin(\alpha_1 - \theta_y)}{d_{CD}} + C_z \frac{d + d_{OC}\cos(\alpha_1 - \theta_y)}{d_{CD}} \\
T_{32} &= B_x \frac{d_{AR} - d_{OB}\sin(\alpha_2 - \theta_z)}{d_{AB}} + B_y \frac{d + d_{OC}\cos(\alpha_1 - \theta_y)}{d_{CD}}
\end{aligned}$$

$$\begin{aligned}
M_{11} &= m_x \\
M_{12} &= m_y l_y \sin\theta_y - m_z l_z \cos\theta_z \sin\theta_y \\
M_{13} &= -m_z l_z \sin\theta_z \cos\theta_y \\
M_{21} &= m_y l_y \cos\theta_y - m_z l_z \cos\theta_z \sin\theta_y \\
M_{22} &= m_y l_y^2 + J_{yy} + m_z l_z^2 \cos^2\theta_z \\
M_{31} &= -m_z l_z \sin\theta_z \cos\theta_y \\
M_{33} &= m_z l_z^2 + J_{zz}
\end{aligned}$$

$$\begin{aligned}
C_{12} &= -m_y l_y \dot{\theta}_y \cos\theta_y - m_z l_z \dot{\theta}_y \cos\theta_z \cos\theta_y \\
C_{13} &= -m_z l_z \dot{\theta}_z \cos\theta_z \cos\theta_y + 2 m_z l_z \dot{\theta}_y \sin\theta_z \sin\theta_y \\
C_{22} &= -\frac{1}{2} m_z l_z^2 \dot{\theta}_z \sin(2\theta_z) \\
C_{32} &= \frac{1}{2} m_z l_z^2 \dot{\theta}_y \sin(2\theta_z)
\end{aligned}$$

$$G_{11} = \frac{m_x g}{d} + k_2$$
$$G_{22} = \frac{m_y g l_y \cos\theta_y + m_z g l_z \cos\theta_z \sin\theta_y}{\theta_y} + k_1 l_y^2$$
$$G_{33} = \frac{m_z g l_z \sin\theta_z \cos\theta_y}{\theta_z} + k_1 l_z^2$$

The nonlinear mathematical model given in (3.38) can be expressed in state-space form as follows:

$$\dot{\boldsymbol{x}} = \boldsymbol{f}(\boldsymbol{x}, \boldsymbol{u}) = \boldsymbol{A}\boldsymbol{x} + \boldsymbol{B}\boldsymbol{u} \tag{3.39}$$

where $\boldsymbol{A} = \boldsymbol{A}(\boldsymbol{x})$, $\boldsymbol{B} = \boldsymbol{B}(\boldsymbol{x})$, $\boldsymbol{M} = \boldsymbol{M}(\boldsymbol{x})$, $\boldsymbol{C} = \boldsymbol{C}(\boldsymbol{x})$, $\boldsymbol{G} = \boldsymbol{G}(\boldsymbol{x})$, $\boldsymbol{T} = \boldsymbol{T}(\boldsymbol{x})$ and

$$\boldsymbol{A} = \begin{bmatrix} \mathbf{0}_{3x3} & \mathbf{I}_{3x3} \\ -\boldsymbol{M}^{-1}\boldsymbol{G} & -\boldsymbol{M}^{-1}\boldsymbol{C} \end{bmatrix}$$

$$\boldsymbol{B} = \begin{bmatrix} \mathbf{0}_{3x2} \\ \boldsymbol{M}^{-1}\boldsymbol{T} \end{bmatrix}$$

$$\boldsymbol{x} = [\ q \quad \dot{q}\ ]^T$$

$$\boldsymbol{u} = [\ F_y \quad F_z\ ]^T$$

As a last step, the linearisation procedure is implemented by using Taylor series expansion to represent the function as a power series consisting of zero order terms, first order terms, second order terms and higher order terms (Baruh, 2015).

Consider a Multiple Input Multiple Output (MIMO) nonlinear function as follows:

$$\dot{\boldsymbol{x}} = \boldsymbol{f}(\boldsymbol{x}, \boldsymbol{u}) \quad \Longrightarrow \quad \begin{aligned} \dot{x}_1 &= f_1(x_1, ..., x_n, u_1, ..., u_m) \\ &\vdots \\ \dot{x}_n &= f_n(x_1, ..., x_n, u_1, ..., u_m) \end{aligned}$$

$$\boldsymbol{y} = \boldsymbol{g}(\boldsymbol{x}, \boldsymbol{u}) \quad \Longrightarrow \quad \begin{aligned} y_1 &= g_1(x_1, ..., x_n, u_1, ..., u_m) \\ &\vdots \\ y_n &= g_n(x_1, ..., x_n, u_1, ..., u_m) \end{aligned}$$

and suppose that $\bar{x}_1$, $\bar{x}_2$, $\cdots$, $\bar{x}_n$, $\bar{u}_1$, $\bar{u}_2$, $\cdots$, $\bar{u}_m$ are the equilibrium points such that $f_i(\bar{x}_1, ..., \bar{x}_n, \bar{u}_1, ..., \bar{u}_m)= 0, \forall i \in(1, 2, ..., n)$. The system stops moving at the equilibrium point as all the f_i functions are equal to zero. To linearise the f_i functions about the equilibrium point, the following Taylor's equation can be used

$$f_i(x_1, ..., x_n, u_1, ..., u_m) \approx \sum_{j=1}^{n} \frac{\partial f_i}{\partial x_j}\bigg|_{x_j=\bar{x}_j} (x_j - \bar{x}_j) + \sum_{j=1}^{m} \frac{\partial f_i}{\partial u_j}\bigg|_{u_j=\bar{u}_j} (u_j - \bar{u}_j) + \text{higher-order terms} \tag{3.40}$$

where for the case of x sufficiently close to $\bar{x}$, the second and higher-order terms will be very close to zero, and hence, they can be neglected to obtain a suitable approximation (Seborg et al., 2016). Additionally, $f_i(\bar{x}, \bar{u})= 0$. Then, the perturbation state (also known as delta state) is defined as $\delta x_j = x_j - \bar{x}_j$ (for $1 \leq j \leq n$) to complete the linearisation, and using the fact that $\delta u_j = u_j - \bar{u}_u$ (for $1 \leq j \leq m$), the linearised model is obtained by

$$\delta \dot{x}_i = \sum_{j=1}^{n} \frac{\partial f_i}{\partial x_j}\bigg|_{x_j=\bar{x}_j} \delta x_j + \sum_{j=1}^{m} \frac{\partial f_i}{\partial u_j}\bigg|_{u_j=\bar{u}_j} \delta u_j \tag{3.41}$$

Therefore, the form of the linearised model can be given as

$$\dot{\boldsymbol{x}} = \boldsymbol{A_{lin}}\boldsymbol{x} + \boldsymbol{B_{lin}}\boldsymbol{u} \tag{3.42}$$

where

$$a_{ij} = \frac{\partial f_i}{\partial x_j}\bigg|_{x=\bar{x},\ u=\bar{x}} \quad \text{and} \quad b_{ij} = \frac{\partial f_i}{\partial u_j}\bigg|_{x=\bar{x},\ u=\bar{x}} \tag{3.43}$$

are the components of the $\boldsymbol{A_{lin}}$ and $\boldsymbol{B_{lin}}$. For the equilibrium point of the FJ-TVC system, $\bar{x} = [(m_1 + m_2 + m_3)g/k_2 \ 0 \ 0 \ 0 \ 0 \ 0]^T$ and $\bar{u} = [0 \ 0]^T$, the linearised model is given in A.1 (Appendix A), which will be used for the control system design of the FJ-TVC system in the following chapters.

3.5 Summary

This chapter firstly introduced the commonly used mathematical modelling methods. It then reviewed the elements included in the dynamic model used in previous studies and discusses the limitations of previous work. In contrast to the literature, this study develops a novel approach to dynamic modelling of the FJ-TVC system including translational motion of the pivot point in the x-axis. Therefore, in the last section, the derivation of mathematical model for the FJ-TVC system has been obtained by using the Lagrangian method and all the assumptions made in accordance with the system

model are listed. This derived dynamic model of the FJ-TVC covers the orientation of nozzle in a better manner and avoids the misalignments due to the displacement of the pivot point in the flight axis. The outstanding difference as a feature of the developed dynamic model is that it includes the displacement of the pivot point, d, in addition to the rotational motion of the nozzle. Also, the closed kinematic equation of the nozzle is given and the variation of the total length of the actuator is outlined according to the boundary conditions of the nozzle position.

This new model forms the basis for the new control laws and experimental validation given in the remaining chapters.

Chapter 4

Controller Design of the FJ-TVC System

In the previous chapter, a novel dynamic model for the FJ-TVC system including previously neglected terms was developed. Therefore, it includes the effects arising from the pivot point displacement in the vertical direction and covers previously unmodelled dynamical behaviours.

This chapter, as a next step, gives the theoretical foundation of conventional and modern controllers developed for the FJ-TVC system. In the initial section, a brief review of control methods including their advantages, limitations and up-to-date research are discussed. Then, two different controllers are designed which are the PID-BB conventional and the CTCL model-based methods. In addition, this chapter also describes the joint space dynamics form used in CTCL for the sake of completeness and discusses well known CTCL designs in detail.

4.1 A Review of Controller Design

In history of the control algorithm development, control methods can be divided into two groups: classical and modern control. Firstly, the classical, also termed conventional, control method is an uncomplicated way of designing a controller, however, its capacity is limited for systems including, e.g., nonlinear behaviours with uncertainties. Conversely, a model-based controller is also used frequently as it achieves better control performance in addition to its straightforward design.

An FJ-TVC system can be considered as a robotic application that requires high speed and accurate tracking control simultaneously. However, the disturbances on the joints, uncertainties and strongly coupled nonlinear dynamics affect the system performance adversely. In the last decades, many modern and intelligent control algorithms have been

developed for nonlinear systems (Goodwin et al., 2000) such as sliding mode control, adaptive control, neural network, fuzzy control, computed torque control. Nevertheless, there is no single study for controlling the FJ-TVC system. There are only a few control methods applied for the movable nozzle TVC systems which specifically cover the GJ-TVC system. In addition, most of the developed controllers rely on classical approaches as detailed below.

An example of a classical control approach in the literature is (Schinstock et al., 1998) which uses a conventional PID controller for the position control of a movable nozzle and a PI controller for the current control of the actuator. However, the controller design does not include modelling and parametric uncertainties in the system model. Lazić and Ristanović (2007) designed a conventional PI controller for the electro-hydraulic thrust vector control of twin rocket engines. Nevertheless, this study also did not consider uncertainties.

Li et al. (2011) have used a conventional control technique, which is a PID-BB controller, to control of the nozzle orientation. This control technique achieves an excellent performance output with a settling time of 0.16 seconds, a steady-state error of zero and an overshoot of zero. However, nonlinearities, disturbances and uncertainties have not been considered in the controller design.

As an alternative to classical approaches, Yu and Shu (2017) have studied Sliding Mode Controller (SMC) with PID control for the control design of a movable nozzle TVC system. Although it is a well-known and powerful method, some bounds on dynamic model uncertainties have to be pre-estimated very well (Shi et al., 2008). Furthermore, chattering is undesirable issue in the practice as it demands high control activity and may excite high-frequency unmodeled dynamics.

There are different modern and intelligent control algorithms in the literature such as artificial neural networks, fuzzy logic systems, robust control and computed torque control method. The artificial neural network controller is trained to learn from the process I/O data, however it is difficult to design the number of middle layers of a network, see (Kim et al., 2000; Ghrab and Kallel, 2013). In addition, fuzzy control is an applicable method for nonlinear systems as used in (Kasabov, 1996), nevertheless, optimisation issues occur on the design and analysis of the appropriate fuzzy rules. Additionally, several robust controllers for the control of robot manipulators are developed such as those based on uncertainty and disturbance estimation (Kolhe et al., 2013; Stobart et al., 2011), adaptive control (Huang and Chien, 2010) and the CTCL for fully actuated manipulators (Nguyen-Tuong et al., 2008; Sabet et al., 2017) and for underactuated systems (Udawatta et al., 2003; Zelei et al., 2011).

In this thesis, all the control methods are not extensively discussed, but as a conventional control design a PID-BB controller is considered which is a well known approach in aerospace applications (Li et al., 2011). Alternatively, CTCL is developed which is a

model-based control method used for time-varying, multi-variable, highly coupled multi-input multi-output (MIMO) manipulators (Lewis et al., 2003; Spong et al., 2006; Zelei et al., 2011). Motion control by the evaluation of computed torque on the joints gives high-performance rotational or translational control. Within this method, the coupled and non-linear equations of motion are converted into a linear model and the tracking error can be controlled by a feedback loop. For most model based controllers, especially for the CTCL, how to design the controller is crucial to achieving excellent tracking control. In Figure 4.1, the block diagram of the CTCL is given.

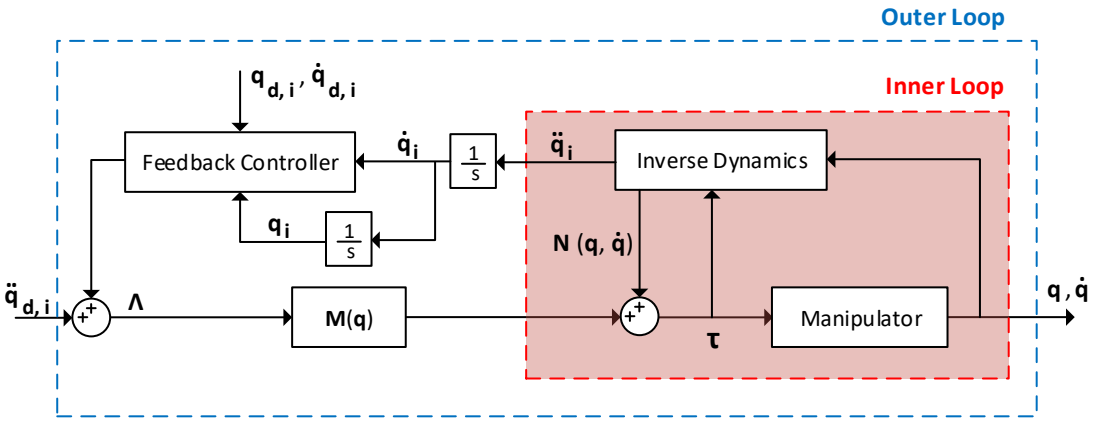

FIGURE 4.1: General block diagram of the CTCL method (Lewis et al., 2003).

A CTCL scheme has two parts as shown in Figure 4.1, where in the compensation part, also called the inner loop, the nonlinear inverse dynamic equations are evaluated. The output of the inverse dynamics equations, $\ddot{\mathbf{q}}_\mathbf{i}$, are evaluated by using (3.30), where the subscript $(.)_\mathbf{i}$ indicates the generalised coordinates of the system. Then, the output is provided into the feedback controller after the integration processes for position and velocity signals. The $\mathbf{q_{d,i}}$, $\dot{\mathbf{q}}_{\mathbf{d,i}}$ and $\ddot{\mathbf{q}}_{\mathbf{d,i}}$ are the position, velocity and acceleration of the desired generalised coordinates, respectively, depending on the prespecified trajectory. In the outer loop of the controller, stabilisation of the system is achieved and hence, according to the evaluated required force/torque value, the actuator applies the required torque $\boldsymbol{\tau}$ to the manipulator for the following desired trajectory. In this control scheme, Λ is defined for ease of understanding, which is equal to the summation of $\ddot{\mathbf{q}}_{\mathbf{d,i}}$ and the output of feedback controller. It is also concluded that the position and velocity control in the outer loop plays a critical role for the determination of the required force/torque. The feedback control method with a conventional PD or PID control in its outer loop theoretically guarantees globally, asymptotically stable trajectory tracking control, if the mathematical model of the system exactly matches the actual dynamic model of the manipulator (Aydogan et al., 2018). Yet, the tracking performance in practice dramatically decreases if the system model is imperfect or time-varying. For such systems a robust controller used in a CTCL method is the best solution (Prattico et al., 2014). Some examples are Robust $\mathcal{H}_\infty$, neural network CTCL (Rahmani and

Ghanbari, 2016), adaptive CTCL (Shang et al., 2012), adaptive fuzzy CTCL (Chen et al., 2012) and sliding CTCL (Diaz et al., 2012), where the outer loop is varying depending on the controller method.

The next section develops the PID-BB controller for the FJ-TVC system. The modern controllers developed in the remaining sections will be used for the benchmarking of control performance on the same dynamic model.

4.2 Conventional Controller Design

Linear classical control is a mature subject with a variety of powerful methods and a long history of successful industrial applications. This section develops the PID-BB controller which is a conventional controller previously designed for a movable nozzle TVC system (Li et al., 2011). However, the dynamic model in the study neglects the crucial terms resulting from the displacement of the nozzle. Therefore, it cannot guarantee excellent tracking performance.

The purpose of the bang-bang controller design in this section is to improve the rapidity of the dynamic response of the FJ-TVC system. It is also supported by the classical PID controller with a phase-lead compensator and hence, the compound control law composed of classical and bang–bang control achieves the switching error as soon as possible with the minimal steady state error, overshoot and rise time depending on the design criteria of the controller. Another reason for the bang-bang controller design is to benchmark the controller performance of TVC system when the pivot point displacement is included as in the dynamic model derived in the Section 3.3 and the case where it has not included as in (Li et al., 2011).

In the MIMO FJ-TVC system, the vertical displacement of the pivot point is coupled with the forces applied over the the nozzle in the yaw and pitch-axes. The force acting on the pivot point displacement is, correspondingly, evaluated by the actuator forces, F_y and F_z, as given in (3.31). Consequently, the transformation equations derived in (3.36) are used to convert the MIMO FJ-TVC system to the DIDO FJ-TVC system, which are given under the transformation matrix block in Figure 4.2.

In this control scheme, e_i, where $\{i \in 1, 2\}$, represent the angular errors of the nozzle in the yaw and pitch axes, respectively. These errors are evaluated by subtracting the nozzle angle from the desired angular input, which are measured in degrees. The determined position errors are then fed to the position controller where the bang-bang or the PID with phase-lead compensator are the options. If the error signal e_i is greater than the defined switching error e_{sw} value, the bang-bang controller is activated. The bang-bang controller is known as an on-off controller that switches abruptly between two states. This controller frequently arises in minimum-time optimal control problems

and applies maximum boundary conditions until the unique switching error is achieved. Alternatively, when the input error decreases to the e_{sw}, then the PID controller with phase-lead compensator is activated. Therefore, the output signal of the controller is passed to the saturation block which imposes upper and lower bounds of the signal and linked to the actuator driver card where the speed and current controllers exist. The PID with phase-lead compensator computes an update of the control input. This process continues while the controller is in effect. It should be noted that the determination of the nozzle angle relies on the kinematic transformation equations in (3.35). Also, even though the input variables of the transformation matrix in Figure 4.2 are d, θ_y and θ_z, respectively, which are the data provided by the feedback sensors such as laser sensor and encoder, the variables $\theta_{y,n}$ and $\theta_{z,n}$ correspond to the nozzle angles in yaw and pitch axes, respectively.

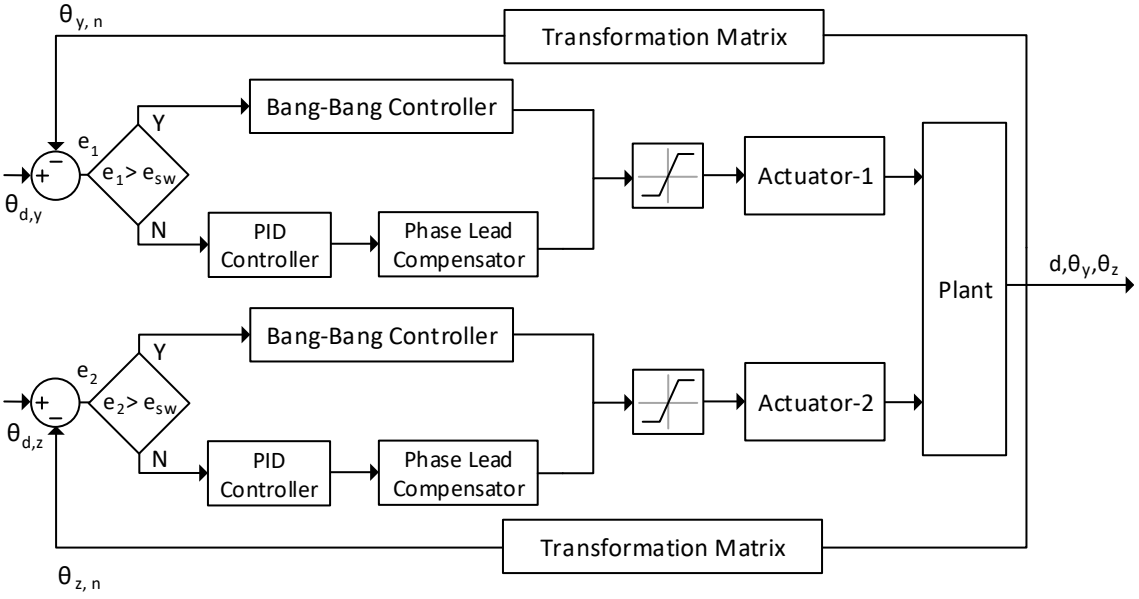

FIGURE 4.2: Block diagram of the PID-BB conventional control method implemented for the FJ-TVC system.

The output of a PID controller, which is equal to the control input to the plant, is calculated in the time domain from the feedback error as:

$$u(t) = K_p e_i(t) + K_i \int_0^t e_i(t)dt + K_d \dot{e}_i(t) \tag{4.1}$$

where K_p, K_i and K_d are the gains of each component of the PID controller.

A PID controller computes both the derivative and the integral of the error signal with respect to time. The control signal u to the plant is equal to the proportional gain K_p times the magnitude of the error plus the integral gain K_i times the integral of the error plus the derivative gain K_d times the derivative of the error.

The transfer function of a PID controller is found by taking the Laplace transform of (4.1) as:

$$K_p + \frac{K_i}{s} + K_d s = \frac{K_d s^2 + K_p s + K_i}{s} \tag{4.2}$$

In the PID control, a saturation might occur due to the increase in the integral action when the input signal is larger than the actuators capacity. In such cases, the increase in integral action causes a deterioration on the controller performance such as large oscillations or even instability. This phenomena is called windup. As a counter-effect of the windup, anti-windup design algorithms are developed in the last decades, back calculation and clamping are examples of those algorithms, for further details, see (Azar and Serrano, 2015; Cao et al., 2002; Galeani et al., 2009). However, anti-windup design is not covered in this controller, and is suggested for future work.

A phase-lead compensator is also used in this control approach as it increases the stability and the speed of response time (Li et al., 2011). This compensator is usually designed for a system in a transfer function form. A first-order lead compensator $C(s)$ can be designed using the root locus. A lead compensator in a general form is given by

$$C(s) = K_c \frac{(s - z_0)}{(s - p_0)} \tag{4.3}$$

where the magnitude of z_0 is less than the magnitude of p_0. A phase-lead compensator shifts the root locus toward to the left in the complex s-plane. The role of the compensator is to improve the system's stability and decrease the response time. Also, the closed-loop bandwidth of the controller is increased, leading to transient response improvements. With the same purpose, Li et al. (2011) aim to decrease the response time by using a compensator. Conversely, the disadvantage of the controller is that the increase of the bandwidth makes the system more sensitive to noise and it may amplify high frequency noises.

In conclusion, a bang-bang controller is used at the initial stage to reduce the tracking error until unique switching error e_{sw} is achieved. Then, a PID controller with phase-lead compensator controls the plant input to provide accurate tracking control.

The next section develops PD-CTCL and $\mathcal{H}_\infty$-CTCL designs for the control of FJ-TVC system.

4.3 Design of Computed Torque Controller

CTCL, also termed static non-linear state feedback control or inverse dynamics control, is widely used for the control of nonlinear manipulators. Since most nonlinear mechanical systems comprise driven motors, coupling gears or nonlinear mechanisms, the complexity

of systems makes the design of controllers a difficult task. However, via inverse dynamics, the CTCL method compensates the nonlinear dynamic terms in the model and decouples the interactions between the degrees of freedom (Chung et al., 2008).

The underlying idea of the CTCL method is to use the existing knowledge of the dynamic model of the system and decouple the manipulator joint dynamics. Hence, the motion of each joint can be individually controlled using well developed control strategies and by this way potentially higher tracking accuracy, lower feedback gains, and lower energy consumption are achieved. There are two main difficulties in the use of CTCL. The first is the high computation requirement of the systems to achieve fast response time. Secondly, a highly accurate dynamic model is required for globally, asymptoticially stable trajectory tracking control. To counter the effect of nonlinearities and disturbances in the system model, uncertainties are introduced for the control loop and robust controllers are used to stabilise the outer loop of the CTCL design.

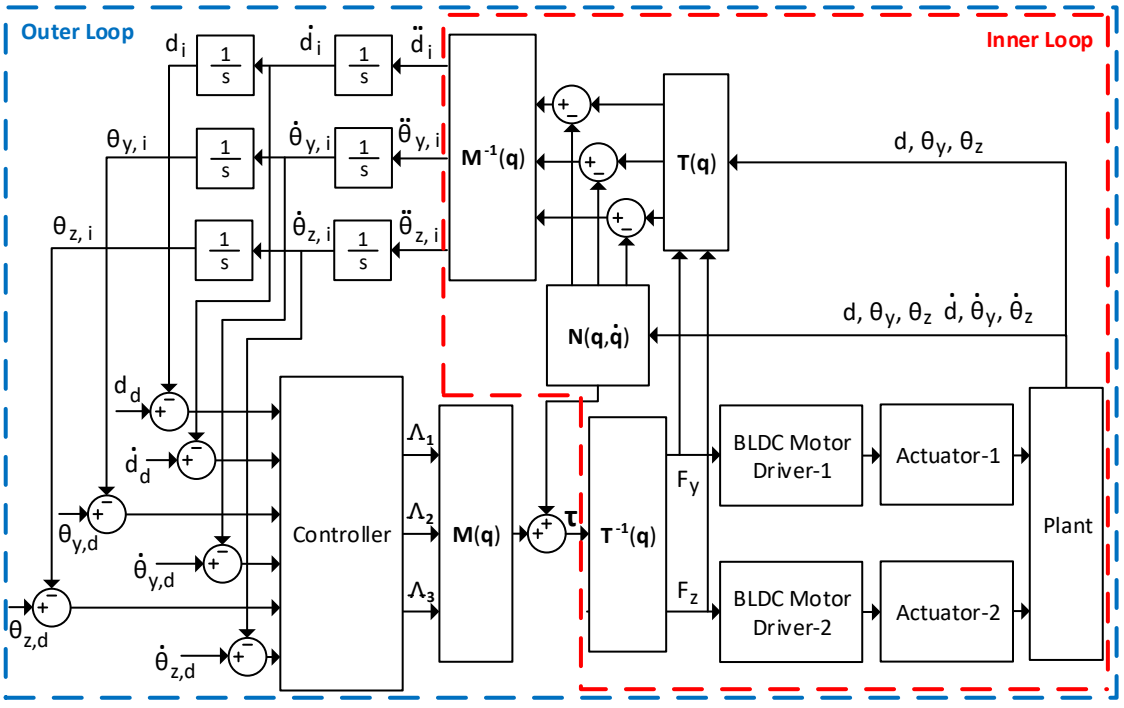

FIGURE 4.3: Block diagram of the computed torque control law implemented for the FJ-TVC system.

The resulting control design is illustrated in Figure 4.3. In the block diagram of the controller, $\mathbf{M}(\mathbf{q})$ and $\mathbf{N}(\mathbf{q}, \dot{\mathbf{q}})$ are the matrices derived in the dynamic model of the system given in (3.37). $\mathbf{T}(\mathbf{q})$ is the transformation matrix given in (3.36), and its inputs are the variables provided by the feedback sensors. The second derivatives of the generalised coordinates are, therefore, evaluated by using (3.38), which are the outputs of inverse dynamics equations, i.e., $\ddot{d}_i$, $\ddot{\theta}_{y,i}$ and $\ddot{\theta}_{z,i}$. Also, the reference inputs, in other words the components of the desired trajectory, are d_d, $\theta_{y,d}$, $\theta_{z,d}$, respectively, where their derivatives are $\dot{d}_d$, $\dot{\theta}_{y,d}$, $\dot{\theta}_{z,d}$ and their second derivatives are $\ddot{d}_d$, $\ddot{\theta}_{y,d}$, $\ddot{\theta}_{z,d}$. Additionally,

Λ is defined for ease of understanding, which is equal to the summation of $\ddot{\mathbf{q}}_\mathbf{d}$ and the output of the feedback controller, see Figure 4.4 for details where PD controller is used as a feedback controller. Consequently, to evaluate the required force/torque, Λ is multiplied by $\mathbf{M}(\mathbf{q})$ and then sum up with $\mathbf{N}(\mathbf{q}, \dot{\mathbf{q}})$, which gives τ_1, τ_2 and τ_3 corresponding to F_d, M_{θ_y} and M_{θ_z}, respectively. As a result, the required force/torque data are transformed to the F_y and F_y by using the inverse transformation matrix, $\mathbf{T^{-1}}(\mathbf{q})$. It is crucial to note that the CTCL design includes an inner nonlinear loop and additionally an outer control loop where the required force/torque is evaluated based on the position and velocity errors of the generalised coordinates.

In the next sections, derivation of inner feedforward loop is explained and then outer loop design alternatives are introduced.

4.3.1 Design of Inner Feedforward Loop

The dynamics of a system with rigid links was given in (3.37) where $\mathbf{q}$ is the vector of generalised coordinates of the system (d, θ_y, θ_z). The inner loop consists of the matrices $\mathbf{M}^{-1}(\mathbf{q})$ and $\mathbf{N}(\mathbf{q}, \dot{\mathbf{q}})$, which are in the nonlinear form as given in (3.39).

Introduce

$$\begin{bmatrix} x_1 \\ x_2 \\ x_3 \end{bmatrix} = \begin{bmatrix} d \\ \theta_y \\ \theta_z \end{bmatrix} \tag{4.4}$$

Then, the first derivatives of the state equations of the FJ-TVC system are defined as

$$\begin{bmatrix} \dot{x_1} \\ \dot{x_2} \\ \dot{x_3} \end{bmatrix} = \begin{bmatrix} x_4 \\ x_5 \\ x_6 \end{bmatrix} \tag{4.5}$$

and the second derivatives of state equations are

$$\begin{aligned} \dot{x_4} = M_{11}^{-1}(-N_1 + \tau_1) + M_{12}^{-1}(-N_2 + \tau_2) \\ + M_{13}^{-1}(-N_3 + \tau_3) \end{aligned} \tag{4.6}$$

$$\begin{aligned} \dot{x_5} = M_{21}^{-1}(-N_1 + \tau_1) + M_{22}^{-1}(-N_2 + \tau_2) \\ + M_{23}^{-1}(-N_3 + \tau_3) \end{aligned} \tag{4.7}$$

$$\begin{aligned} \dot{x_6} = M_{31}^{-1}(-N_1 + \tau_1) + M_{32}^{-1}(-N_2 + \tau_2) \\ + M_{33}^{-1}(-N_3 + \tau_3) \end{aligned} \tag{4.8}$$

which are derived from the general dynamic equation in (3.37). These second derivatives of the state equations specify the input in feedback controller after integration processes

to evaluate the position and velocity errors. The first integration of the state equations give $\dot{d}_i$, $\dot{\theta}_{y,i}$ and $\dot{\theta}_{z,i}$ which correspond to the velocity data obtained from the inverse dynamics equations of the system. Additionally, the second integration of the state equations give d_i, $\theta_{y,i}$ and $\theta_{z,i}$ which are the position data determined by the same approach. These variables are used in the feedback controller which is explained in the outer loop design in the next section.

4.3.2 Design of Outer Loop

The outer loop stabilizes the system by using a suitable controller and enforces tracking of the prescribed trajectory. As seen from Figure 4.3, the input of the feedback controller depends on $\mathbf{q}(t)$ and $\dot{\mathbf{q}}(t)$. There are several ways for choosing the input where commonly known techniques are such as conventional, optimal, robust and adaptive control. The next sections develops PD and $\mathcal{H}_\infty$ controller for the outer loop design of the CTCL method, respectively.

4.3.2.1 Conventional Method: PD Controller

Conventionally, control design of practical applications is as the tuning of a PD, PI or PID controller for the mechanical systems (Canudas-de Wit et al., 1997). Its history goes back to the study of tuning procedures for PID compensator (Ziegler et al., 1942). Especially in the industry, simple control methods are mostly preferable as they are easy to design and provide quick response, stability and small steady state error. Conversely, in such cases conventional control methods are unable to give significant enhancement as discussed in Section 4.1.

The commonly used conventional method for the control of robotic applications is the PD controller. It is a feedback mechanism combining two different components. Physical capacities of PD components are as follows: Proportional part, in certain cases provides a smooth control and an error that is almost zero in the steady state by the tuning of proportional gain (K_p). Then, the derivative part introduces damping into the system which is proportional to the signal error change rate. The selection of these parameters are crucial to achieve performance requirements. There are several tuning methods such as the Ziegler-Nichols method (Ziegler et al., 1942), Cohen-Coon parameters (Cohen, 1953), the Relay method (Åström and Hägglund, 1984). Most recent developments are given by Wang et al. (2002) who uses the Fast Fourier Transform (FFT) and by Jeon et al. (2010) who use a linear combination sub-relay signals with different frequencies or gains. However, the parameters obtained by these methods may not be suitable for all electromechanical systems and require fine tuning based on the system output.

The PD-CTCL method has a variety of advantages over first linearizing the dynamics and then applying linear control design, e.g., potentially higher tracking accuracy, lower

feedback gains, higher suitability for compliant control, lower energy consumption (Ma and Ghasemi-Nejhad, 2005). However, there is a requirement to have precise analytical models in order to predict the torques required for the execution of the trajectory.

In this method, a nonlinear feedback control provides tracking of the desired trajectory. The required torques and forces are calculated by using the following equation,

$$\tau = M(q)(\Lambda) + (N(q, \dot{q})) \tag{4.9}$$

where Λ depends on the chosen controller. In this case a PD controller is used. Hence $\Lambda = \ddot{q}_d + k_d\dot{e} + k_p e$ and the PD-CTCL is

$$\tau = M(q)(\ddot{q}_d + k_d\dot{e} + k_p e) + (N(q, \dot{q})) \tag{4.10}$$

resulting in the tracking error dynamics

$$\ddot{e} = -k_d\dot{e} - k_p e \tag{4.11}$$

where $\ddot{q}_d$ correspond to the desired acceleration of the generalised coordinates.

Moreover, the controlled system is stable provided k_p and k_d are positive diagonal matrices. It is common to select these gain matrices as diagonal and hence stability holds provided all diagonal entries are positive.

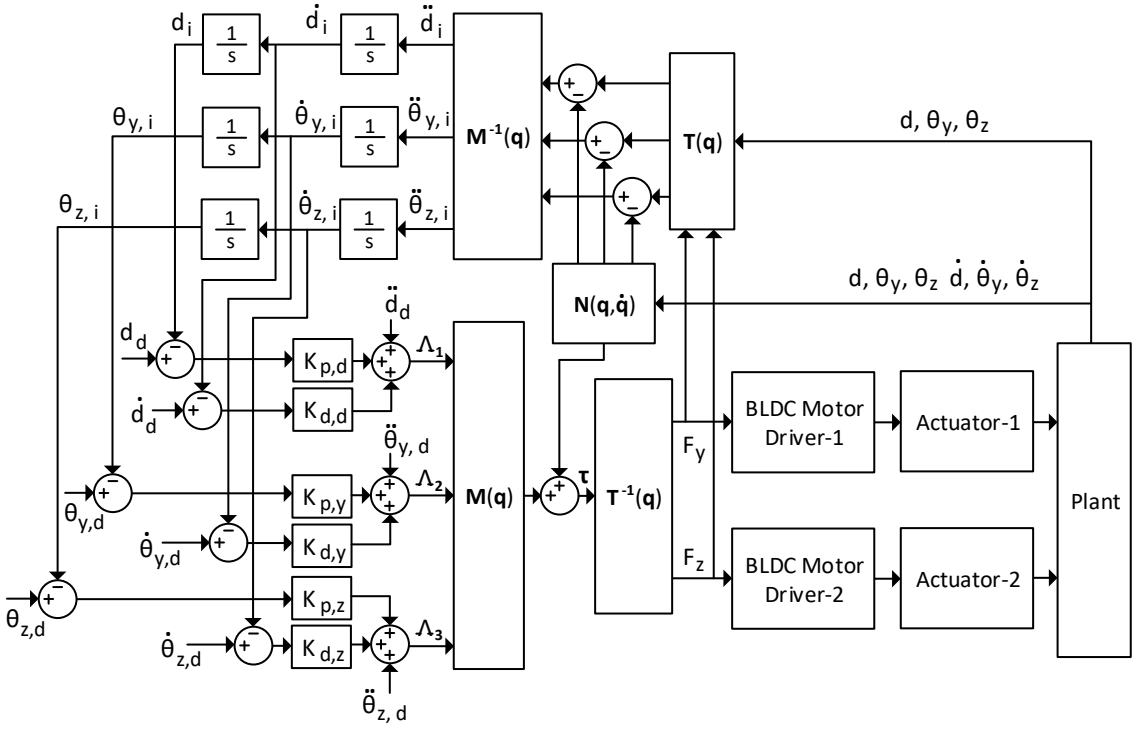

FIGURE 4.4: Components of the PD-CTCL design.

In Figure 4.4, the first component consists of a nonlinear inner loop where the generalised applied forces (actuator torques) are calculated and the equations of motion are solved by an integrator. This part of the controller design is essentially the inverse dynamics of the system. The second component is an outer loop which stabilises the system by using a PD controller that makes the system follow the specified trajectory. The outer-loop signal $\ddot{e}$ can be chosen using many approaches, including robust and adaptive control techniques. The notation used in Figure 4.4 holds the same meaning as that defined in Figure 4.3.

The error dynamics can be written as

$$\begin{bmatrix} e_1 \\ e_2 \\ e_3 \end{bmatrix} = \begin{bmatrix} q_{d,1} \\ q_{d,2} \\ q_{d,3} \end{bmatrix} - \begin{bmatrix} x_1 \\ x_2 \\ x_3 \end{bmatrix} \tag{4.12}$$

$$\begin{bmatrix} \dot{e}_1 \\ \dot{e}_2 \\ \dot{e}_3 \end{bmatrix} = \begin{bmatrix} \dot{q}_{d,1} \\ \dot{q}_{d,2} \\ \dot{q}_{d,3} \end{bmatrix} - \begin{bmatrix} \dot{x_1} \\ \dot{x_2} \\ \dot{x_3} \end{bmatrix} \tag{4.13}$$

and within the controller parameters

$$\Lambda = \begin{bmatrix} \Lambda_1 \\ \Lambda_2 \\ \Lambda_3 \end{bmatrix} = \begin{bmatrix} \ddot{q}_{d,1} + k_{d,1}\dot{e_1} + k_{p,1}e_1 \\ \ddot{q}_{d,2} + k_{d,2}\dot{e_2} + k_{p,2}e_2 \\ \ddot{q}_{d,3} + k_{d,3}\dot{e_3} + k_{p,3}e_3 \end{bmatrix} \tag{4.14}$$

the required torque/force parameters

$$\tau = \begin{bmatrix} \tau_1 \\ \tau_2 \\ \tau_3 \end{bmatrix} = \begin{bmatrix} M_{11}\Lambda_1 + M_{12}\Lambda_2 + M_{13}\Lambda_3 + N_1 \\ M_{21}\Lambda_1 + M_{22}\Lambda_2 + M_{23}\Lambda_3 + N_2 \\ M_{31}\Lambda_1 + M_{32}\Lambda_2 + M_{33}\Lambda_3 + N_3 \end{bmatrix} \tag{4.15}$$

can be determined, respectively. These force/torque values are fed to the BLDC actuator driver to follow the desired trajectory where the current controller is implemented.

The outer-loop design performed in this section is based on the conventional PD controller. The next section designs a robust $\mathcal{H}_\infty$ controller which is more powerful and able to compensate explicitly for the uncertainties and disturbances in the system model.

4.3.2.2 Robust Control Method: $\mathcal{H}_\infty$ Controller

In the fixed-parameter dynamic systems, which means system parameters in the model are time-invariant and accurately known, it is generally the case that inverse dynamics control or CTCL may become unstable in the presence of uncertainties. If the model

parameters are not exactly known but bounds on these parameters are available, robust control design can be applied. There are many robust control techniques such as sliding mode, direct passive, saturation-type and decoupled designs (Bellini et al., 1989; Diaz et al., 2012). Additionally, an adaptive control method could be applied which is a very powerful technique to automatically account for the uncertainties and disturbances present in system dynamics, see (Craig, 1986; Lewis et al., 2003) for further details.

This research only focuses on $\mathcal{H}_\infty$-CTCL design in this thesis as it achieves very accurate tracking control with the straightforward evaluation procedures for the outer loop design of CTCL. For the $\mathcal{H}_\infty$ design solution, the Linear Matrix Inequality (LMI) approach is used which has been proposed as an alternative approach to algebraic Riccati equations in the early 1990s. It is now well established from a variety of studies that the LMI solution makes the powerful numerical algorithms available for the $\mathcal{H}_\infty$ problem (Doyle et al., 1991; Beck, 1991). Within the existing developments, therefore, it has been demonstrated that the original $\mathcal{H}_\infty$ problem can be reduced to the formulation of convex optimization problem that is amenable to computer solution (Gahinet and Apkarian, 1994; Iwasaki and Skelton, 1994).

Let $G(s)$ denote the transfer-function of the Linear Time-Invariant (LTI), Multiple-Input and Multiple-Output (MIMO) system with the state-space realisation

$$\begin{aligned} \dot{x} &= Ax + B_1 w + B_2 u \\ y &= x \end{aligned} \tag{4.16}$$

where the inputs to G are the disturbance w and the input from the controller u. The outputs of G are the input to the controller y. The formulation of w is explained in (4.21) which basically relies on the differences between nominal and real values of the system parameters.

The control input u is state feedback, i.e.,

$$u = K_f x \tag{4.17}$$

where K_f denotes the controller to be designed.

The design problem is formulated with $||\cdot||_\infty$ denoting the $\mathcal{H}_\infty$ norm as

$$\|G\|_\infty = \sup_\omega \bar{\sigma}(G(j\omega)) < \gamma \tag{4.18}$$

where $\bar{\sigma}(\cdot)$ denotes the maximum singular value and $\gamma \in (0, 1)$.

In Figure 4.5, the block diagram of generalised plant for the $\mathcal{H}_\infty$ is depicted. Here, as it is known r is the reference input vector including q_d and $\dot{q}_d$, e is the vector of state errors, u is the vector of control inputs, K_f is the controller gain matrix and W_s, W_{cs} and W_t are the weighting functions. These functions are introduced to achieve the desired

behaviour of the system, i.e., W_s and W_t control the shape of the tracking and the closed loop behaviour, being the inverse of the sensitivity function S and the complementary sensitivity T. Additionally, W_{cs} is defined to shape the penalty on control signal use.

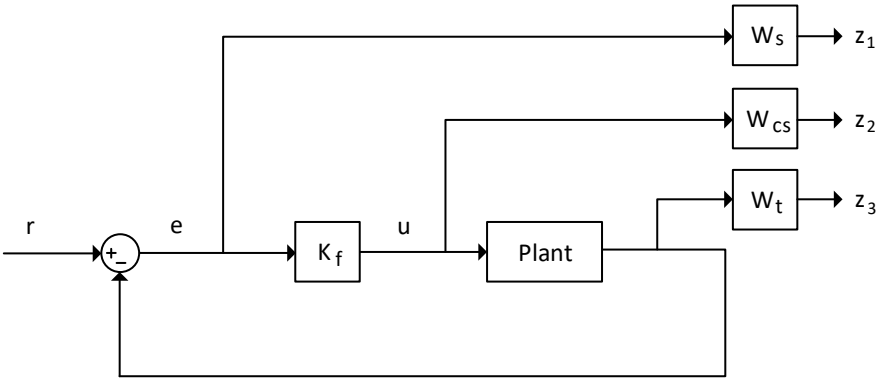

FIGURE 4.5: Block diagram of generalised plant model for the $\mathcal{H}_\infty$ control.

For good reference-tracking control, W_s is included in the $\mathcal{H}_\infty$ control which shapes the sensitivity function for reference tracking. Therefore, it describes the transfer function where the magnitude and frequency are dependent of the reference commands. Typically, W_s is flat at low frequency and rolls off at high frequency.

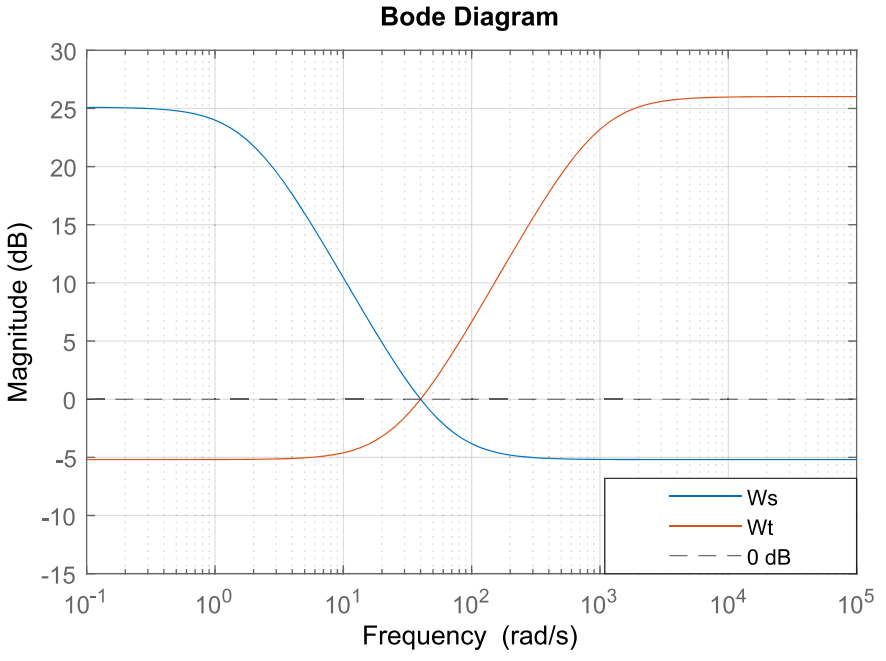

FIGURE 4.6: Weighting functions, W_s and W_t.

Secondly, W_t balances the difference between the response of the closed-loop system and the desired model. It is generally required that the system should have a good matching

of desired model at low frequencies whereas less accurate matching at higher frequencies. Bode diagrams of W_s and W_t are given in Figure 4.6.

Lastly, W_{cs} is defined to form the penalty on the control signal which is a frequency varying weighting function as well. It is utilised to limit the control effort. Bode diagram of W_{cs} is given in Figure 4.7.

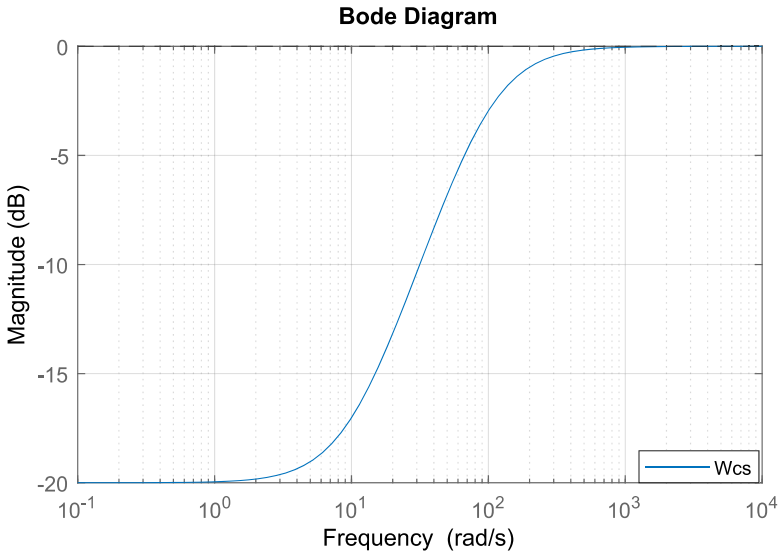

FIGURE 4.7: Weighting function, W_{cs}.

These weighting functions can be defined in MATLAB using the `makeweight` command, which provides a convenient means to specify weighting functions according to the target gain profiles and cut-off frequencies. Alternatively, the following formulation can be utilised to specify the weighting functions:

$$W = \frac{s + w_b/M_{cs}}{\varepsilon_1 s + w_b} \tag{4.19}$$

where w_b is the cut-off frequency, M_{cs} is the gain for high frequency disturbances and ε_1 is the control signal at low frequency (Helton and Merino, 1998).

The weighting functions can be tuned to achieve the desired trade-off between robustness and performance. This tuning is carried out through trial and error where the effect on the performance of the system is observed. The weighting functions, in this study, are chosen according to the control performance requirements of the system. The studies held by Beaven et al. (1996); Hu et al. (2000); Skogestad and Postlethwaite (2005) are worthwhile for a more in-depth discussion about the weighting function selection. Further synthesis such as loop-shaping design is planning to implement in the future work.

After specifying the system parameters and the weighting functions which are dependent on the application and the required behaviour of the system, the next step is to formulate

the optimisation problem. In MATLAB, `hinfsyn` function can compute the $\mathcal{H}_\infty$ optimal feedback controller K_f for the augmented plant with weighted functions. Alternatively, the LMI approach for the optimisation problem can be implemented for the controller design, see (Duan and Yu, 2013).

4.3.3 Modelling of Uncertainties

The modelling of uncertainties plays a crucial role to achieve a reliable result on the simulation studies. The parametric uncertainties are modelled using random variables and additionally, Monte Carlo simulation is performed to illustrate the effect of these parameters on the system model.

The parameters with uncertainties are modelled as follows:

$$\tilde{K}_i(\Omega) = \tilde{k}_i + \tilde{k}_i \sigma_i \xi(\Omega) \tag{4.20}$$

where for each parameter k_i is the mean, σ_i is the largest percentage deviation from the mean, ξ is the normal random variable and Ω is a random process. The normal random variable is derived by the normal probability distribution function. It is then used to evaluate the uncertain parameters.

Based on the largest percentage deviation of the parameters, the uncertainties are implemented in a MATLAB/Simulink model by using uncertain state space block where uncertain system variables exist within their percentage range. Consequently, the state-space realisation of the FJ-TVC system is extended as

$$\begin{aligned} \dot{x} &= Ax + B_1 w + B_2 u \\ w &= \Delta(\tau - \ddot{q}_d) + M^{-1}\delta \\ \Delta &= M^{-1}\tilde{M} - I_n \ , \ \delta = N - \tilde{N} \end{aligned} \tag{4.21}$$

where $\tilde{}$ sign indicates the matrices that include uncertain parameters. Also, M and N are the matrices determined in (3.38) where $N(q, \dot{q})$ corresponds to $C(q, \dot{q}) + G(q)$. It is, therefore, concluded that if $M = \tilde{M}$ and $N = \tilde{N}$, then Δ and δ will be equal to zero, i.e., the corresponding disturbance w will be equal to zero. Conversely, depending on the differences between nominal and real values of the system parameters, a disturbance effect occurs over the system performance.

The Monte Carlo simulation analyses the maximum and minimum values of the matrices in transfer function by creating Latin hypercube samples in MATLAB. This allows sampling the random variables to evaluate the effect of the uncertainties for the system

model in (4.21) which is formed as follows:

$$\dot{x}_{max} = Ax + \max B_1(\Omega)w + \max B_2(\Omega)u \qquad (4.22)$$
$$\dot{x}_{min} = Ax + \min B_1(\Omega)w + \min B_2(\Omega)u$$

and includes the maximum and minimum values due to the uncertainties and disturbances. The controller designs developed for the FJ-TVC system, therefore, take into account the boundary conditions of the system including uncertain parameters. The real values of the system parameters and their mean and deviation values are given in the next chapter.

4.4 Summary

This chapter gives a survey of the current status of controller design for TVC systems. It is concluded that there are only a few control methods developed for movable nozzle TVC systems, and all of them specifically consider the GJ-TVC system as a dynamical model which neglects the significantly different behaviours in FJ-TVC. In addition, most of the studies developed a controller design for movable nozzle TVC system use a conventional control method, such as a PID controller (Schinstock et al., 1998), PI controller (Lazić and Ristanović, 2007), PID-BB controller (Li et al., 2011). Conversely, sliding mode controller with PID control has been developed in (Yu and Shu, 2017) where a similar conventional dynamic model has been used.

This chapter also develops a conventional controller which is the PID-BB controller. Then the CTCL method is used as an alternative for the control of an FJ-TVC system. The CTCL method, in principle, compensates the nonlinear dynamic terms in the model, decouples the interactions between the degrees of freedom and hence, achieves better tracking control. Moreover, the outer loop design is an essential part of the CTCL design. Therefore, well-known control methods for the design of outer feedback loop are developed which are PD and robust $\mathcal{H}_\infty$ controller. Additionally, the approach for the uncertainty modelling of the uncertain variables is described. The approach relies on the implementation of uncertain variables by using uncertain state space block in MATLAB/Simulink.

The developed control algorithms in this chapter are used in the simulation and experimental studies in the next chapters.

Chapter 5

MATLAB and Simulink Implementations

In the previous chapter, the theoretical background of conventional (PID-BB) and the model-based (PD-CTCL and $\mathcal{H}_\infty$-CTCL) were controllers developed for the considered system.

This chapter, firstly, defines the system requirements and specifications for the simulation studies of the FJ-TVC system. Following this, the controllers from the last chapter are simulated in a MATLAB/Simulink environment where each controller is tested for two different system models, the initial model assumes the FJ-TVC system is precisely known, whereas the second considers the uncertainties in addition to its nominal model. Within this framework, the performance result of each controller is discussed in detail.

5.1 System Requirements and Design Criteria

This section defines the functional and control performance requirements of the FJ-TVC system to be fulfilled during operation. These requirements play a pivotal role in the design of controllers. This is because, the purpose of this study is to provide a more robust and competitive controller when compared to similar systems which were previously surveyed in Section 2.2. The requirements are given in Tables 5.1 and 5.2.

TABLE 5.1: Application specific requirements

Parameter	Definition	Value	Unit
θ_y	Thrust vectoring on yaw axis	± 4	deg
θ_z	Thrust vectoring on pitch axis	± 4	deg
d	Vertical displacement of pivot point	0.004	m

TABLE 5.2: Control performance requirements

Parameter	Definition	Value	Unit
e_{ss}	Maximum allowable steady state error for each axis	0.2	deg
t_s	Maximum allowable settling time for each axis	0.2	sec
t_r	Maximum allowable rise time for each axis	0.1	sec
p_o	Maximum allowable percent overshoot	5	pct

The specific requirements defined here play the key role for the system performance. Most of the requirements are obtained from similar studies in the literature, see (Lampani et al., 2012; Li et al., 2011; Swain et al., 2019; Chunguang et al., 2020). More specifically, it is concluded from (Li et al., 2011) that the displacement of the pivot point is bounded and lies within a certain margin. As a case study, it is concluded from the finite element analysis, the evaluated pivot point displacement is 2 mm for a system with the inner diameter of 250 mm. So, it is approximately equal to 0.8% of the internal diameter.

Conversely, the result obtained from experimental test of (Swain et al., 2019) shows that the deformation of the flexible joint under different chamber pressures causes a displacement of the pivot point which is less then 80 mm for a system with an internal diameter of 1500 mm. For this specific case, the displacement corresponds to 6% of the internal diameter of the system. Although, the deformation of the flexible joint is also affected by the thickness of the elastomer layer and the number of spherical metallic sheets used between them, the results obtained from these studies give an approximate value for the displacement of pivot point. Additionally, Swain et al. (2019) concludes that the asymmetric deformation of flexible joint is at a negligible level when compared to the axial displacement. Based on this information, the vertical displacement of the pivot point is defined as 4 mm in the experimental and simulation studies in this thesis.

A few circumstances occuring in the FJ-TVC system have not been considered in the performance requirements of the study. The assumptions and design criteria adopted for the simulation of the FJ-TVC system are listed as follows:

- The vibrations arising from jet noise, aeroelastic effects and the radial displacement of the nozzle pivot point in the y- and z-axes are neglected;
- The actuators and the feedback sensors are stable, so that all the poles of the transfer functions corresponding to components are in the open left half-plane;
- The avionics, including the BLDC actuator driver are fast relative to the other elements in the control loop, therefore, the delays due to the avionics are neglected;
- The nonlinearities in the dynamics of feedback sensors are neglected;
- The slew rate of the actuator is sufficient to satisfy the control performance requirements;

- The measurement rates of feedback sensors are sufficient to satisfy the operating frequencies of the corresponding control loops;
- The stroke of the actuator is adequate to steer the nozzle at maximum nozzle angle ± 4;
- The actuator used in the system should draw maximum 5 A current which is the current limit of the actuator to avoid any damage on the test-rig made of plastic materials;
- The saturation limit of the actuator is set to 24 V as the actuators voltage limit is 24 V; and
- The system should be able to track sinus command with the magnitude of 0.8 degrees at 5 Hz, where 0.8 degrees is the 20 percent of the maximum rotation angle of the nozzle.

5.2 Controller Design of the BLDC Actuator

This section gives the proposed controller design for the the BLDC actuator utilised in the MATLAB/Simulink implementations. Even though the custom-design BLDC actuator driver card and its commercial software used in the experimental setup provide an interface for the tuning of controller parameters over the existing controller structure, this section firstly gives the BLDC actuator model and then describes the details of controller design implemented for the actuator.

Table 5.3 shows the necessary parameters used in the controller design for the Faulhaber 3268-BX4 BLDC actuator. It is worth noting that the system parameters given in this section are the nominal values of the components.

TABLE 5.3: DC motor parameters.

Parameter	Definition	Value	Unit
R	Resistance	1.47	Ohm
L	Inductance	110×10^{-6}	Henry
L_b	Pitch of ball screw	2×10^{-3}	m
K_t	Motor torque constant	43.3×10^{-3}	N.m/A
K_r	Stiffness of the drive rod	2×10^{8}	N/m
K_e	Electromotive force constant	43.3×10^{-3}	V/rad/sec
J_m	Moment of inertia of the rotor	63×10^{-6}	kg.m^2
τ_e	Electrical time constant	7.5×10^{-5}	sec
τ_m	Mechanical time constant	4.9×10^{-3}	sec

Initially, the BLDC actuator model with the six-step inverter is shown in Figure 5.1. For the sake of clarity, the details of the blocks are given seperately in Appendix C, see Figure C.1 for the six-step inverter model, Figure C.2 for the BLDC model and Figure C.3 for the back EMF output details.

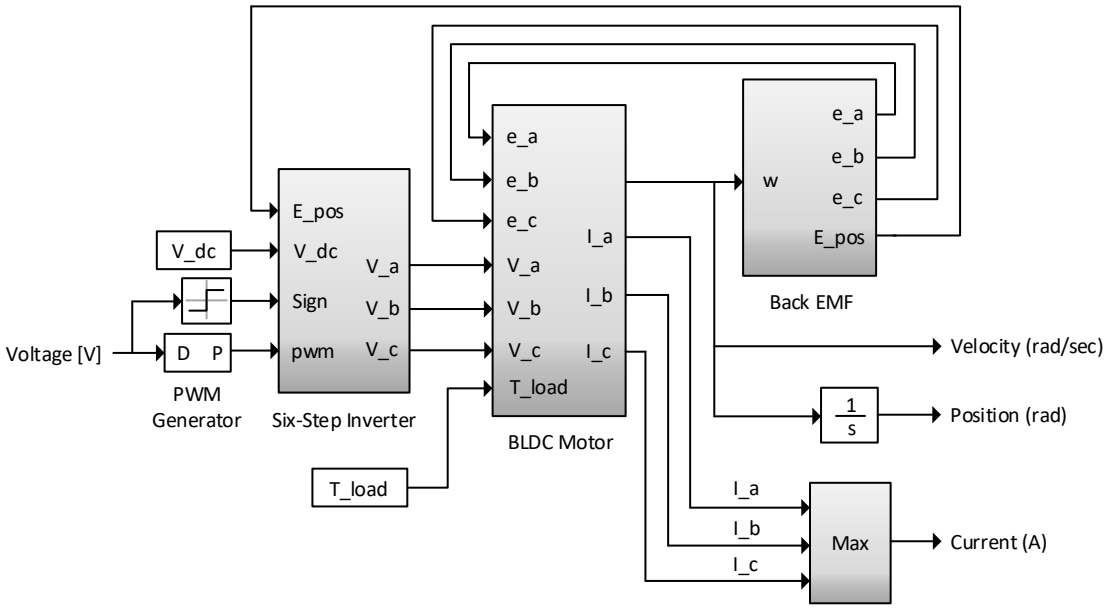

FIGURE 5.1: Block diagram of the BLDC actuator with six-step inverter and back EMF

The model given in Figure 5.1 is developed for observing speed and current characteristics of the BLDC actuator. The actuator operates in accordance with the six-step commutation sequence. Each phase of the actuator is excited by a hall effect sensor and at each sequence, only two phases are energised where the third phase is non-energised. Based on the signal detected by the hall effect sensor, the controller generates a proper gating signal to the switches of the inverter. Then, the actuator starts to rotate.

As a next step, the step response of the current/voltage transfer function of the actuator is plotted, see Figure 5.2. It is set out to investigate the current output when the unit input voltage is supplied. What stands out in the figure is that the actuator draws 0.66 A in 0.0005 seconds. It means that the current controller will be implemented for the BLDC actuator should operate at least 20 kHz for the ideal design purpose (Willsky and Young, 1997), which is 10 times higher than the current step response of the actuator 2 kHz (1/0.0005 seconds).

The actuator model given in this section is utilised in the simulations of proposed controllers in the following sections. Specifically, the controller parameters in the PID-BB controller are tunned based on the linear plant with the actuator model given in Figure 5.1. Conversely, the CTCL method requires a current controller for the controlling of torque input determined by (4.10). For this purpose, a conventional PI controller is

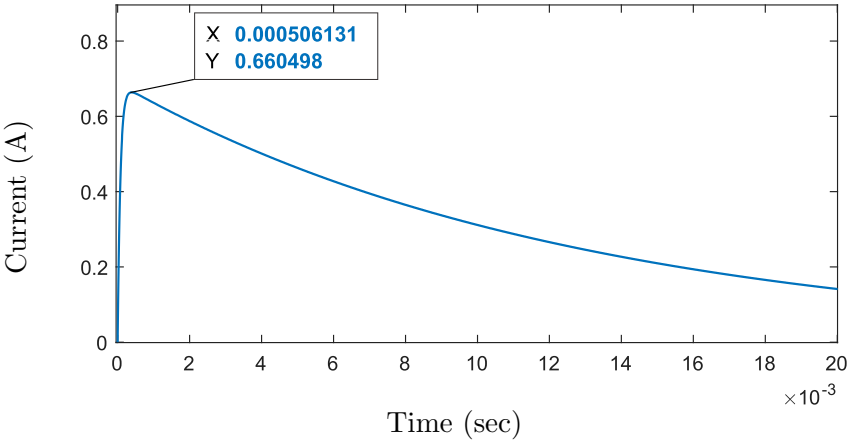

FIGURE 5.2: Step response of the current transfer function of the actuator

designed forming the innermost loop in the CTCL method operating at 20 kHz. Accordingly, the bandwidth of the controller decreases towards the outer loop, with the position and speed loop being at least one order of magnitude smaller than that of the current loop. For a satisfactory dynamic response without oscillations, the current controller designed should have the phase margin greater than 45° and the bandwidth should be designed in accordance with the performance criterias. In this manner, the bandwidth of the controller is evaluated from the bode diagram of the closed-loop transfer function of the system where the gain drops to -3 dB.

In Figure 5.3, the currents drawn in Phase A, B and C are plotted when 0.05 Nm torque step input is provided. Additionally, the trapezoidal back EMF arised in the actuator during the operation is given in Figure C.3.

5.3 Simulation of the FJ-TVC System without Uncertainties

This section gives the simulation result performed for the FJ-TVC system where it is assumed that the system dynamics are known precisely. Within the theoretical background of the developed controllers, this section gives the controller parameters and designs the Simulink models, then simulates the PID-BB and PD-CTCL controller, respectively. The controller using robust $\mathcal{H}_\infty$-CTCL method is not implemented in this section as it comes into prominence when the system uncertainties and disturbances are considered in the controller design, which is the subject of the next section. Additionally, the performance targets of the FJ-TVC concern position command tracking. Therefore, the step response of the system is simulated for each controller where the reference input

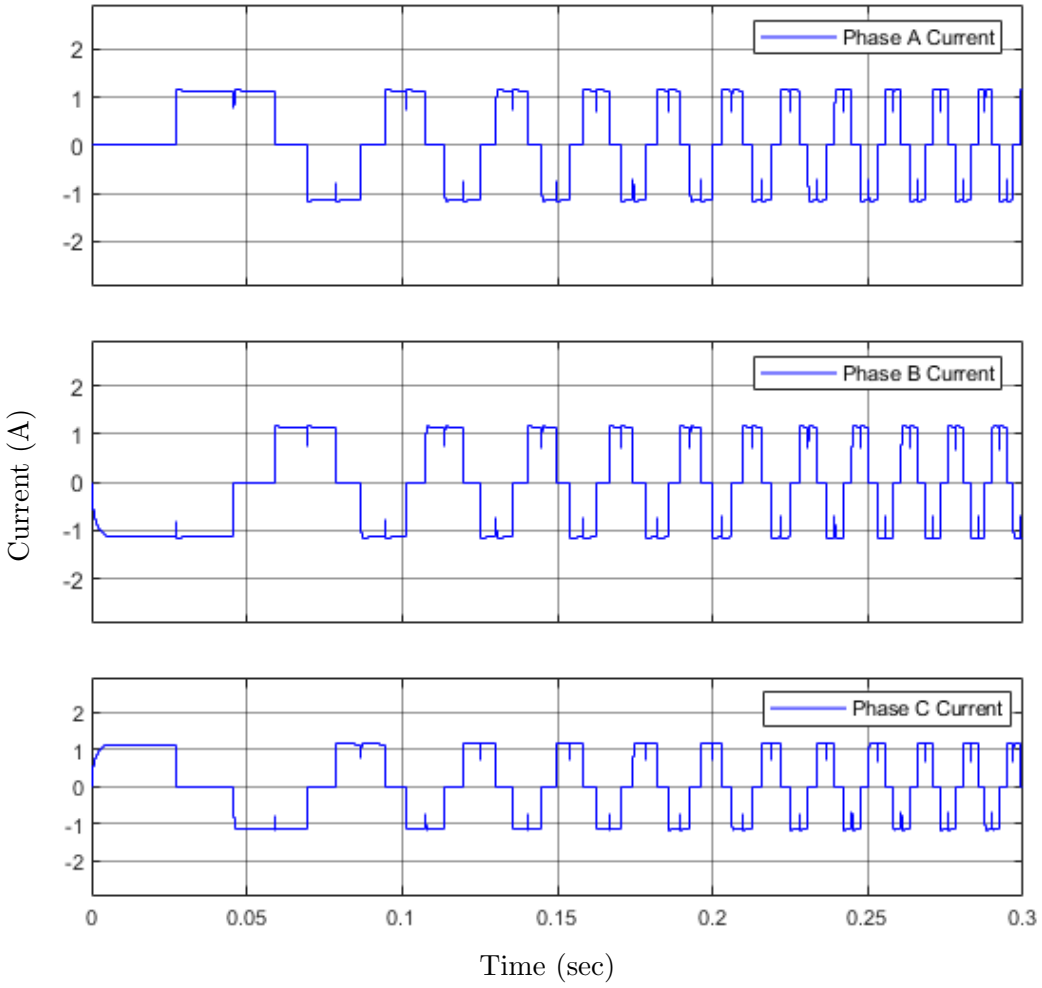

FIGURE 5.3: Phase Currents I_a, I_b, I_c when 0.05 Nm torque step input is fed into the current loop.

is defined as 0.8° for the rotation of nozzle in yaw and pitch axes. The physical and geometrical properties of the FJ-TVC model are given in Table B.1 (Appendix B).

5.3.1 PID-BB Controller

The PID-BB controller is simulated in this section. In this controller, the Bang-Bang controller is used to improve the rapidity of the dynamic response of the system and also provides the maximum allowable input when it is 'on' position. Figure 5.4 illustrates the Simulink model of PID-BB controller for the control of the FJ-TVC system.

The 'on-off' switching value of the bang-bang controller is set 0.5° in the simulation studies. The switching value can be set to a smaller/larger value, however, it affects the controller performance, e.g., there will be an oscillating error around the switching value if it is setted to a smaller value such as 0.05°. Conversely, a larger switching value makes the bang-bang controller redundant. Consequently, 0.5° is decided as an average value

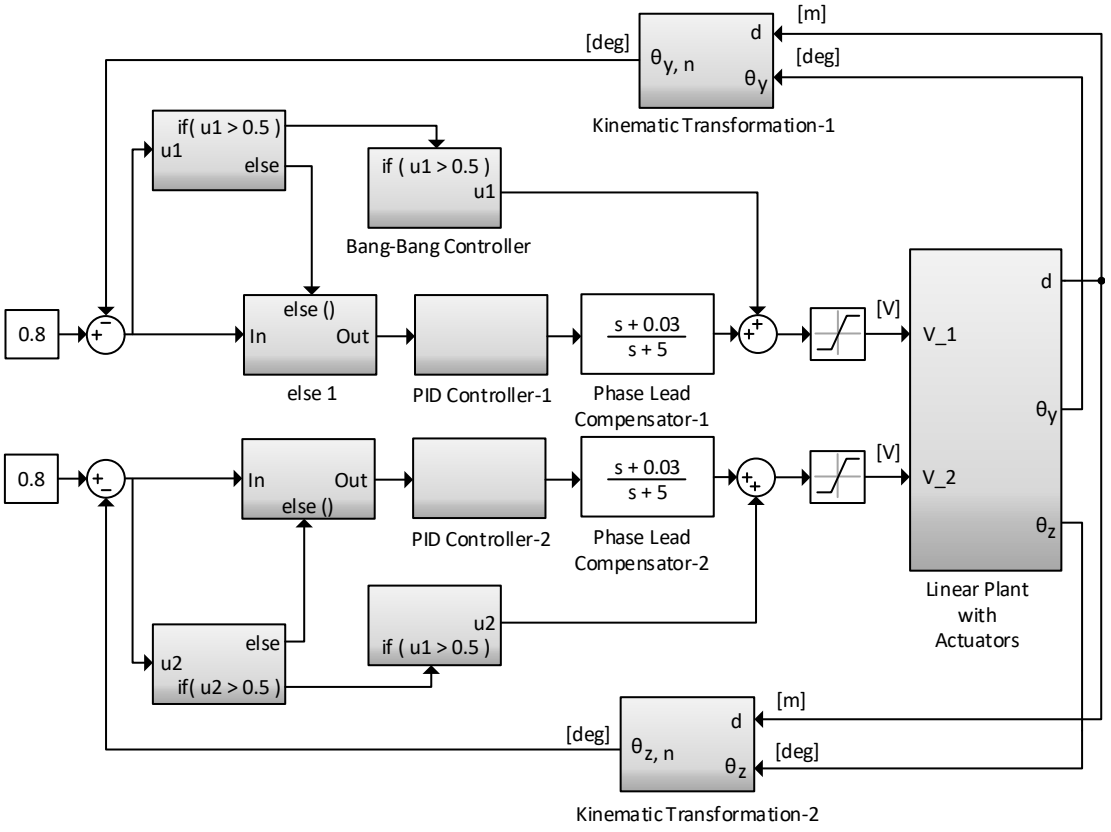

FIGURE 5.4: Simulink model of the PID-BB controller.

without causing any oscillation. The parameter tuning process for the PID controller with phase-lead compensator is given by Li et al. (2011) and Lu et al. (2010). The dynamic model used in the simulation is the linearised model given in A.1 (Appendix A). The parameters evaluated for the simulation studies as follows: the proportion coefficient is 122, the integral coefficient is 0.397 and the differential coefficient is 4.37 where the units are [V/rad]. The transfer function for PID and phase lead compensator are:

$$G_{PID}(s) = 122 + \frac{0.4}{s} + 4.37s$$
$$G_{lead}(s) = \frac{0.03s + 1}{0.003s + 1} \tag{5.1}$$

To investigate the bandwidth of the FJ-TVC system, a chirp signal is fed to the closed-loop system as an input and the output signal of the system is plotted with the reference input. Therefore, the bandwidth of the corresponding axis is evaluated where the output signal decreases to 0.707 of the magnitude of input which corresponds to -3 dB in bode diagram. For this purpose, the trajectory tracking of the FJ-TVC system when the chirp signal is given in Figure 5.5. The initial frequency of the input signal is 1 Hz and the final frequency at 20 seconds is 20 Hz. As can be seen from the figure, 5 Hz bandwidth

requirement is satisfied for 0.8 degrees of sinus input, where the evaluated bandwidth is around 15.5 Hz. It worths to remind that the current limit is 5 A and the saturation limit is 24 V.

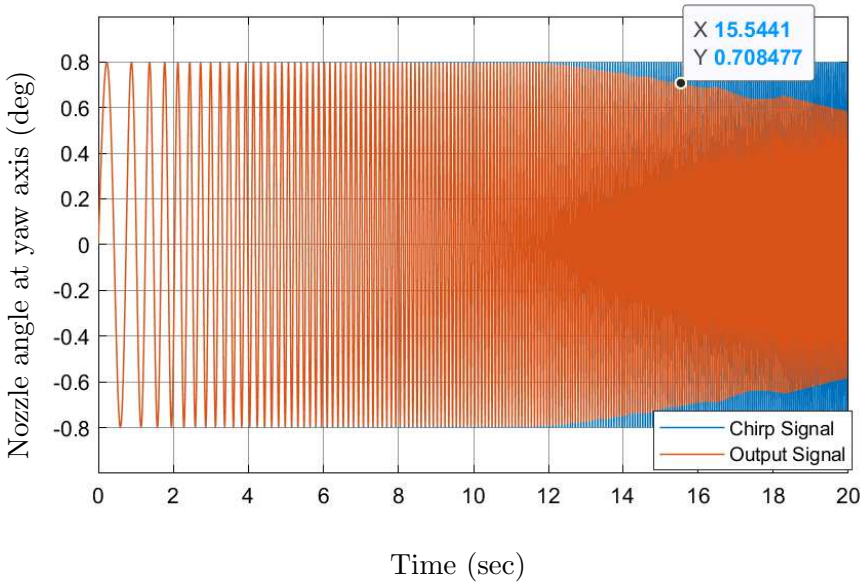

FIGURE 5.5: Trajectory tracking of the FJ-TVC system when the chirp signal is supplied as an input.

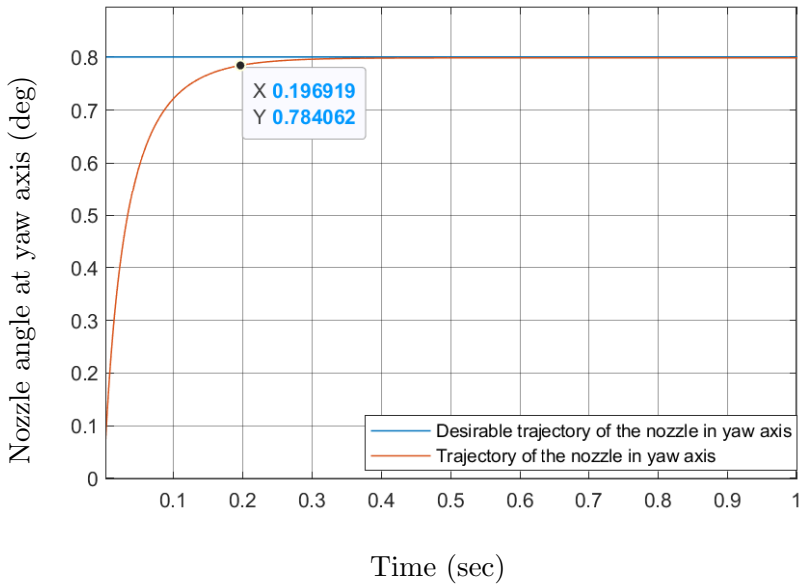

FIGURE 5.6: Yaw axis trajectory tracking control of the nozzle with the PID-BB controller.

As a further analysis, the settling time, steady-state error and overshoot of the system responses can be examined. Figures 5.6 and 5.7 give the output of yaw and pitch axes trajectories of the nozzle from simulation of the controlled system. Closer inspection of

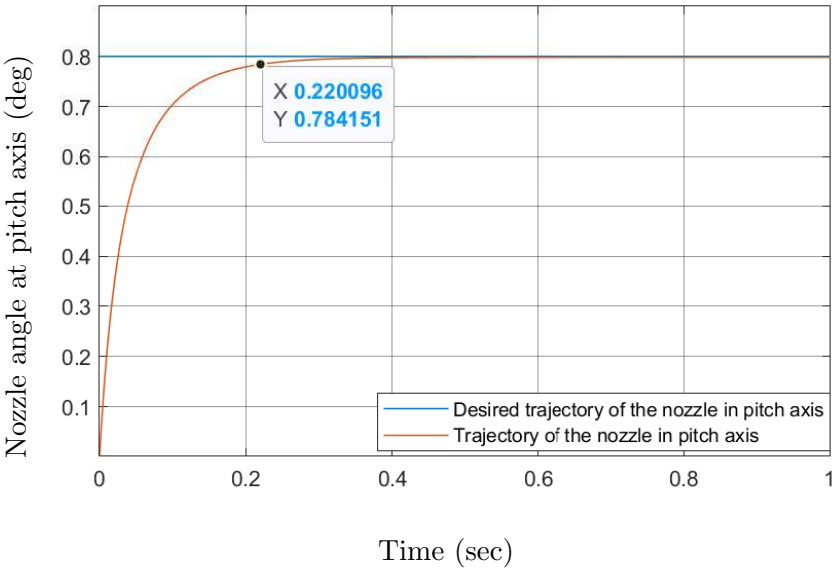

FIGURE 5.7: Pitch axis trajectory tracking control of the nozzle with the PID-BB controller.

the figures confirm that the joints are able to follow the desired trajectory. The error between the trajectory and reference input at the specified settling time is approximately 0.02° and the settling times are approximately 0.20 and 0.22 seconds, respectively, for the 2% error tolerance band.

Based on these simulations, it is concluded that the control performance satisfies the system requirements defined in Table 5.2 and also is in agreement with the performance results of (Li et al., 2011). Nevertheless, a sensitivity analysis should be performed to evaluate the switching error if there is more feasible switching point, which is not covered in this work since the system controller performances are met. Additionally, it was emphasised in the previous chapter that Phase-lead compensator improves phase margin and provides a quick response as it increases bandwidth. However, it was concluded that the bandwidth of the system is already higher than the requirement of 5 Hz for 0.8 degrees of nozzle rotation. Thus, it seems that the compensator design in adddition to the PID controller, as it was proposed by Li et al. (2011), might not affect the results positively as predicted and require further investigation in the future work.

5.3.2 PD-CTCL Controller

As an alternative approach, this section simulates the CTCL method where the PD controller is included in its outer loop. This method also guarantees tracking of the desired trajectory within the required torques are evaluated for an accurately well-known dynamic model as discussed in the previous chapter with its theoretical formulation.

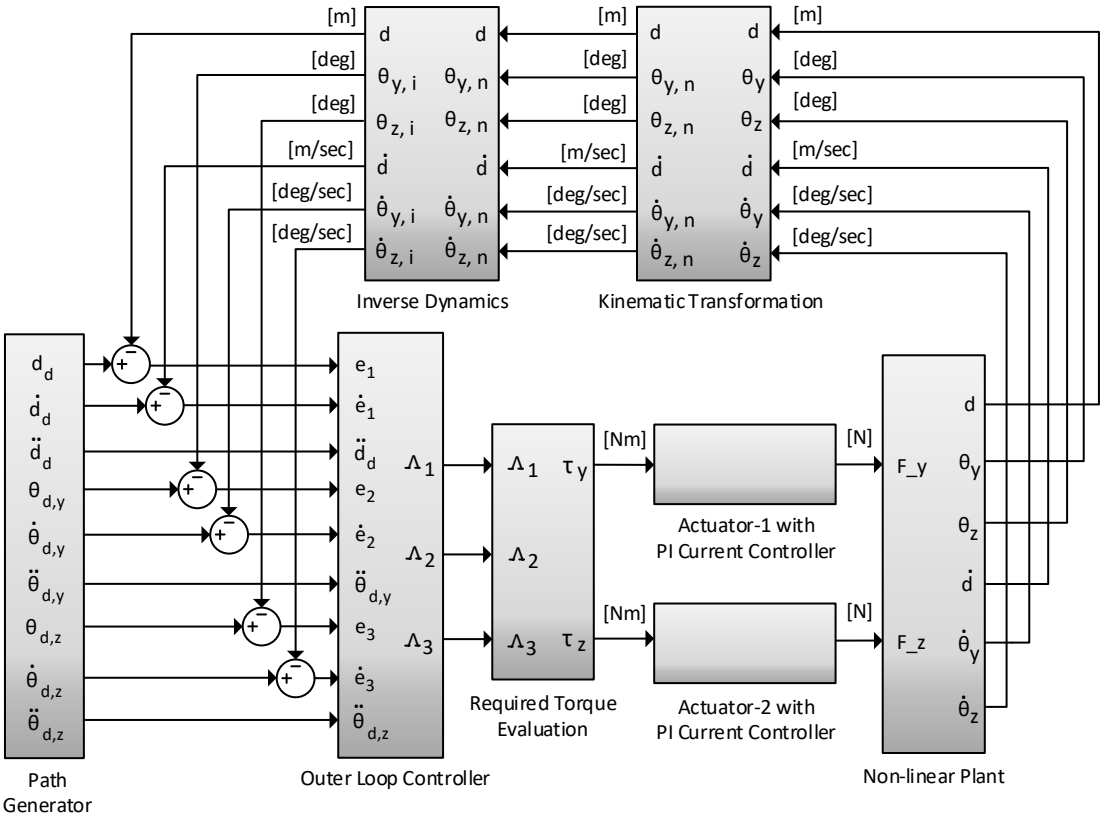

FIGURE 5.8: Simulink model of the PD-CTCL controller for accurately known FJ-TVC system

Figure 5.8 illustrates the Simulink model of the PD-CTCL controller. The inner loop evaluates the inverse dynamics of the system including the inverse of $M(q)$ inertia matrix, $N(q, \dot{q})$ Coriolis/centripetal matrix and $F(\dot{q})$ friction terms. In the simulink model, d, θ_y and θ_z are the variables obtained from the feedback sensors. For the controlling of the nozzle, these variables are converted into the variables representing the nozzle orientation in terms of yaw and pitch axis which are defined as $\theta_{y,n}$ and $\theta_{z,n}$, respectively. This conversion includes the number of ticks in the encoder, the pitch size of the ballscrew and the length of the moment arm used in the position kinematics of the system. Additionally, $\theta_{y,i}$ and $\theta_{z,i}$ are the outputs of the inverse dynamics equations. The outer loop stabilises the system by using a PD controller and enforces tracking of the prescribed trajectory. The reference input is defined as 0.8° for the rotation of the nozzle in yaw and pitch axes.

Figures 5.9 and 5.10 gives the output of yaw and pitch axis trajectories of the nozzle from simulation of the PD-CTCL controller. It confirms that the joints are able to achieve the desired reference input. The error between the trajectory and reference input at the specified settling time is around 0.01°, which was approximately 2% when PID-BB controller was used. The settling time is approximately 0.05 seconds for the 2% error tolerance band which is much superior to the conventional approach.

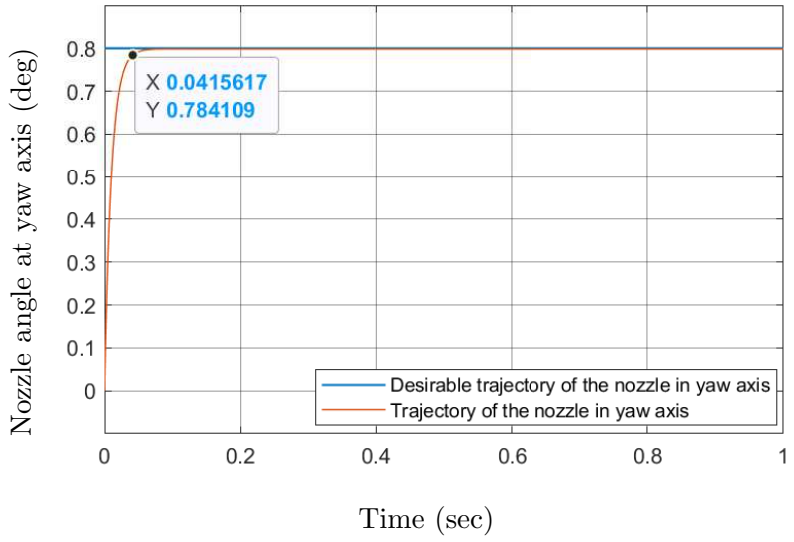

FIGURE 5.9: Yaw axis trajectory of the nozzle with the PD-CTCL controller.

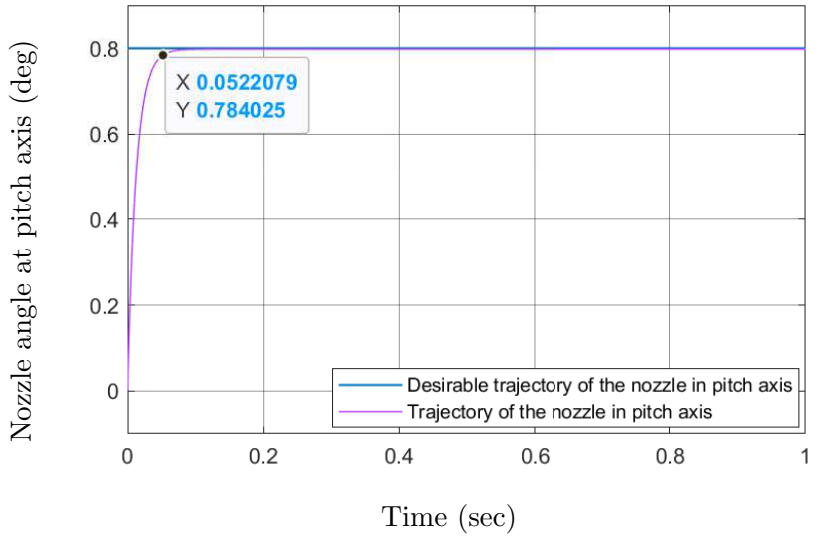

FIGURE 5.10: Pitch axis trajectory of the nozzle with the PD-CTCL controller.

In comparison, it can be concluded that the model based CTCL method calculates the required torques immediately and supplies it to the actuator. Therefore, although both controllers use classical control techniques such as a PD or a PID controller, the PD-CTCL design establishes a superiority over the previous study in regards to lower steady-state error and shorter settling time. However, it should be noted again that all the system parameters are assumed as known accurately.

The next section takes into account the uncertainties in the system model.

TABLE 5.4: System parameters and corresponding mean and deviation values.

Parameter	Definition	Unit	Mean Value	σ (%)
m_1	Mass of *link-1*	kg	0.3490	0.0201
m_2	Mass of *link-2*	kg	0.8306	0.0314
m_3	Mass of *link-3*	kg	2.0736	0.0502
J_{yy}	Inertia of *link-2*	kg.m^2	1.8231	0.0291
J_{zz}	Inertia of *link-3*	kg.m^2	14.8144	0.0476
d	Linear Displacement	m	0.0042	0.0498

5.4 Simulation of the FJ-TVC System with Uncertainties

This section simulates the developed controllers for the FJ-TVC system, where the uncertainties in the system model are taken into account as a different approach. Additionally, robust $\mathcal{H}_\infty$-CTCL method, which is a modern control technique to reject the disturbances and uncertainties, is implemented in addition to the controllers in the previous section. The simulations are demonstrated on tracking control of defined circular path instead of a step response.

Within this formulation, previously identified parameters are re-evaluated and obtained as in Table 5.4.

5.4.1 PID-BB System Performance

The PID-BB controller is simulated for the same plant but including uncertainties. The uncertain state space block is used in the Simulink environment to demonstrate the effect due to the uncertainties over system performance. Rotation angles for the joints are limited to $(-2.0°, 2.0°)$ for a circular path of desired trajectory. The parameters for the PID-BB controller are kept in the same form as in (5.1). Then, the worst case scenario from the simulation results is illustrated in Figure 5.11.

This simulation study demonstrates that the trajectory generated does not give acceptable performance. Figure 5.12 shows the joint errors in the corresponding axes. The dashed red line in the figure indicates the level of limit as an angular error. It is concluded that the joints exceed the limit of angular error at certain times. The maximum angular error is approximately 0.36° which is higher than 0.2° allowable angular error.

5.4.2 PD-CTCL System Performance

This section considers a PD based CTCL controller in the presence of uncertainties. The controlled system is stable by choosing k_p and k_d as positive diagonal matrices. It is

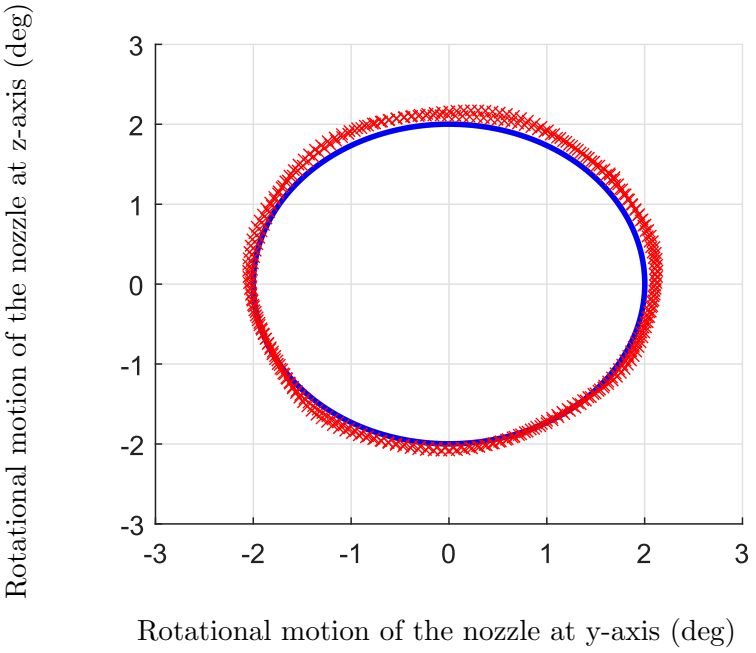

FIGURE 5.11: Trajectory tracking control with the PID-BB controller.

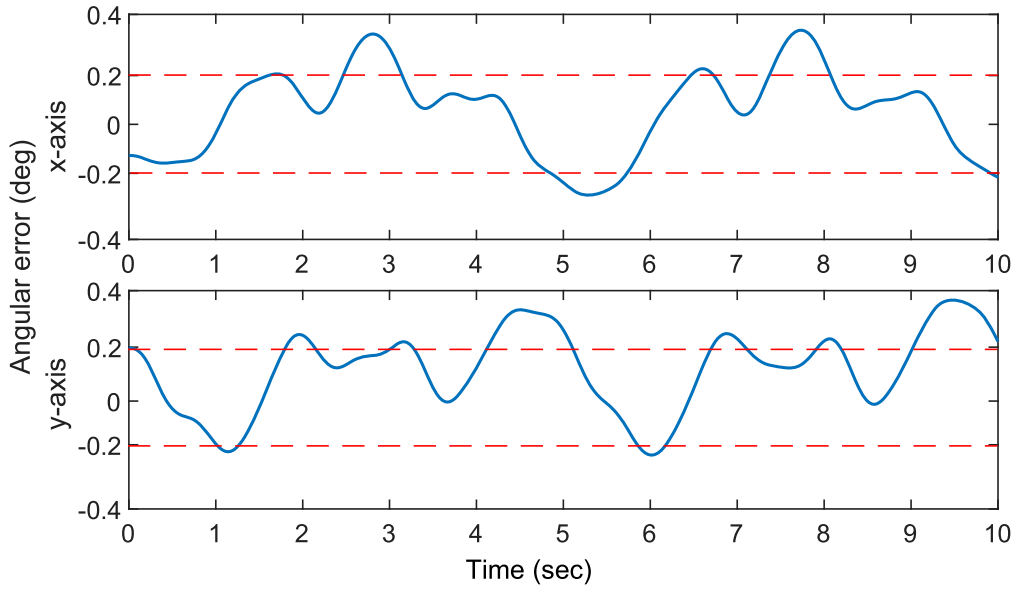

FIGURE 5.12: Trajectory tracking error generated by the PID-BB controller.

common to select these gain matrices as diagonal and hence stability holds provided all diagonal entries are positive. In this section k_p and k_d are, respectively, $500I$ and $100I$, where I denotes the identity matrix. Figure 5.14 gives a representative of the simulation results for this choice, where the desired trajectory is a circle and the rotation angles for the joints are limited to $(-2°, 2°)$.

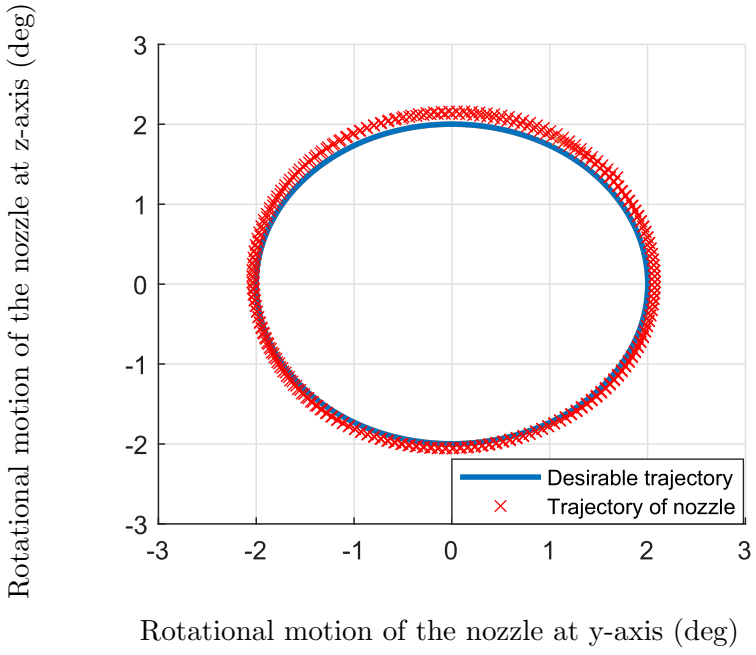

FIGURE 5.13: Trajectory tracking control with the PD-CTCL controller.

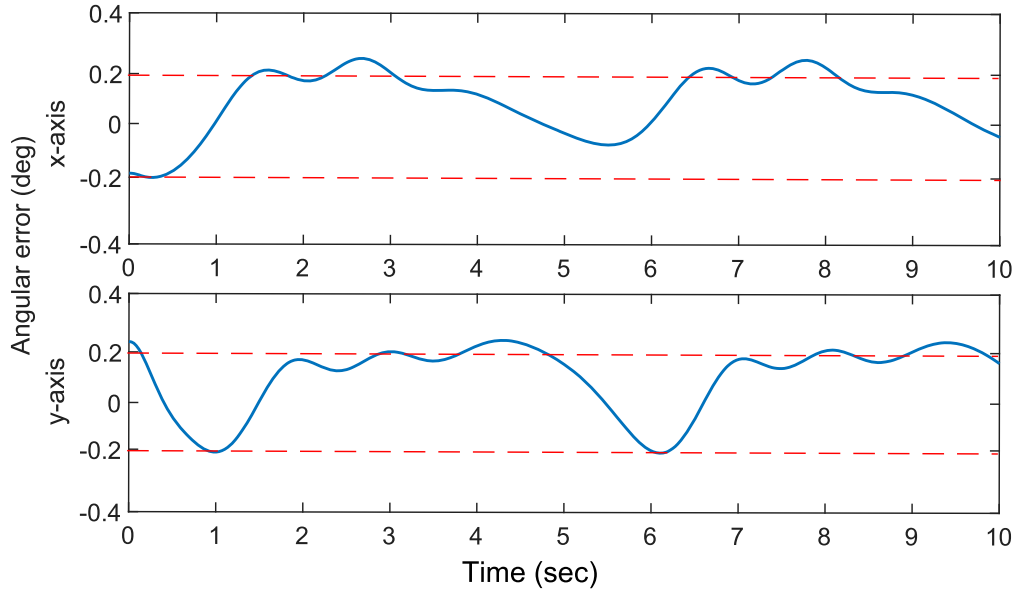

FIGURE 5.14: Trajectory tracking error generated by the PD-CTCL controller.

This simulation demonstrates that the trajectory tracking is not in the acceptable range where Figure 5.13 shows the desired trajectory and the nozzle angular output and Figure 5.14 illustrates the joint errors. The maximum joint error is evaluated as approximately 0.28° which is slightly over allowable angular error (0.2°).

5.4.3 $\mathcal{H}_\infty$ - CTCL System Performance

The controller models designed for uncertain systems always demand more attention to surpass uncertainties and disturbances. After the results achieved in previous sections, it is concluded that the classical controllers are not very powerful to satisfy the requirements when the uncertainties are not fully covered. Therefore, $\mathcal{H}_\infty$ design, which is one of the well-known modern control methods for the plants including uncertainties and disturbances, is simulated in this section. Previously, its theoretical background has been introduced in Section 4.3.2.2. Within this method, when the sufficient conditions are satisfied, it is expected the $\mathcal{H}_\infty$ control law stabilises the system, even with the variations of system parameters.

The objectives of the weight functions to be applied for the $\mathcal{H}_\infty$ were defined in Section 4.3.2.2. This section simulates the trajectory tracking of the nozzle by using the feedback gain obtained from the evaluation of the $\mathcal{H}_\infty$ optimisation problem. The YALMIP software (Löfberg, 2012) is used to solve the problem. Figures 5.15 and 5.16 show the trajectory tracking of the nozzle and angular errors of the joints respectively.

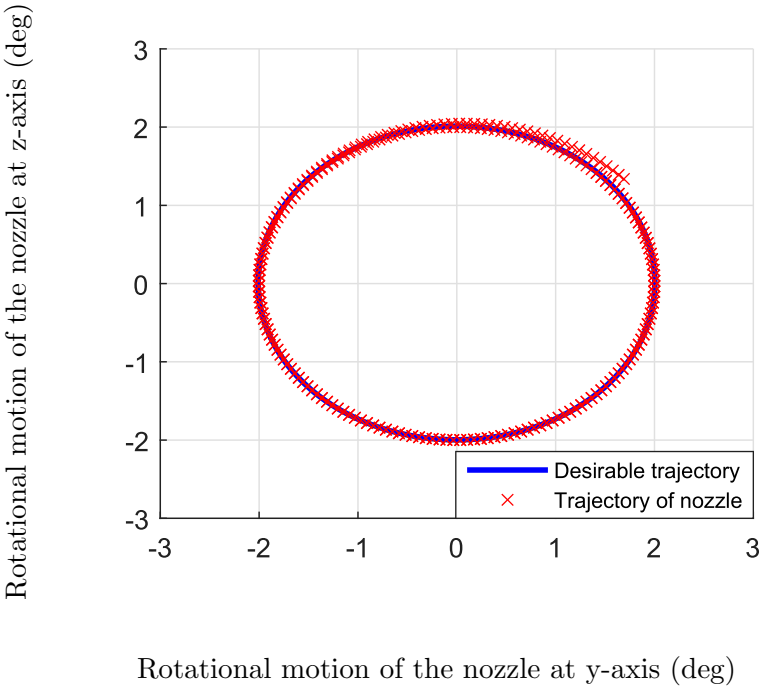

FIGURE 5.15: Trajectory tracking control with the robust $\mathcal{H}_\infty$ controller.

Consequently, the rotational errors are decreased to a lower level because of the robustness of the controller to the structured uncertainties and unmodelled dynamics. The joint space rotational errors for the x- and y-axes are less than 0.05° (the small amplitude oscillations are not critical). Therefore, this chapter establishes that $\mathcal{H}_\infty$-CTCL

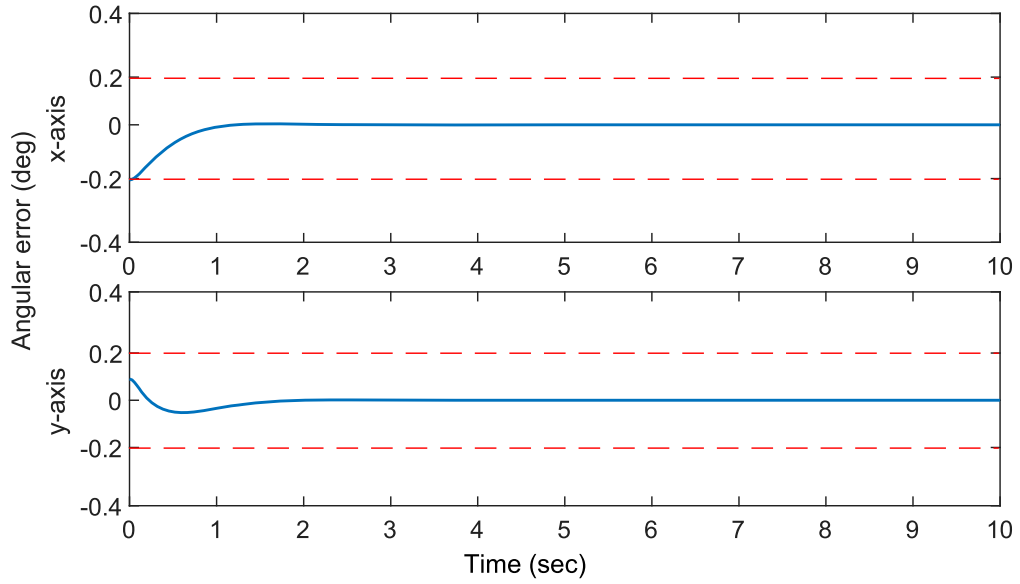

FIGURE 5.16: Trajectory tracking error generated by the robust $\mathcal{H}_\infty$ controller.

achieves excellent trajectory tracking control in spite of unmodelled dynamics and uncertainties where the conventional controllers such as the PID-BB and PD-CTCL methods are not very effective.

In conclusion, the performances of the three-controllers can be distinguished from each other by comparing their maximum trajectory tracking error occured in the simulation time. It should remind that the CTCL method evaluates inverse dynamic equations and hence provides better tracking control based on the accurately known dynamic model where the non-linear plant model can be implemented. Conversely, the PID-BB controller utilises the linear model derived for the FJ-TVC test-rig which might cause inadequacy in controller performance. This is the dominant feature between the controllers. In addition, when the uncertainties on the system parameters are taken into account, it is concluded that the PID-BB and PD-CTCL controllers could not minimise the disturbance effects due to the uncertainties, which were, however, attenuated by the $\mathcal{H}_\infty$-CTCL design. Numerically, while the maximum angular errors of the PID-BB and PD-CTCL controllers are evaluated as approximately 0.36° and 0.28°, respectively, the $\mathcal{H}_\infty$-CTCL design has less than 0.05° tracking error.

5.5 Summary

In this chapter, the system requirements and specifications for the FJ-TVC system have been defined. This is followed by a simulation based study of the controllers designed in the previous chapter. Each controller is evaluated for two different system models,

where the initial model assumes the dynamics of the FJ-TVC is known precisely, whereas the second one defines the uncertainties in addition to its nominal model. Within this framework, the performance results of each controller are discussed in detail.

For the initial case where the uncertainties are not introduced for the system model, the simulation results of the conventional controllers enable the joints to follow the desired trajectory very well. The errors between the trajectory and reference input are less than 0.02% and the settling time is approximately 0.05 seconds for the 2% error tolerance band. However, for the second case where the uncertainties are considered by using Monte Carlo based evaluations, it is concluded that the performance output of the conventional methods are not sufficiently robust and stability problems could arise in the current control loop due to the unstructured uncertainties. To counter such effects, an $\mathcal{H}_\infty$ based computed torque controller was designed based on norm bounded model uncertainty. Then, the effectiveness of the final design is demonstrated by a simulation study and it is established that an $\mathcal{H}_\infty$-CTCL achieves excellent trajectory tracking where the uncertainties are minimised and joint errors are decreased to a lower level.

Some results from this chapter form the basis of (Aydogan et al., 2019).

The next chapter details the experimental setup environment and then it is followed by the experimental validation of simulation results obtained in this chapter.

Chapter 6

Real-Time Experimental System

In the previous chapter, the results of a simulation based studies for the FJ-TVC system were reported. However, the performance of algorithms on an experimental setup is also crucial for the verification of results. This chapter details the design and commissioning the experimental setup where the developed control algorithms will be tested. To achieve this, firstly a test-rig for the FJ-TVC system is designed by using a Computer Aided Design (CAD) software. The purpose of the test rig is to provide a system that has the key features of the flexible joint structure in the FJ-TVC system. When the effects due to the pivot point displacement of the nozzle are considered, it was concluded from the studies in the literature that the flexible joint has larger displacement in the axial x-axis than the displacements in radial directions perpendicular to the x-axis (Lampani et al., 2012; Swain et al., 2019; Chunguang et al., 2020). Within this context, the modelling of the test-rig with the new approach having one more degree of freedom compared to the conventional models of the FJ-TVC system is considered as a necessary step for the benchmarking of the controller performance over the nozzle orientation. Secondly, its manufacturing methods must be determined where the 3D printer or CNC technology are amongst these options. Once the same is manufactured, the hardware implementation of the dSPACE DS1103 Digital-Signal-Processing (DSP) controller is described. In addition to its compatibility with MATLAB® Simulink, its distinguishing features such as providing very efficient and accurate real-time solutions are noted. The following eight-steps procedures summarise the development process of the FJ-TVC experimental setup:

- Mechanical design of the FJ-TVC test-rig;
- Selection of the actuator and sensor components;
- dSPACE HWIL system setup;
- Identification of I/O interface between dSPACE and other electronics;

- Implementation of control algorithms;
- Compiling and embedding of the MATLAB/Simulink model into dSPACE electronics card;
- Constructing a real-time interface in Controldesk software;
- Calibration of the sensors;

This chapter firstly describes the custom designed test-rig for the FJ-TVC system, followed by the specification of actuator and feedback sensors. Additionally, the hardware-in-the-loop system setup and the real-time interface in Controldesk software are described. Lastly, the calibration procedures for the feedback sensors are defined and evaluated parameters are given within the Simulink model.

6.1 Design of the FJ-TVC Test Rig

This section introduces the design criterias of the FJ-TVC FJ-TVCtest-rig. By nature of the in-service FJ-TVC system, it provides the rotation of the nozzle in yaw and pitch axes to achieve the trajectory tracking of the vehicle, where the flexible joint structure is the significant component taking an active role. However, the displacement of the pivot point due to the elastomeric structure of the flexible joint causes misalignment issues on the nozzle angle, which needs to be modelled in its dynamic model and the same has to be implemented in the test-rig design. The design of the test platform, therefore, has been studied within a new approach to develop the dynamic model of the FJ-TVC system more accurately as discussed in the derivation of mathematical model in Chapter 3 and implement the simulated controller designs in Chapter 5.

The design criterias of the test-rig are defined as follows:

- The test-rig must have 3-DoF which are the rotational motion of the nozzle about the y- and z-axes, and the translational motion in the x-axis;
- The rotational motion of the nozzle must be at least ± 5 degrees and the spindle length of the actuator, therefore, has to be longer than the length required for the rotational motion of the nozzle;
- The nozzle must have 5 mm of translational motion capability in the x-axis and there should be mechanical stoppers at both ends;
- The nozzle should achieve 5 deg/sec angular velocity capacity in rotational motion;
- The test-rig has to include linear springs as a counter load to perform the rotational motion of the flexible-joint mechanism;

- The test-rig has to include linear springs as a counter load to perform the translational motion of the flexible-joint mechanism in the x-axis;
- The mechanical parts in the test-rig must be strong enough to handle loads applied by the actuators and linear springs;
- The test-rig should be manufactured within a tight tolerance to avoid issues due to the mechanical gaps;

In the test-rig design, instead of using a combination of molded rubber and metal sheets in a flexible joint structure, four-symmetrically aligned linear compression springs are utilised to provide the counter load of the flexible joint. Preload is applied to the compression springs to avoid the play existing in the gap between the springs and mechanical parts. The compression force in the mechanical spring, corresponding to the spring torque over the nozzle, increases as the rotation angle of the nozzle increases. For the orientation of nozzle with 3-DoF including the pivot point displacement of the nozzle in the x-axis and the rotational motion about the y- and z-axes, a frame-in-frame gimbal assembly is designed to provide the rotational motion, which is then integrated into a sliding mechanism to move in the vertical direction with the nozzle. As a result, the physical structure of flexible joint is obtained by the design of a sliding mechanism with the frame-in-frame gimbal assembly. The orientation of the nozzle is supplied by the actuators where the counter-load is the resultant compression force of the four-symmetrically aligned springs.

Another advantage of the design is the ability to measure the rotational angle of nozzle in yaw and pitch axes by using two potentiometers integrated to gimbal shafts, in addition to the encoders on the actuator shafts. Therefore, the potentiometers form a back-up system to check the overall position and nozzle orientation independently as the encoder data on the actuator shaft is coupled with the linear displacement of pivot point.

Each mechanical component in the model is manufactured by either an industrial 3D printer or CNC machine depending on the load that it is exposed to. Acrylonitrile Butadiene Styrene (ABS) material is used for the parts that are printed in 3D printer due to known high resilience and impact resistancy. Some components such as gimbal frames are manufactured in aluminum to carry heavy loads and provide more precise orientation.

The FJ-TVC test-rig includes two actuators for the steering of nozzle in yaw and pitch axes where each actuator includes its own encoder and motion controller for the trajectory tracking control.

Based on the approach described above, the scaled version of the FJ-TVC system is designed by using a CAD tool, Solidworks software (Biovia, 2018), as shown in Figure 6.1.

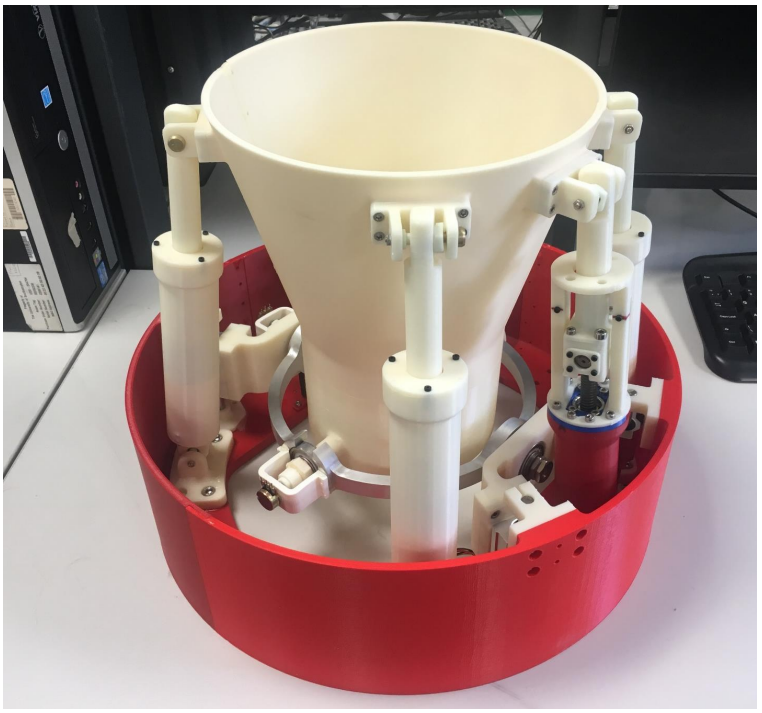

FIGURE 6.1: Prototype of the FJ-TVC system

Lastly, the equipment used in the prototype is listed as follows:

- Two brushless DC actuators
- Two motion controllers for brushless DC actuators
- Four linear springs to simulate the counter loads of flexible joint in yaw and pitch axes
- Two linear springs to simulate the counter loads of flexible joint in vertical direction
- Two potentiometers for yaw and pitch axes
- A linear laser displacement sensor

The developed prototype model in this chapter is designed by considering the dynamic model of the FJ-TVC system.

6.2 Specification of the Actuator and Feedback Sensors

This section gives the specification of selected actuator and sensors utilised in the experimental setup. The actuator is selected according to the control requirements defined in Table 5.2. The chosen Brushless DC (BLDC) actuator has been identified to have more effective characteristics with high torque by current ratio, speed range and power density.

In addition to the specification of the actuator and feedback sensors, the importance of their usage in the orientation of the nozzle is also discussed.

6.2.1 Brushless DC Actuator

The BLDC actuator is one type of permanent magnet synchronous motor that has a number of advantages when compared to direct current (DC) and induction motors. These include a better torque and speed ratio, high efficiency and reliability, fast dynamic response, low maintenance costs and no friction in the commutator. The disadvantage of the BLDC actuator is its complexity. For instance, electronic commutation requires executive circuits to ensure accurate timing of coil energisation for high precise speed and torque control, as well as ensuring the motor runs at maximum efficiency. This section gives the specifications of BLDC motor used in the experimental setup and the frequency responses of the each control loop designed in the cascade controller for the determination of the operating frequencies.

A Faulhaber BLDC actuator with an integrated magnetic encoder and a ball screw mechanism is selected for the experimental setup as shown in Figure 6.2.

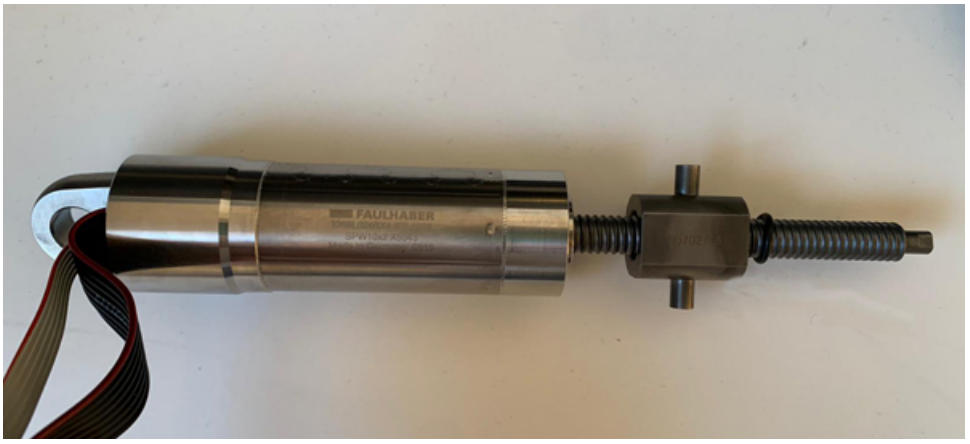

FIGURE 6.2: Brushless DC actuator - Faulhaber 3268-L024-BX4

The reason for selecting this actuator is due to its fast dynamic response, its significant operating temperature range between $-40°$ to $+65°$ and its easy compatibility with the requirements of MIL-STD standards. Unlike Faulhaber's shelf products, this actuator includes a magnetic encoder which has 1024 lines per revolution and a ball screw with 10mm diameter and 2 mm pitch size.

The full list of the motor parameters is given in Table 6.1 which also includes several important parameters such as no load speed, no load current, stall torque and terminal resistance. These parameters are used in the evaluation of actuator power which is one of the key parameters in determining of the actuator performance.

TABLE 6.1: Technical specifications of the actuator

Parameter	Value	Unit
Nominal Voltage	24	V
Number of Pole	4	-
No Load Speed	5500	min^{-1}
No Load Current	0.183	A
Stall Torque	705	mN.m
Friction Torque	11.10^{-4}	$mN.m/min^{-1}$
Speed Constant	220	min^{-1}/V
Back-EMF Constant	4.534	mV/min^{-1}
Torque Constant	43.5	mN.m/A
Current Constant	0.023	A/mN.m
Terminal Inductance	110^{-6}	H
Terminal resistance	1.47	Ohm
Rotor Inertia	63	$g.cm^2$

The next section gives more detail about the driver card specifications for the BLDC actuator.

6.2.2 Brushless DC Actuator Driver

The custom-design electronic driver card is used to drive the actuator. It also provides an interface for tuning of controller parameters utilised in the controller schemes, where position, velocity and current controllers can be implemented in a cascade structure, alternatively velocity and current controllers or only the current controller can be activated based on the controller design. It is built with six-Metal Oxide Semiconductor Field Effect Transistor (MOSFET), a gate switching unit, signal conditioning units and a diode rectifier with protection circuits. In Figure 6.3, the view of BLDC actuator driver card set is shown. As seen from the side view, it has three electronic cards which are the processor card, the driver card and the MOSFET card.

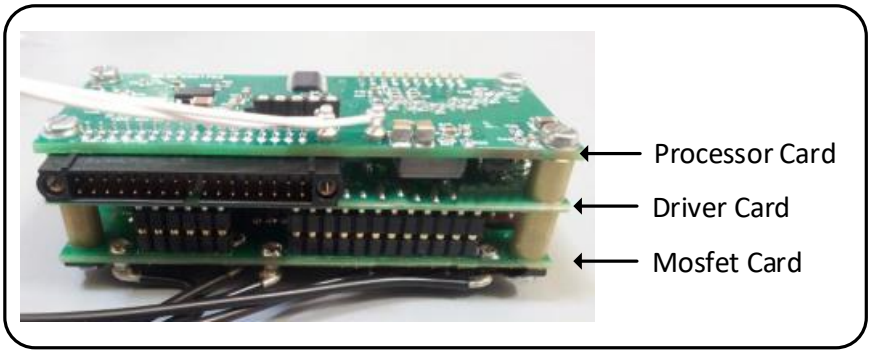

FIGURE 6.3: Brushless DC actuator driver, side view

The processor card generates space vector PWM signals, triggers the switching gates and reads the hall sensor data on the actuator in addition to the signals from external feedback sensors such as the potentiometer, encoder and the current sensor. In Figure 6.4, the bottom view of the driver is shown. The phases of the actuator are connected into the interface in this card.

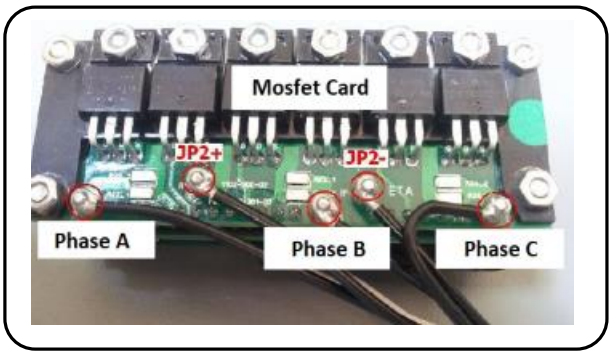

FIGURE 6.4: Brushless DC actuator driver, bottom view

The reading of hall sensor on the actuator is accomplished by the pull-up resistance as shown in Figure 6.5. This unit can read the digital signals up to 10k rpm rotation speed.

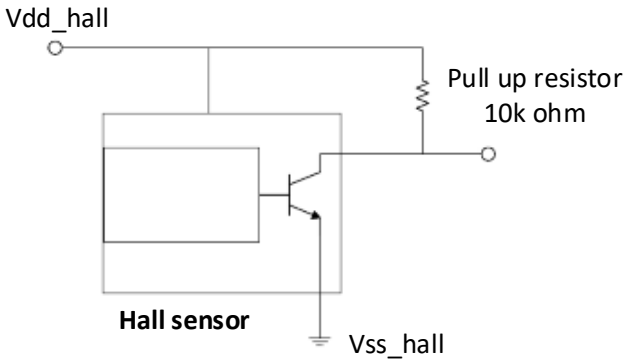

FIGURE 6.5: Reading of hall sensor by pull-up resistor

The processor on the processor card is the dsPIC33EP model which is suitable for precision motor control. The features of digital signal controller (DSC) are as follows;

- 7.14 ns PWM resolution
- 70 MHz max CPU Speed
- 512 KB program Memory Size
- 32-bit Quadrature Encoder Interface (QEI) module configurable as a timer/counter

- Peripheral Trigger Generator (PTG) for scheduling complex sequences
- ADC module, configurable as 10-bit
- CAN™ module (1 Mbaud) CAN 2.0B support
- 4-channel DMA with user-selectable priority arbitration
- 5 x 16-bit, 2 x 32-bit timers

In the experimental setup, BLDC actuator driver is used for tasks such as 3-phase conversion, reading of hall sensor output and driving the actuator by generated PWM signals. The six-step inverter model including hall sensor commutation and gates blocks are given in Figure C.1. However, this is not the actual controller model existing in the driver card as it is developed and embedded by the third-party company and belongs to commercial restrictions. The driver card has its own GUI to set the controller parameters.

The driver utilised in the experimental setup plays a crucial role as an interface between the actuator and real-time hardware. However, the more important processing duties are assigned to the dSPACE hardware as its processing rate is much faster. Moreover, reading of some feedback sensor outputs are supported by the dSPACE hardware as well which ensure all the sensors data have been collected from the same interface.

6.2.3 Feedback Sensors

For the feedback control, three separate analog sensors have been used to measure the orientation of nozzle on rotational and linear axes. One of the feedback sensors is potentiometer, see Figure 6.6. This is assembled to the gimbal shaft for zeroing of the nozzle angle before the experimental tests where the encoder on the actuator shaft measures the rotational motion of the nozzle in the corresponding axis and the data is provided to the feedback control loop.

FIGURE 6.6: Rotary potentiometer (Sparkfun, 2021)

A rotary potentiometer has a linear characteristic model and its error tolerance is around 10%. As the purpose of this potantiometer is just to measure the overall rotational motion of the nozzle rather than providing accurate data into the feedback control loop, the error tolerance is not considered critical for the accuracy concerns. The model number of potentiometer is PDB182-K220K-104B. The working principle of this sensor is that the angular movement on the shaft causes the internal wiper to sweep around a curved resistive element, see Figure 6.7. Therefore, the output voltage gives a proportional response as the resistance value changes and gives the wipers angular position accurately. However, the calibration process is crucial to get reliable test data.

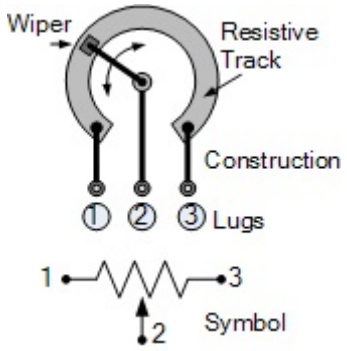

FIGURE 6.7: Curved resistor (etechnog.com, 2021)

A laser displacement measuring sensor is used to evaluate the linear position of the nozzle which corresponds to the displacement of pivot point in the flexible joint. In the experimental setup, therefore, a distance measuring device SHARP GP2Y0A is used, see Figure 6.8. Analog output voltage of this sensor is typically in the 0.4 to 2.3 V range and the position of object is identified according to the output voltage. Its position error tolerance is around 0.1 mm which is feasible for the orientation of nozzle as the vertical position of the nozzle changes between 1 to 4 mm.

FIGURE 6.8: Distance measuring device - Sharp GP2Y0A

Lastly, a current sensor is used to measure the supply of the system hardware and this signal is processed in the control loop to provide the required torque in order to ensure the nozzle position is in the right position according to the reference trajectory.

The selected current sensor, see Figure 6.9, produces an output that varies from 25% to 75% of the supply voltage as the magnetic field varies within the Gauss range. It is also possible that the increase on the number of turns within power cable passing through the current sensor increases the accuracy of the result. This version accepts a bidirectional current input with a magnitude up to 57 A and its response time is 3 µs which is

FIGURE 6.9: Current sensor - Honeywell CSLA1CD

very competitive. The accuracy of the sensor is improved by increasing the number of turns of the power cable through the sensor (three-times) and a multilayer ceramic capacitor (1 µF) is inserted in series with the output of the current sensor to block out the variations of the offset voltage. After these improvements and the implementation of the calibration procedures, the accuracy of the sensor is verified as approximately 2% by the current readings in the BLDC actuator driver.

All the datasheets corresponding to the feedback sensors used in the experimental setup are given in Appendix A.

6.3 Hardware-in-the-loop System Setup

This section firstly explains the specifications of the dSPACE HWIL system used for the experimental studies. The system provides software and hardware tools for implementing and testing real-time systems such as advanced control systems and HWIL simulations. The dSPACE electronic control unit is a set of electronic cards that processes the embedded code built by Simulink model. Then, Digital-to-Analog (DAC) and Analog-to-Digital Converters (ADC) are included in the dSPACE environment to supply the communication between the actuators and feedback sensors in the FJ-TVC prototype and control unit. The Controldesk software is used as a real-time interface to collect the data, plot the results and export them for further analysis in MATLAB.

The HWIL system runs based on the scheme in Figure 6.10. The experiments in this study starts with the controller design in MATLAB Simulink environment and continues with off-line performance tests. After the achievement of a good tracking performance from the controller, I/O of the model is identified and a wiring process is conducted between the electronic components in the prototype and the I/O connector card of the dSPACE system. Then, the next step is the building of the controller design and implementation of the code in the real-time controller card. Lastly, the Controldesk software enables to build very user friendly interfaces to control the parameters in real-time basis, collect the test data and present the results in a suitable graphics format.

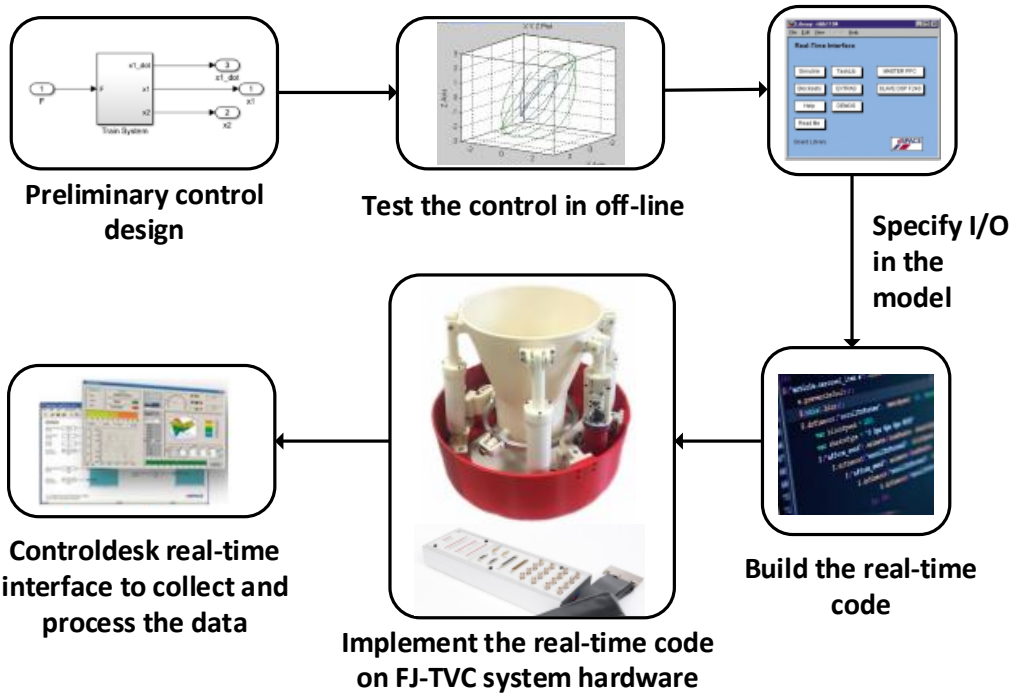

FIGURE 6.10: HWIL system

More specifically, a single arm on the FJ-TVC system is directly coupled with an actuator shaft and an incremental encoder, which is used to measure the linear displacement of the nut on the ballscrew. As seen from Figure 6.11, the Quadratic Encoder Pulse (QEP) signals Qa and Qb are connected to the I/O connector card which is linked to the quadrature pulse decoder in the control card to read the actual position.

Additionally, the subtraction of the actual position data from the reference position signal is applied to evaluate the position error and then it is fed to the position controller. Therefore, the output of the position controller becomes the input of the reference DC link current, Idc. Then, the calculated reference current in the computed torque control loop is compared with the measured Idc to evaluate the current error. Lastly, the output of the current controller provides the duty cycle of the gate pulse and the direction to be run. Therefore, according to the duty cycle output, the dSPACE generates PWM signals and passes these to a six MOSFET based inverter in BLDC actuator driver and making it run, as seen in the block diagram in Figure 6.11. All the feedback sensors such as the potentiometer, laser distance sensor and the current sensor are connected to the ADC channel of the dSPACE. After calibration of these sensors, the imported data are processed in the feedback control loop and it is becoming the part of the controller to generate the input signal. All these calculations are evaluated in the DS1103 DSP controller card and provided to the user with the interface of Controldesk software.

The measurement rates of the feedback sensors are critical for achieving of good control performance in the cascade controller. The operating frequencies of each control loop is

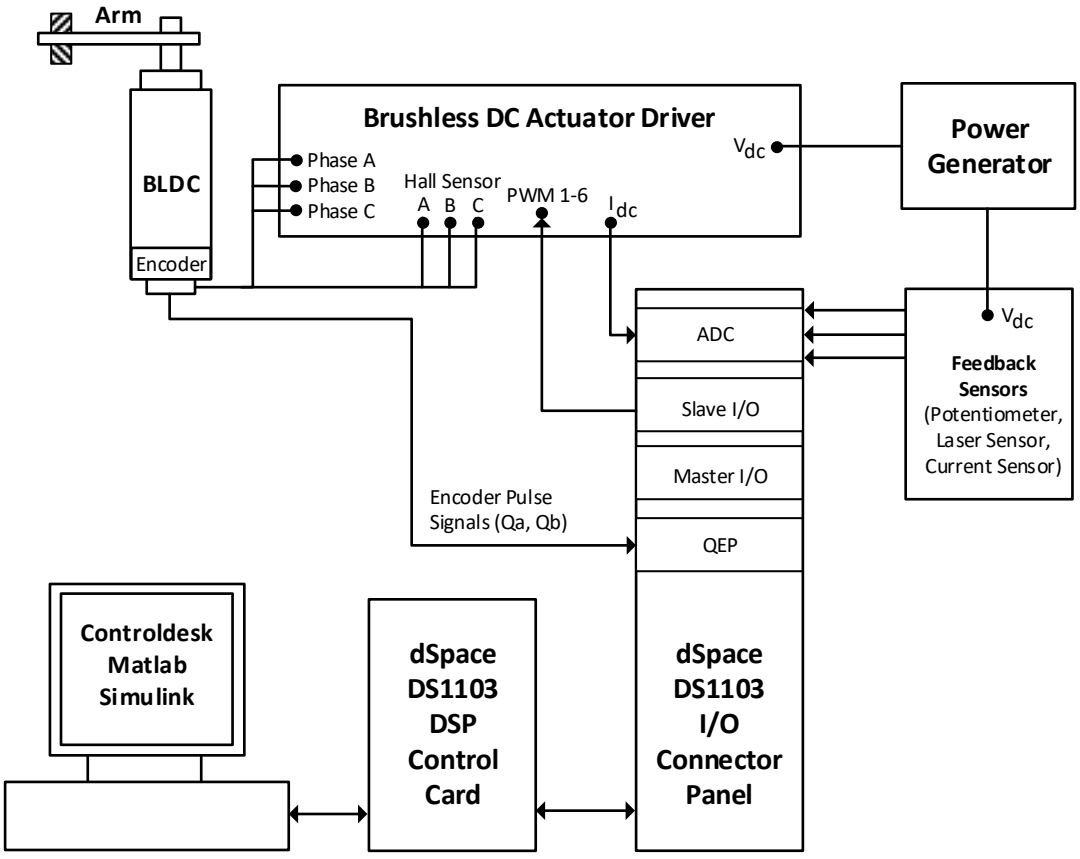

FIGURE 6.11: dSPACE hardware implementation block diagram

setted based on ideal design purposes where the innermost current control loop operates at 20 kHz and the feedback rate of the current sensor utilised for the feedback control is chosen in accordance with the operating frequency of the control loop (the response time of the current sensor is 3 µs). Additionally, the outer velocity and position loops are specified to operate in 2 kHz where the position data is measured by the encoder on the actuator and the velocity of the actuator is evaluated by taking the derivative of position data.

After the introduction of hardware implementation, the specifications of the dSPACE hardware is given in the following sections.

6.3.1 dSPACE Hardware

dSPACE allows to set up a control algorithm, gets the signals easily and quickly, and provides to turn new control methods into the real-time systems. Vast amount of Input/Output channels of different types make dSPACE a multifunctional system that can be used in especially mechatronic areas such as aerospace, robotics, automotive, medical engineering and renewable energy.

6.3.2 Electronic Control Unit

One of the subsystems of the system is Electronic Control Unit (ECU) including a multiprocessor.

Its specifications are as follows:

- PowerPC 750GX at 1GHz for rapid control prototyping
- Application memory 32MB
- Multiprocessor system up to 20 DS1103 processor boards with fibre optic connections
- 3 Timer interrupts
- Full programmable using MATLAB/Simulink

6.3.3 Multi-Channel Input/Output Board

A Multi-Channel Input/Output interface allows to receive and send the provided signals by the controller. The unit is shown in Figure 6.12. Its specifications are as follows:

- ADC with 16 multiplexed channels
- 16 Bit resolution on ADC
- DAC with 8 channels
- 16 Bit resolution on DAC

FIGURE 6.12: ADC and DAC channel board

6.4 Controldesk Software and Real-Time Interface

Real-time Interface (RTI) enables users to carry out and update design iterations. It also includes the C code generator called as Simulink Coder™ for the implementation of Simulink model on the real-time hardware. Therefore, without professional knowledge of developing C code programming, it is very straightforward with this experimental setup to build your own model in MATLAB Simulink and convert it to an appropriate C code for the electronic card.

In addition to the above noted functionality, it is very straightforward to connect the prototype to a dSPACE I/O electronic board by dragging the I/O module from the RTI block library onto the model and then connecting it to the Simulink blocks. Also, it allows the change of parameters over the blocks by clicking the settings option and after that, Simulink Coder™ builds the Simulink model and generates the suitable C code while preparing the model for the real-time application. This is a fast prototyping system that the real-time model is built, downloaded, and started on the real-time hardware automatically. Meanwhile, RTI ensures consistent checks for potential errors during the building process. Once identified then the same can be resolved swiftly.

The relationship between the MATLAB and the dSPACE enviroment is supplied by the Simulink blocks as seen in Figure 6.13. It is seen that RTI includes some blocks compatible with MATLAB Simulink, blocksets, functions of Master PPC board and Slave DSP F240 board.

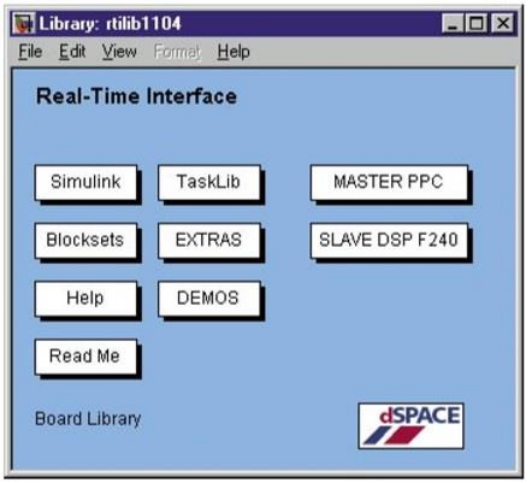

FIGURE 6.13: Real-Time interface of the dSPACE

Additionally, reading the analog signal by Analog Digital Converter (ADC) and sending the reference digital signal to the analog device by Digital Analog Converter (DAC) is an uncomplicated process using the library of the dSPACE in Simulink, see Figure 6.14.

The Controldesk software plays a vital role in fast prototyping which is used to embed the C files on its own interface after generated by Simulink Coder™ in MATLAB Simulink. In

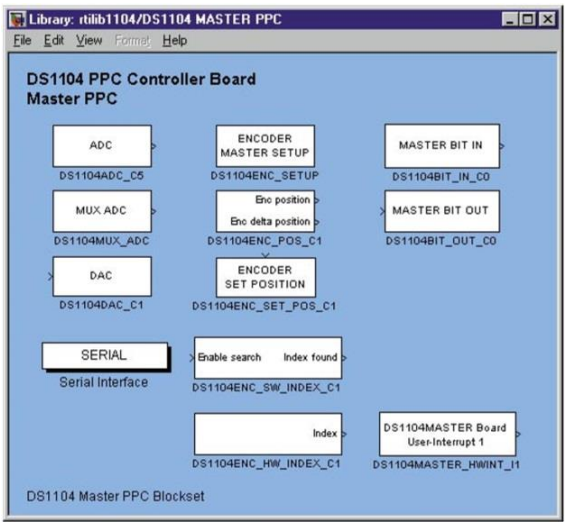

FIGURE 6.14: Simulink blocks for controller board

addition to its simple and userfriendly interface, it provides enormous range of features required for rapid prototyping.

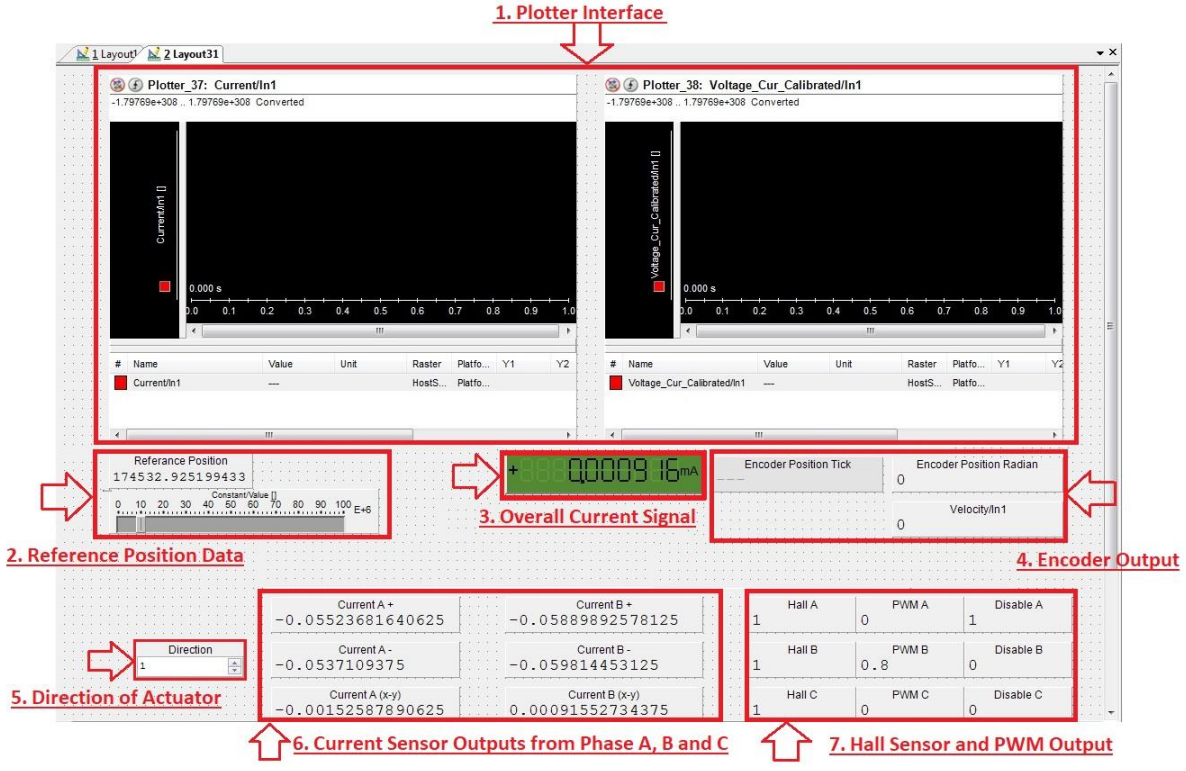

FIGURE 6.15: Controldesk software and interface

In Figure 6.15, the graphical user interface (GUI) of the FJ-TVC system includes the calibrated current signal, encoder data, reference position, hall sensor data and the PWM signal of the BLDC actuator. The Master PPC controller board also provides the encoder and position setting blocks in MATLAB Simulink library.

6.5 Calibration of the Feedback Sensors

This section gives the calibration procedures of the feedback sensors used in the experimental setup. It also gives the calibration models developed in MATLAB Simulink. The feedback sensors that need to be calibrated are the potentiometer, the current sensor and the laser displacement sensor which are detailed in the next sections, respectively.

6.5.1 Calibration of the Potentiometer

A common way to calibrate a potentiometer is to rotate the sensor between two different angular positions and read the change in the corresponding output voltage. In the calibration process, the supply voltage for the sensor is set to 5 VDC in accordance with the requirement. Also, the reference angular ruler with 0.1 degree accuracy is used stuck on the gimbal shaft, see Figure 6.16, to identify the angular position of the nozzle visually as a reference.

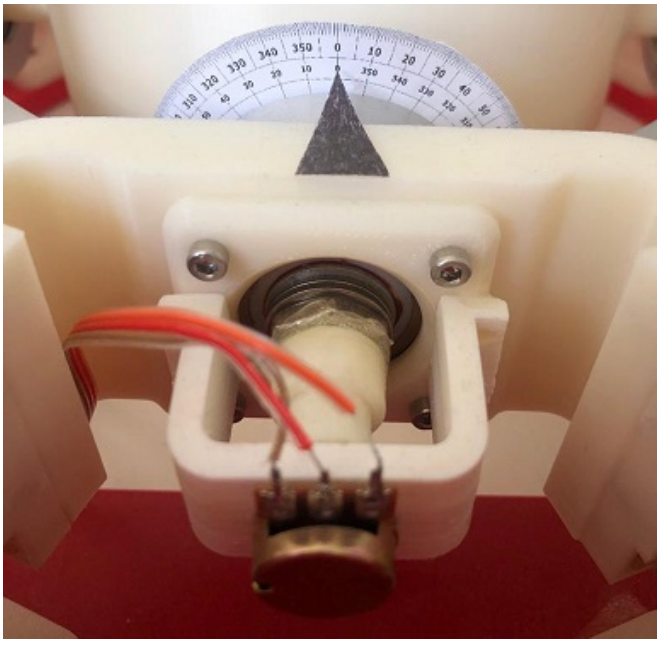

FIGURE 6.16: The calibration of potentiometer

The calibration procedures of the potentiometer are as follows:

1. Connect the I/O interface of the potentiometer (Pin 1 is Vdc, pin 2 is the analog output and pin 3 is ground)
2. Apply the supply voltage to the potentiometer (5 VDC).
3. Multiply the ADC signal by 10 which is necesseray for the compatibility of the resolution of the dSPACE.

4. Note the output voltage when the position of the shaft is setted to 0° which is termed as off-set value.
5. Subtract the off-set value from the analog output voltage.
6. Rotate the gimbal shaft to +5° degrees, and note the output voltage.
7. Rotate the gimbal shaft to −5° degrees, and note the output voltage.
8. Evaluate the difference between high and low analog voltage outputs.
9. Divide the value found in the previous step by 10 degrees to evaluate the corresponding voltage change for a degree which is termed as calibration factor.
10. Multiply the calibration factor with the value evaluated in the step 4 to evaluate the calibrated angular position.

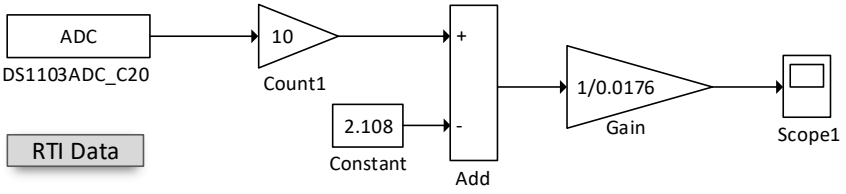

FIGURE 6.17: Calibration model of the potentiometer in MATLAB Simulink

After applying the procedures described above, the calibration model in MATLAB Simulink is developed as given in Figure 6.17. The output voltage of the potentiometer is set to 0 after subtraction of the value of 2.108. Then, it is multiplied by the calibration factor which is evaluated as $1/0.0176 = 56.8$ for this sensor. Hence, the angular position of the gimbal shaft is evaluated by using this calibration model.

6.5.2 Calibration of the Current Sensor

The current supplied in the experimental setup is measured by using a current sensor. However, the current sensor requires a calibration process to give more reliable and consistent outputs. To do this, firstly, a simple circuit including a resistor and power generator is built specifically for this calibration process. The current sensor generates an analog output according to the current passing from the magnetic core of the sensor. The output data of sensor is read by the dSPACE hardware. Additionally, the supplied current is limited by the current limiter in the power generator. Therefore, the output data from the current sensor is collected at different current levels. The change on collected data is used for the calibration of the current sensor.

The calibration procedure of the current sensor is:

1. Build a simple closed-loop circuit including a resistor and power generator.
2. Apply the supply voltage to the circuit (5 VDC).
3. Limit the current in power generator and take a measurement of current sensor analog output.
4. Subtract the off-set from the current sensor output to obtain zero bias.
5. Increase the current limit in power generator and take a measurement of current sensor analog output.
6. Evaluate the difference between each measurement.
7. Evaluate the corresponding change on the analog output of the current sensor when the current limit is increased, this parameter is termed as calibration factor.
8. Multiply the output voltage by the calibration factor which gives the calibrated current value.

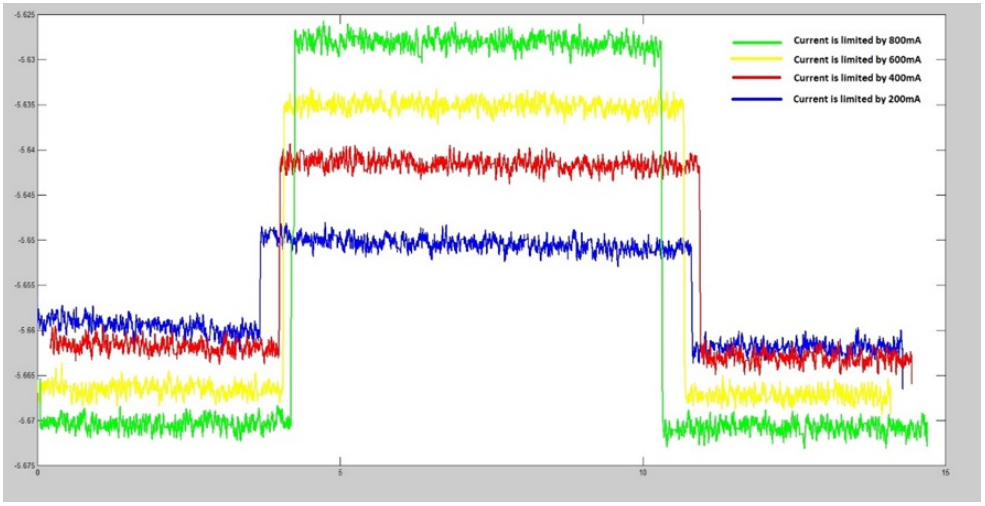

FIGURE 6.18: Current sensor output under different current levels 200 mA, 400 mA, 600 mA, 800 mA.

To apply the calibration processes described above, firstly, a circuit is built and it is supplied by 5 VDC voltage. Then, different current limits are applied to the circuit and the output of current sensor data collected by the dSPACE hardware. The current supplied by the power generator is limited at 200 mA, 400 mA, 600 mA and 800 mA, respectively. Figure 6.18 illustrates the uncalibrated current output data in times (seconds). The calibration cycle is 15 seconds and at approximately the first and last three seconds, the data with neglecting the supply voltage in the circuit is depicted. Although, there is no voltage and current in the circuit at these time periods, there occurs a bias between each measurement varying between -5.65 and -5.67. Therefore, this bias is set to zero in real-time hardware before each measurement is carried out. Then, the corresponding

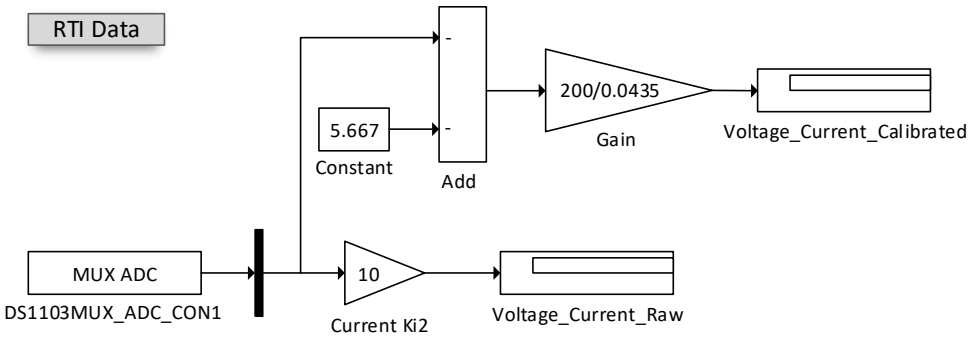

FIGURE 6.19: Calibration model of the current sensor in Simulink.

current output at different current limits are calibrated according to the evaluated bias and calibration factor parameters.

As a result, the calibration factor is calculated as 200/0.0435. The calibration model of the current sensor is developed in MATLAB Simulink which is given in Figure 6.19.

6.5.3 Calibration of the Laser Displacement Sensor

The calibration of laser displacement sensor plays a vital role to have a consistent and reliable data as it is used for the displacement of nozzle. This sensor principally composed of a laser diode, an optical filter, a converging lens, a receiving lens and a position sensitive detector. The calibration process of this sensor is similar to the potentiometers' calibration. In the experimental test, this sensor measures 1 mm nozzle displacements in vertical direction. Therefore, the accuracy of sensor is calibrated to read 0.1 mm intervals.

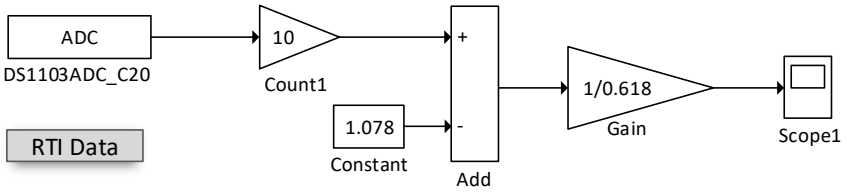

FIGURE 6.20: Calibration model of the laser displacement sensor in MATLAB Simulink.

For the calibration of laser displacement sensor, a linear ruler is used to measure different reference positions. Then, the calibration factor and bias are evaluated by using the output analog data where the supply voltage is 5 VDC. It is concluded that the bias value is 1.078 and the calibration factor is 1/0.618 which is equal to 1.61. The calibration model of laser displacement sensor in MATLAB Simulink is given in Figure 6.20.

6.6 Summary

This chapter has described the development of a real-time experimental setup for the verification of FJ-TVC system.

Firstly, the custom-design of the FJ-TVC test-rig was explained in detail. One of the crucial point in the design of the prototype was that the spring torque of the elastomer material in the flexible joint is provided by the four-symmetrically aligned mechanical compression springs. Secondly, the displacement of the nozzle was also considered in the system model where the frame-in-frame gimbal assembly is moving by a sliding mechanism in vertical direction. Therefore, while gimbal frames enable the nozzle to rotate in yaw and pitch axes, the designed sliding mechanism provides the translation of gimbal frames and nozzle together.

Secondly, the feedback sensors and actuators in the experimental setup were identified and their measurement rates were defined. Moreover, the working principle and technical specifications of the dSPACE hardware were described. It was concluded that the dSPACE hardware is a very powerful electronic card set for the real-time fast prototyping. Additionally, the Controldesk software and its distinguishing features were outlined. Lastly, the calibration procedures for the feedback sensors were defined and the calibration models developed in MATLAB Simulink were given where the model verification of the whole system was planned to be held in the future work.

In the next chapter, the test results obtained from the real-time experimental test setup are outlined and further discussion is also included.

Chapter 7

Experimental Results

In Chapter 5, the controllers developed for the FJ-TVC system were simulated to analyse their performance outputs. Then, to validate the results, the design and commissioning of an experimental setup was described in Chapter 6, where the prototype design, the procedures of the calibration of electronic sensors were detailed in addition to the specifications of the dSPACE real-time HWIL system.

This chapter, as a next step, applies benchmarking to evaluate the tracking control performance of the developed controllers within the experimental test setup. The tests conducted on the setup are for the PID-BB controller, PD-CTCL and $\mathcal{H}_\infty$-CTCL. The verification tests for these controllers are applied for two different pivot positions of the nozzle which are 0 mm and 4 mm, respectively. The parameters measured are the angular errors at yaw-axis and its variation under pivot point displacement. The findings in this chapter are the results of preliminary tests that applied at only one frequency and desired trajectory. The principal limitation of the experimental tests is due to the ABS plastic metarial used in the manufacturing of the test-rig. Even though it is known for its high resilience and impact resistancy, the actuator inputs were limited to avoid any unexpected damage. Additionally, the time constraint is the another limitation of the experimental tests.

The first section describes the test plan for the experiments. Then, the results obtained from the potentiometers are given to evaluate the controller outputs. Lastly, the control performance of each controller is discussed in terms of angular error.

7.1 Test Plan

This section defines the test plan to be followed during the testing life cycle. It involves collecting the data for each control algorithm, measuring how well it is in terms of tracking performance and comparing the results. The desired trajectory is a sinusoidal

path as the trajectory of the FJ-TVC system consists of quarter sinusoidal movements for the stability of vehicle. The sampling time is 0.001 seconds during the experiment. As discussed in previous chapter, the prototype illustrated in Figure 6.1 has been designed to cover linear displacement of nozzle in vertical direction in addition to rotational motions in two axes. Therefore, the control performance of each controller under different pivot point locations are experimentally evaluated in this chapter. It is crucial to emphasise that the size of the actuator signal is limited in the experimental tests due to the following reasons. First of all, the large actuator signal may cause excessive heating and damage the actuator. Secondly, the exceeding of absolute limits (saturation) might cause the plant to be a poor model of the system to be controlled. Thirdly, a large actuator signal can be associated with excessive power consumption. Lastly, excessively rapid changes in the actuator signal might cause undesirable stresses over the test setup where the ABS plastic materials utilised. The constraints can be expressed in terms of slew-rate, saturation and bandwith limitations, which were discussed in Chapter 5. Additionally, as there is no sign about saturation on the actutor signals in the experimental tests, the actuation efforts are not presented. In the experiment, the linear displacement of nozzle is fixed at a certain point by using a metal grabber and hence the experimental tests are performed at two different pivot point locations which are 0 mm origin point and 4 mm maximum allowable displacement point, respectively. The test results given in this chapter are for the trajectory tracking control of nozzle in yaw axis, however, the results for pitch axis are similar to these results due to the symmetrical design of the model. The test plan of the experimental validation consists of the following steps: 1) Generating of the embedded C code for each control algorithm in MATLAB Simulink, 2) Transfering of the C code to the dSPACE electronic card, 3) Building of the real-time interface in the Controldesk software, 4) Setting of the pivot point position of nozzle to the desired point, 5) Implementation of the experimental test, 6) Collection of the data, respectively.

Based on the steps described above, experimental tests are conducted by using developed control algorithms for 0 mm and 4 mm pivot point positions of the nozzle, respectively, and the test results are discussed in the remaining sections.

7.2 Experimental Results - PID-BB Controller

To evaluate the performance of the PID-BB control algorithm, a number of experiments were undertaken and representation results are given in this section. Additionally, the peak value of the angular errors are outlined for the benchmarking of tracking performance of each controller at different pivot point positions.

The control algorithm applied in this section was firstly developed in Section 4.2 and simulated in Sections 5.3.1 and 5.4.2. First simulation was considering the nominal

plant, hence its control performance was in the range of the requirements defined in Table 5.2 in terms of steady state error, rising and settling time. However, when the uncertainties are included in the system model, it was concluded from the simulation study that this classical controller does not provide perfect tracking control where the norm of the angular error at joint was approximately 0.29°, which is higher than the allowable angular limit.

After the implementation of test procedures described in the previous section, the trajectory tracking of the nozzle in yaw axis at 0 and 4 mm pivot point positions are illustrated in Figures 7.1 and 7.3. Additionally, the corresponding angular errors are given in Figures 7.2 and 7.4, respectively, to show the angular error during the test cycle.

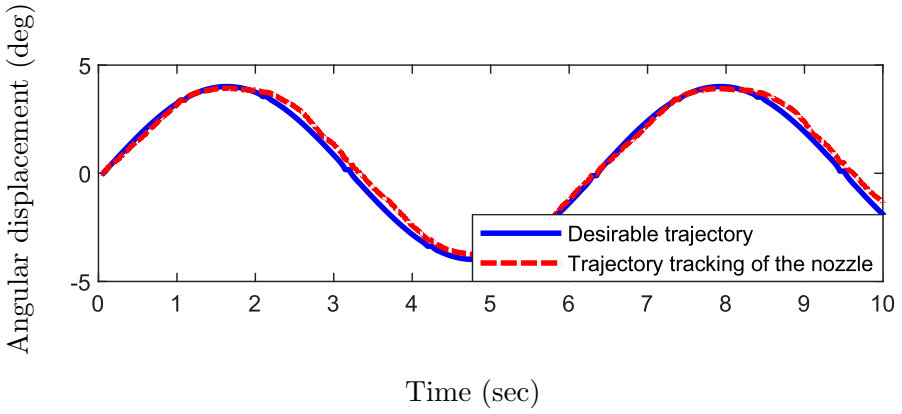

FIGURE 7.1: Trajectory tracking control of the nozzle at 0 mm pivot point position with the PID-BB controller.

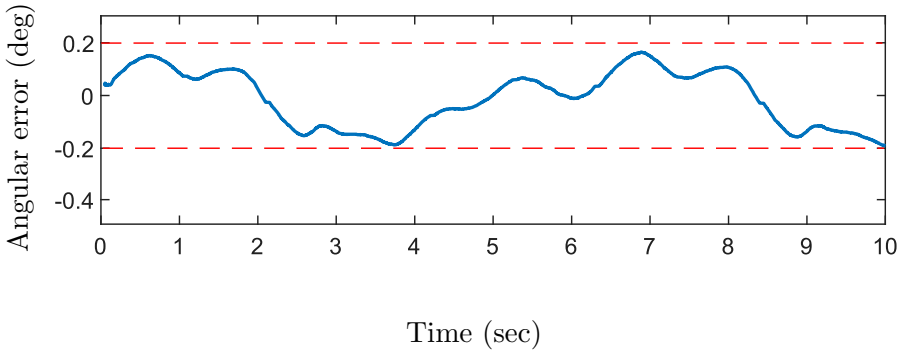

FIGURE 7.2: Trajectory tracking error at 0 mm pivot point position generated by the PID-BB controller.

As seen from Figure 7.1, when the nozzle position is at origin point, the PID-BB controller can follow the desired trajectory in an allowable range. It is worth noting that whereas the tracking performance is good enough over the first two seconds, it almost

achieves error limits after the change of slope of the sinusoidal path from positive to negative which occurs at approximately 1.8 seconds.

In Figure 7.2, the angular error output is given in degrees which is determined by the desired reference input minus the output of the angular position of the nozzle. The maximum angular error measured during the test cycle is approximately 0.19° which is very close to the error limit. The red dashed line in the figure identifies the maximum and minimum bounds of the angular error.

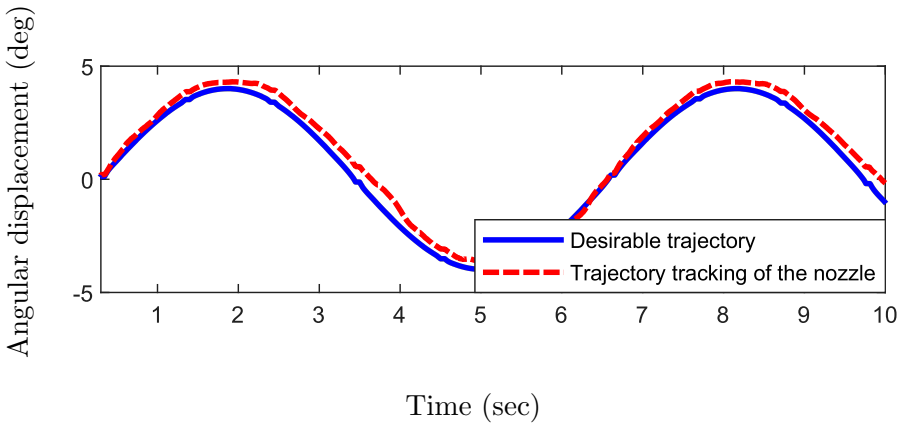

FIGURE 7.3: Trajectory tracking control of the nozzle at 4 mm pivot point position with the PID-BB controller.

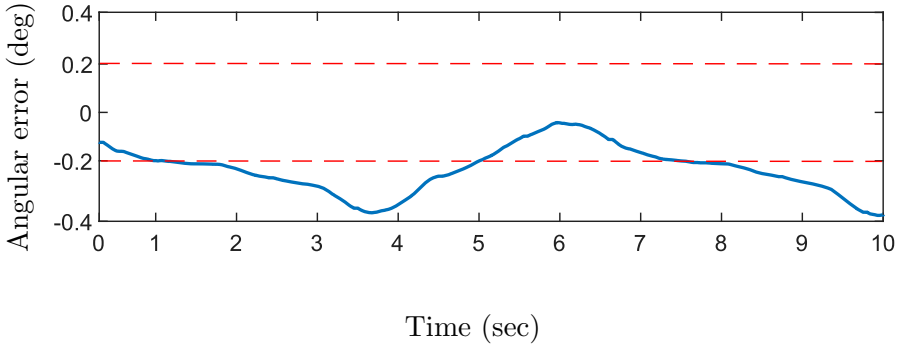

FIGURE 7.4: Trajectory tracking error at 4 mm pivot point position generated by the PID-BB controller.

As a second step of the experimental verification, Figure 7.3 gives the trajectory tracking of the nozzle at 4 mm pivot point position. It is concluded that there is more disruption in the output of trajectory tracking of the nozzle when the pivot point is at 4 mm in the vertical direction. As seen in Figure 7.4, the maximum angular error reachs up to 0.38° which is out of the allowable range.

To assess the performance of the algorithm, the angular joint errors are calculated by evaluating the maximum absolute difference between the desired and actual joint angle

Pivot Point Position (mm)	maximum absolute joint error (deg)
0	0.19
4	0.38

TABLE 7.1: Norm calculation of error signal generated by the PID-BB controller with two different pivot point positions of the nozzle.

during the test. The angular joint errors generated by the PID-BB controller are given in Table 7.1.

In conclusion, it is verified that although the developed conventional controller has good tracking performance when the nozzle is fixed at origin pivot point, it does not maintain the similar performance when the pivot point of the nozzle is displaced and this causes misalignment issues. Note that the results given are the best among a range of tests.

7.3 Experimental Results - PD-CTCL Controller

In this section, the performance result of PD-CTCL controller is given. The theoretical background of this controller was provided in Section 4.3.1. The simulation results were detailed in Sections 5.3.2 and 5.4.3 for the nominal model and the model with uncertainties, respectively. It was concluded from the initial simulation result that its tracking performance is feasible in terms of the requirements in Table 5.2, where the nominal plant was considered. However, the later simulation study showed that angular error exceeds the allowable limit and does not provide acceptable tracking performance, when the uncertainties are included. To verify the simulation results, this section conducts experimental tests for the PD-CTCL controller for two different pivot positions of nozzle which are 0 mm and 4 mm, respectively. Additionally, the angular error results are given for the benchmarking of tracking performance.

Figure 7.5 shows the trajectory tracking output of the nozzle when the pivot position is at the origin point. It is concluded that PD-CTCL controller can track the desired path very well. Additionally, the angular error during the test cycle is shown in Figure 7.6 and it follows that the nozzle can follow the desired trajectory within the allowable error range where the maximum error occured was 0.13°. Moreover, its tracking performance in terms of angular error is lower than the performance of the developed controller in the previous section at 0 mm pivot point position. Since the PD-CTCL is a model based controller, it can give a better result when the plant model is accurately known even though similar conventional controllers are used in the outer loop of the CTCL, which is verified at the specific frequency within this experimental test. However, further tests are required for different frequencies, which are planned to be conducted in the future works.

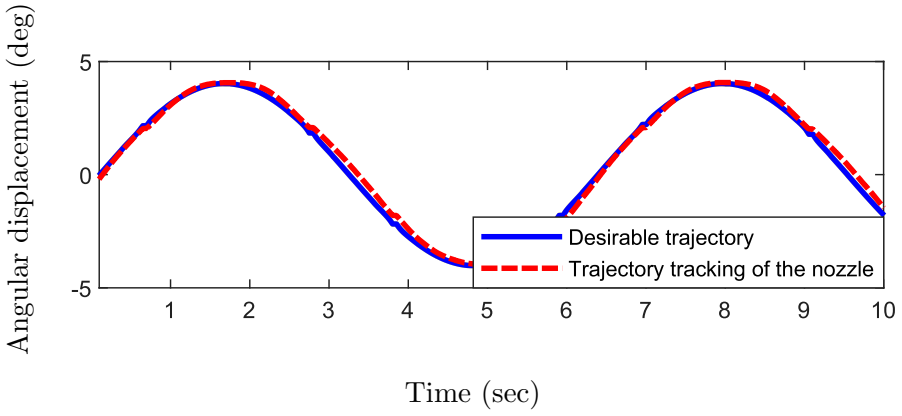

FIGURE 7.5: Trajectory tracking control of the nozzle at 0 mm pivot point position with the PD-CTCL controller.

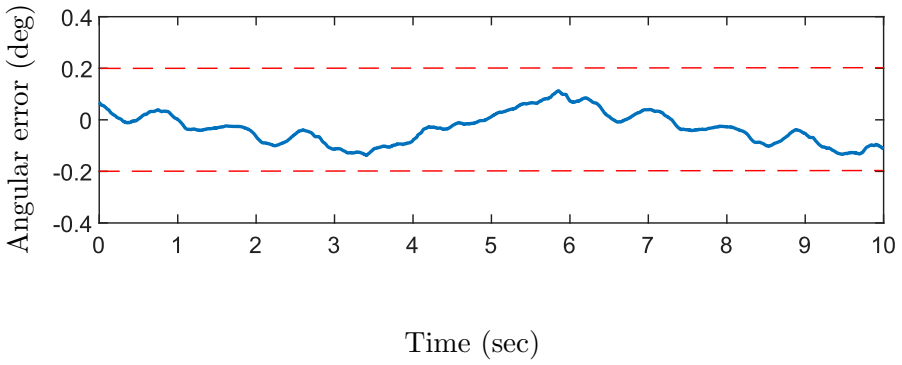

FIGURE 7.6: Trajectory tracking error at 0 mm pivot point position generated by the PD-CTCL controller.

Figure 7.7 shows the trajectory tracking control of the nozzle at 4 mm pivot point position. It is clear that the misalignment issues appears after the displacement of the pivot point. The disruption at the angular position output of the nozzle increases at maxiumum and minimum points of the sinusoidal path. As the pivot point is translated 4 mm in the positive direction of the z-axis, angular misalignment occurs in the nozzle orientation. As seen in Figure 7.8, the maximum angular error at nozzle orientation is measured as 0.34°.

Pivot Point Position (mm)	maximum absolute joint error (deg)
0	0.13
4	0.34

TABLE 7.2: Norm calculation of error signal generated by the PD-CTCL controller with two different pivot point positions of the nozzle.

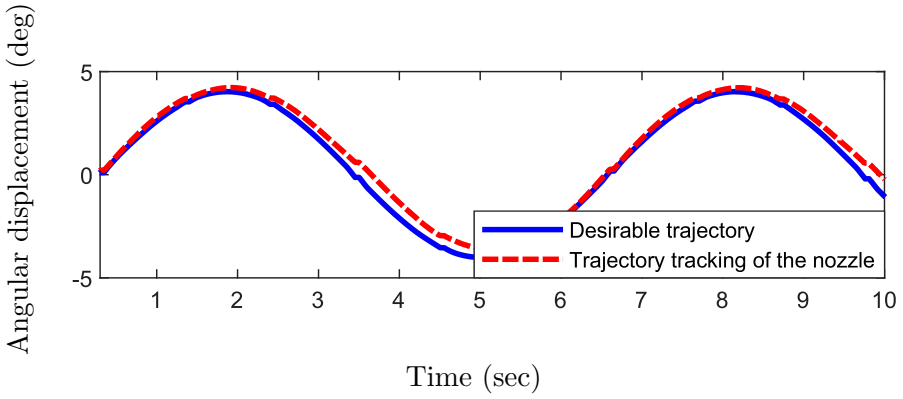

FIGURE 7.7: Trajectory tracking control of the nozzle at 4 mm pivot point position with the PD-CTCL controller.

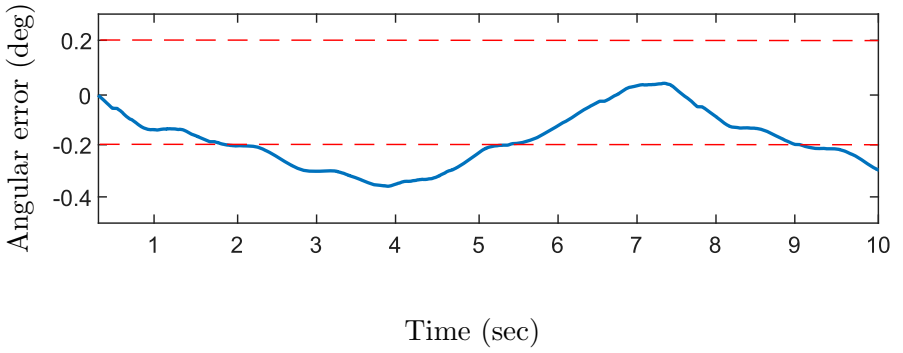

FIGURE 7.8: Trajectory tracking error at 4 mm pivot point position generated by the PD-CTCL controller.

As one measure of the performance of this controller, the angular joint errors are evaluated and the results are given in Table 7.2.

To conclude, it is experimentally verified that the PD-CTCL controller has good tracking performance when the nozzle is at the origin point, nevertheless, its performance gets worse when the pivot point of the nozzle is displaced to the maximum point, 4 mm, and exceeds the angular error limit.

7.4 Experimental Results - Robust $\mathcal{H}_\infty$ CTCL Controller

The experimental results of the $\mathcal{H}_\infty$-CTCL controller is given in this section. The theoretical background of this controller and the corresponding simulation results were discussed in Chapter 5. It was concluded that it achieves an excellent tracking performance as the uncertainties are minimised and the joint errors are decreased to a lower level. For the validation of those results, this section conducts the experimental tests by applying

the $\mathcal{H}_\infty$-CTCL controller at different positions of the pivot point. Then, the angular error results are given for the benchmarking of the trajectory tracking performance.

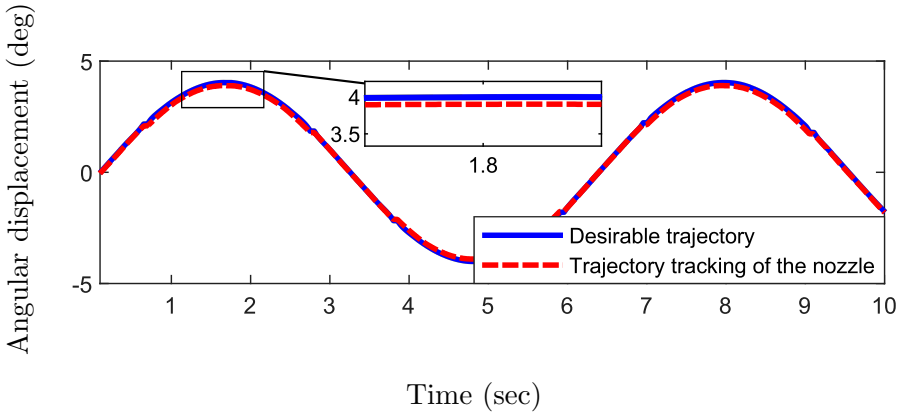

FIGURE 7.9: Trajectory tracking control of the nozzle at 0 mm pivot point position with the $\mathcal{H}_\infty$-CTCL controller.

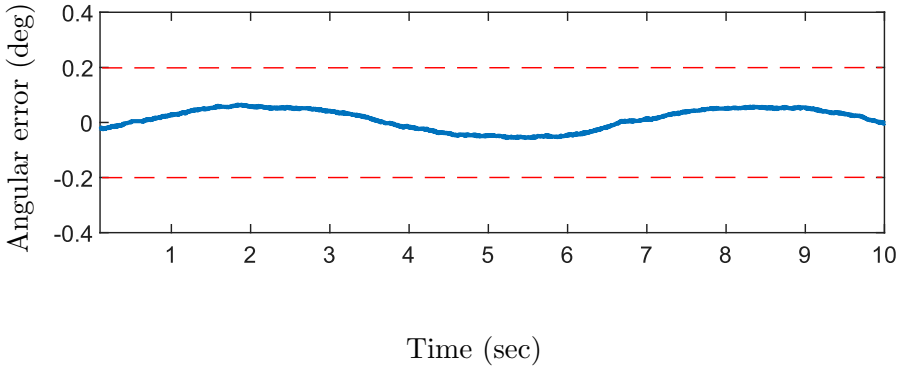

FIGURE 7.10: Trajectory tracking error at 0 mm pivot point position generated by the $\mathcal{H}_\infty$-CTCL controller.

Figure 7.9 shows the trajectory tracking control of the nozzle when the pivot position is at the origin point. For more clarity, a section of the tracking output is zoomed-in and given in the same figure. It is concluded that there is a slight difference between the desirable trajectory and the trajectory tracking of the nozzle. Figure 7.10 demonstrates the angular error on the nozzle orientation, where the maximum angular error is evaluated as 0.08°.

Alternatively, the trajectory tracking control of nozzle is given in Figure 7.11 when the pivot position is at 4 mm. The angular error on the joint axis is given in Figure 7.12 where it is concluded that the maximum angular error is approximately 0.09°. The error signal is not totally symmetrical to the previous test conducted at the origin point of

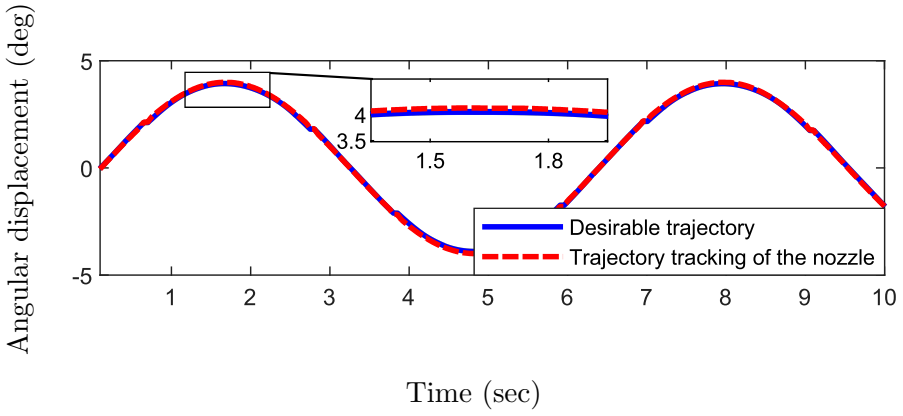

FIGURE 7.11: Trajectory tracking control of the nozzle at 4 mm pivot point position with the $\mathcal{H}_\infty$-CTCL controller.

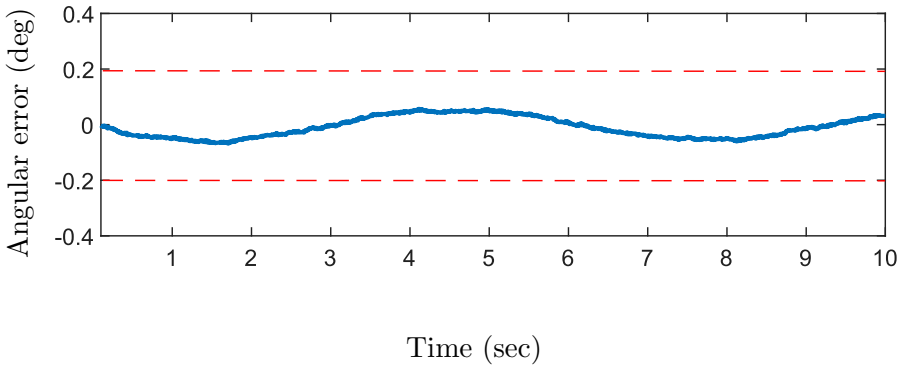

FIGURE 7.12: Trajectory tracking error at 4 mm pivot point position generated by the $\mathcal{H}_\infty$-CTCL controller.

the nozzle, however, the maximum errors at the corresponding joint are close to each other. The angular joint errors are given in Table 7.3.

Pivot Point Position (mm)	maximum absolute joint error (deg)
0	0.08
4	0.09

TABLE 7.3: Norm calculation of error signal generated by the $\mathcal{H}_\infty$-CTCL controller with two different pivot point positions of the nozzle.

In conclusion, it is established that the $\mathcal{H}_\infty$-CTCL has an excellent tracking control performance for preleminary tests for the cases where the pivot point positions are 0 mm and 4 mm, respectively.

7.5 Improved Controller Design

In the initial stage of the experimental tests, the developed algorithm results were verified and compared with the performance results of simulation studies in terms of the angular error. As a next step, the range of the uncertainties for certain parameters are extended to drive the design process to achieve the best trajectory tracking control performance. Moreover, some uncertainties for specific parameters, which have not been defined in the previous analysis, are included in the further analysis. Lastly, the Bees Algorithm is applied to the tuning of the controller parameters where the plant is modelled including extended uncertainties.

7.5.1 Further Modelling of the Parametric Uncertainties

The Monte-Carlo simulation was used in Chapter 5, where the mean and deviations of the physical and geometrical system paramaters were given in Table B.1 (Appendix B). It included mass, inertia, CoG parameters of the links and the linear displacement of the nozzle in the vertical direction. Based on the probability distributions of these parameters, a number of simulations were performed to evaluate the control performance of the developed controllers. However, after the experimental tests in this chapter, it is concluded that some essential steps should be followed for further improvements of the controller design.

Firstly, the experimental tests demonstrated that transferring the stored energy from one compression spring to another in the counter side causes a disruption in the trajectory tracking control performance of the nozzle. The angular error increases at each direction change of the nozzle from 0° in either positive or negative direction. After conducting experimental tests, it was concluded that there are two reasons of this behaviour, the mechanical gap between the springs and having the different stiffness values of the springs. The mechanical gap problem is an obvious area for future research. However, the modelling of the uncertainties for the compression springs is an immediate step to be followed for further analysis in the Monte-Carlo simulation. Therefore, the uncertainties of stiffness coefficient of the springs and its effect on the controller performance during the test cycle is experimentally tested.

Electro-mechanical actuators are subject to the uncertainties due to the several reasons such as operating point changes, perpetual parametric variations due to temperature changes, un-modelled dynamics and asymmetric behaviours (Salloum et al., 2016). In the modelling of the uncertainties of the actuator, the variables of resistance and inductance are included.

Additionally, the uncertainties, which have been previously modelled, are open to improvement by the extension of the uncertainty range. The uniform distribution is used

TABLE 7.4: System parameters and corresponding mean and deviation values.

Parameter	Definition	Unit	Mean Value	σ (%)
R	Resistance	ohm	1.4703	0.0488
k_1	Stiffness coefficient of spring-1	N/m	0.6093	0.1014
k_2	Stiffness coefficient of spring-2	N/m	3.8148	0.0985
L	Inductance	Henry	110×10^{-6}	0.0479
m_1	Mass of *link-1*	kg	0.3490	0.0201
m_2	Mass of *link-2*	kg	0.8306	0.0314
m_3	Mass of *link-3*	kg	2.0736	0.0502
J_{yy}	Inertia of *link-2*	kg.m^2	1.8231	0.0291
J_{zz}	Inertia of *link-3*	kg.m^2	14.8144	0.0476
d	Linear Displacement	m	0.0042	0.0498

and random values are generated in MATLAB by using

$$R = \texttt{normnrd}(\mu, \sigma) \tag{7.1}$$

function which returns a random number chosen from the normal distribution with parameters μ (mean) and σ (standart deviation), respectively. The updated physical and geometrical properties of the system given in Table 7.4 forms the basis of the Monte-Carlo simulation.

7.5.2 The Implementation of the Bees Algorithm

The Bees Algorithm (BA) is a population-based search algorithm that is motivated by the intelligent foraging behaviour of honey bee swarms. In (Yuce et al., 2013), the BA based search algorithm is described and implemented with a number of benchmark functions. The results from the study show that the developed BA based algorithm is more succesfull than the alternative optimization algorithms, such as, the Evolutionary Algorithms (EA), Particle Swarm Optimization (PSO), Ant Colony Optimization (ACO), in terms of accuracy and performance. The BA algorithm is, therefore, used to tune the controller parameters in the PID-BB and PD-CTCL controllers, respectively.

The BA is a competent method to solve many complex multi-variable optimisation problems having more robust and efficient approaches than existing algorithms. As an example, if approximations are satisfactorily selected, then it might find the solution rapidly compared to any other general approach. The BA can also do both local and global search by utilizing exploitation and exploration strategies, respectively (Pham et al., 2005). The pseudo-code of the algorithm is given in Table 7.5. The working principle of the algorithm, firstly, starts with the generation of a random population and send the n scout bees randomly to the selected sites where the Simulink model is run

the implemented parameters in simulation environment in the background. According to the result of objective function, elite and non-elite sites are evaluted. Then, the result of each trial is sorted from the highest to the lowest.

TABLE 7.5: Pseudo code of the BA

```
1.  Generate random population and evaluate fitness
2.  Sort population
3.    While (stopping criteria not met)
4.              For i=1: EliteSite
5.                          Recruit bees for elite site and evaluate fitness
6.                          Select the best bee from each site
7.              End
8.              For i=EliteSite+1 : BestSite
9.                          Recruit bees for best site and evaluate fitness
10.                         Select the best bee from each site
11.             End
12.             For i=BestSite+1: ScoutBee
13.                         Generate random population and evaluate fitness
14.             End
15.    End While
16. Sort population
```

Then, the local search phase starts and finds the best sites, which are the m fittest locations. Also, local search employs forager bees in the neighborhood of the best sites, evaluates their fitness values, in other words objective functions, and selects the best bee from the best site. After that, the global search phase starts with a random search process and the overall locations are put in an array according to their objective function result and the process runs until the global optimum is evaluated.

When designing control systems in general, the integral of the square of the error is used as an objective function (Sahin, 2022), i.e

$$J = \int_0^\infty (r(t) - y(t))^2 dt \tag{7.2}$$

where $r(t)$ and $y(t)$ are the reference and output position parameters, respectively. As the trajectory tracking error is only aimed to be minimised at preliminary experimental tests, (7.2) is sufficient to be used as an objective function.

Given the search strategy of the BA, the parameters used in the algorithm are defined as in Table 7.6. When parameters such as the iteration number of the algorithm increased to more than 1000, the analysis time increases, whereas evaluated controller parameters do not change significantly.

TABLE 7.6: Parameters of the BA

Definition of the parameter	Value
Number of Scout Bees in the Selected Patches (n)	50
Number of Best Patches in the Selected Patches (m)	15
Number of Elite Patches in the Selected Best Patches (e)	3
The size of neighborhood for Each Patches (ngh)	1
Number of Iterations (maxiter)	1000
Difference between the Iterations (diff)	0.001

The controller parameters for the plant including the extended modelling uncertainties are evaluated by the BA. The calculated controller parameters for the PID-BB controller are 154, 0.425 and 3.66, respectively, for the coefficients of proportional, integral and derivative components. For the parameters of the PLC, the magnitude of zero and pole are updated as 0.046 and 5.2, respectively. Alternatively, the evaluated controller parameters for the PD-CTCL are 477 and 145, respectively, for the proportional and derivative terms.

After the updating of the controller parameters, experimental tests are conducted at 0 mm and 4 mm pivot point positions of the nozzle for the benchmarking of the controller performance. In Figure 7.13, the trajectory tracking control of the nozzle with the PID-BB controller is given where two different sets of controller parameters are used. The first controller uses the previously designed control parameters, whereas the alternative model employes the updated parameters evaluated by using the BA including the extended modelling uncertainties, which are termed the PID-BB controller with old parameters and updated parameters, respectively.

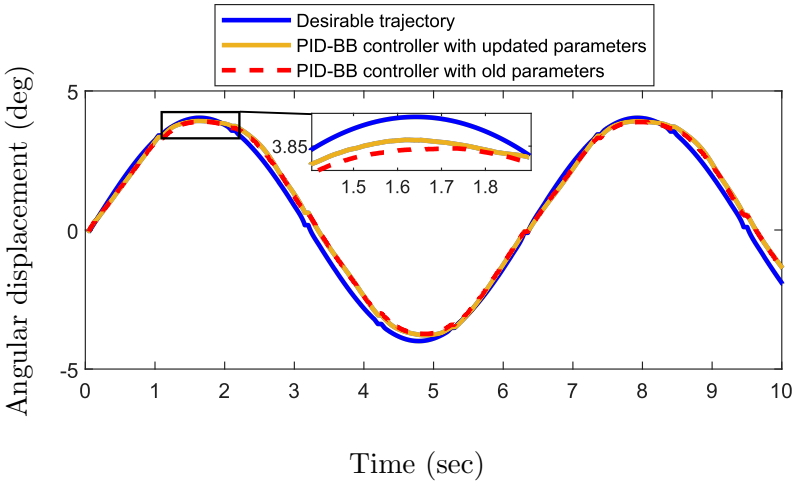

FIGURE 7.13: Trajectory tracking control of the nozzle at 0 mm pivot point position with the PID-BB controller. The controllers compared are seperated from each other in terms of controller parameters.

Figure 7.13 shows that when the controller parameters are tuned with the BA and the uncertainty model is improved by including the previously unmodelled parametric uncertainties, the trajectory tracking control performance of the system is improved, yet no significant change occurs. In terms of angular error, the maximum value is evaluated as 0.15°, which was previously 0.19°. Therefore, it is concluded that the characteristic behaviour of the trajectory tracking of the nozzle is almost similar, only minor performance improvements are observed at the peak values of the sinusoidal reference trajectory.

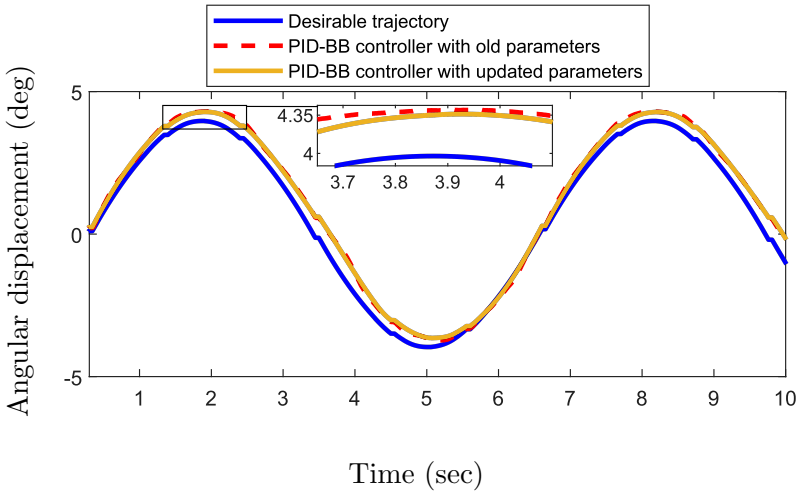

FIGURE 7.14: Trajectory tracking control of the nozzle at 4 mm pivot point position with the PID-BB controller. The controllers compared are seperated from each other in terms of controller parameters which are previously designed parameters and the updated parameters.

Figure 7.14 compares the trajectory tracking control of the nozzle at the 4 mm pivot point position where the PID-BB controller is applied with two different sets of controller paramaters. The maximum angular error is calculated as 0.34° within the experimental tests, which was previously 0.38°. The results obtained from these results show that even though minor improvements occur on the system performance, the PID-BB controller still does not achieve excellent tracking control performance as obtained with $\mathcal{H}_\infty$-CTCL.

In Figure 7.15, the trajectory tracking control of the nozzle at the 0 mm pivot position with the PD-CTCL controller is displayed where two different sets of controller parameters are used. The difference between the controllers is given in a separate section which is zoomed-in for more clarity. What stands out in this figure is that there has not been a substantial improvement on the trajectory tracking control of the nozzle, where only slight improvements occurs locally at maximum values of the desirable trajectory.

In Figure 7.16, the test results of the PD-CTCL controller are given where the pivot point of the nozzle is set to 4 mm. The control performance of the PD-CTCL controller with two different sets of control parameters are compared, and it is observed that

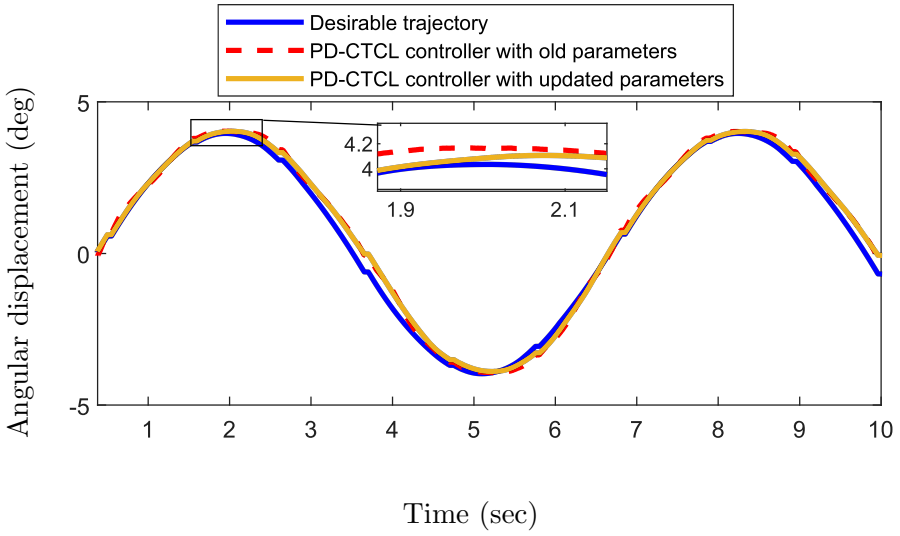

FIGURE 7.15: Trajectory tracking control of the nozzle at 0 mm pivot point position with the PD-CTCL controller. The controllers compared are seperated from each other in terms of controller parameters which are previously designed parameters and the updated parameters.

the control performance of the system does not change considerably, even though the controller parameters are tuned with the BA and further modelling of the uncertainties are included for the enhancement of the controller.

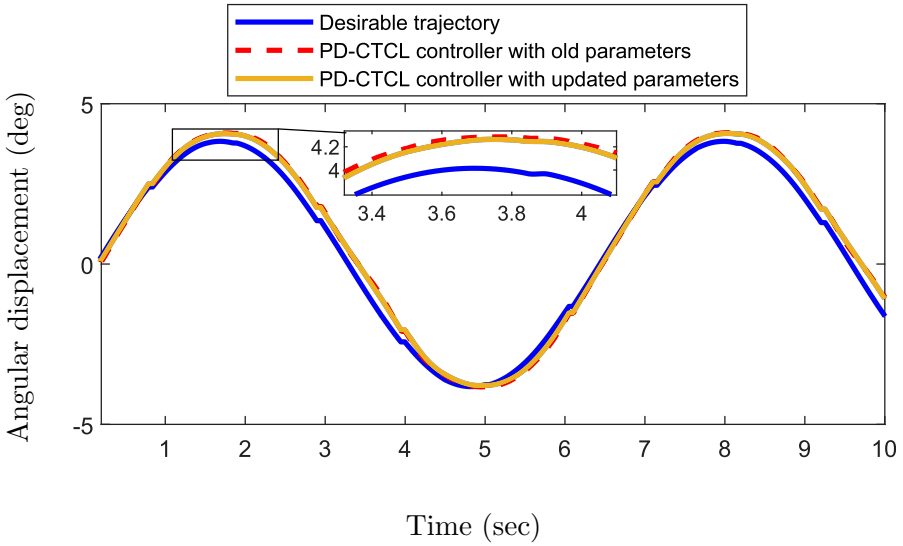

FIGURE 7.16: Trajectory tracking control of the nozzle at 4 mm pivot point position with the PD-CTCL controller. The controllers compared are separated from each other in terms of controller parameters which are previously designed parameters and the updated parameters.

7.6 Discussion of the Experimental Test Results

In the simulation studies, see Chapter 5, it was concluded that, when the controllers were simulated for the nominal plant, both the PID-BB and PD-CTCL controllers achieved good performance on the tracking control of the FJ-TVC system. The steady state errors were approximately 0.02° and 0.01°, respectively, for the 0.8° reference input signal. However, when the uncertainties were considered in the plant model, it was concluded that the steady state errors were approximately 0.36° and 0.28°, respectively. Therefore, to satisfy the requirements which is only possible with the minimisation of the effects due to the uncertainties, $\mathcal{H}_\infty$-CTCL was developed and applied in simulation environment. It was then concluded that robust $\mathcal{H}_\infty$-CTCL achieves excellent tracking control performance where the steady state errors are less than 0.05°.

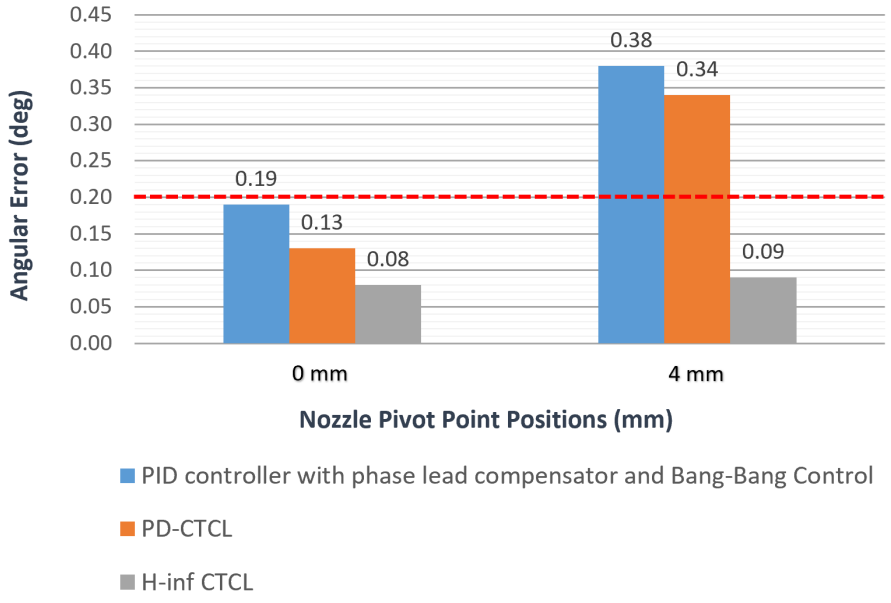

FIGURE 7.17: Comparison of angular errors in terms of the controllers and the pivot point positions of nozzle

In order to validate the simulation results, the three developed controllers were tested on the FJ-TVC experimental setup. Then, the results in Figure 7.17 are obtained where it is divided into two groups which are corresponding to 0 mm and 4 mm pivot point positions of the nozzle and the y-axis of the figure shows the angular error in degrees. The red dashed line also indicates the maximum limit of the angular error.

The experimental test results confirm that, when the pivot point of the nozzle is at 0 mm, the angular errors are 0.19°, 0.13° and 0.08°, respectively, for the PID-BB, PD-CTCL and $\mathcal{H}_\infty$-CTCL controller. Therefore, it is concluded that all the three controllers satisfy the tracking control performance. However, amongst these results, while the $\mathcal{H}_\infty$-CTCL exhibits excellent tracking performance in terms of angular error, the model using PID-BB controller gives poorer results.

Conversely, when the pivot point position is at 4 mm, it is concluded that only the robust $\mathcal{H}_\infty$-CTCL controller gives a superior tracking control performance where the angular error is almost similar to the result of 0 mm of pivot point position. The angular errors of the PD-CTCL and the PID-BB controllers are almost doubled which confirms that they can not minimise the effects due to the uncertainties. It is also concluded that even though PD-CTCL is a model-based controller, it is not capable of minimising the uncertainties when it is combined with a conventional controller.

7.7 Summary

This chapter conducts the experimental tests to validate the simulation results obtained from the tracking control of the FJ-TVC system. To do this, firstly a test plan of the experiments was defined which forms the basis of the procedures to be followed during the test cycle. Then, the three controllers, which are PID-BB, PD-CTCL and $\mathcal{H}_\infty$-CTCL were tested for the two different nozzle positions. The positions for the pivot point were set as 0 mm and 4 mm, respectively. The tests were essential as it was able to identify the controllers whose performances are limited or acceptable in terms of core requirements. Additionally, it was experienced that the experimental tests with the custom-design test-rig in the HWIL system is the substantial part of the work to verify the test results obtained from simulation outputs. Moreover, a user-friendly interface developed for controlling of the system provided a remarkable coordination between the MATLAB/Simulink model and the test-rig setup where the Simulink model is embedded into the real-time hardware, required torque inputs are fed into the custom-design controller card, then the nozzle rotates depending on the magnitude of generated force and feedback sensors supply the output data into the control loop to achieve excellent trajectory tracking.

It was concluded from the experimental tests that all three developed controllers in this research give feasible tracking control performance in terms of angular error when the pivot point of the nozzle is at origin position. It is worth noting that robust $\mathcal{H}_\infty$-CTCL was the best solution amongst the tested controllers. Conversely, after the experiments were conducted again for the 4 mm pivot point position, PID-BB and PD-CTCL controllers were out of the acceptable range of the angular error as the errors were almost doubled. However, $\mathcal{H}_\infty$-CTCL kept its performance in the similar level and gives excellent tracking control performance.

Additionally, further analysis and improvements are conducted on the PID-BB, PD-CTCL controllers to drive the design process to achieve the best trajectory tracking control performance. The range of the uncertainties for certain parameters are extended to cover additional parametric uncertainties. Then, the BA is applied to the tuning of the controller parameters where the plant is modelled with extended uncertainties.

Nevertheless, the obtained test results showed that a conventional PID-BB controller, and a model-based CTCL with a PD controller in its outer loop do not satisfy the controller requirements even though further analysis and tests. However, further experiments within different scenarios, such as different desired trajectories at possible high and low freqencies, are planned to be conducted in the future works. Furthermore, the relationship between the choice of the weighting functions and frequency responses to the behaviour seen in practice will be further investigated for the $\mathcal{H}_\infty$-CTCL method.

The next chapter draws general conclusions from the results in this thesis and gives avenues for possible future research.

Chapter 8

Conclusions and Future Work

The aim of this thesis was to develop a robust controller for the FJ-TVC system, motivated by the dynamic modelling limitations of the flexible joint. The study in this thesis has identified several characteristic features of the FJ-TVC system that makes it an unrivalled solution for most of the spacecraft and launcher systems. The major advantages of the FJ-TVC system can be listed as having of a longer lifespan, negligible thrust loss, minimal maintenance and greater energy efficiency. Conversely, it is worth emphasising that the spring torque encountered by the flexible joint increases significantly when the nozzle angle is greater than 10°. Operation out of this limit, therefore, might require more powerful actuators that are not feasible in practice. Alternatively, different methods have been proposed in the literature to classify the TVC system demanding larger steering angle, e.g., the mechanical deflector and the secondary fluid injection for the fixed nozzle, and the gimbal-joint mechanism for the movable nozzle system. These alternative methods provide a higher steering angle, however, the major drawbacks of these approaches can be discussed under three headings, which are the having of the huge amount of thrust loss, the being in need of heat resistant material or reservoir for fluid injection and lastly the having of an inefficient power consumption with very limited lifespan.

It was concluded that there is a growing body of literature that recognises the importance of the FJ-TVC system. Nevertheless, recent developments have heightened the need for a more accurate dynamic model and robust controller for the FJ-TVC system to achieve excellent trajectory tracking as the studies still hold a potential weakness in practice. Prior studies predominantly have showed that the dynamic models developed for the FJ-TVC system include the nozzle orientation in yaw- and pitch-axes. However, this was a simplification of the dynamic model that causes misalignment issues due to the displacement of pivot point in the vertical direction. Previously reported research conducted structural analysis and experimental tests to evaluate the vertical displacement of the nozzle. It was then concluded that the displacement of the nozzle in the vertical direction is not at a negligible level and must be included in the dynamic modelling

since the behaviour of the flexible joint could change significantly under different motor pressures and environmental conditions such as high temperature and low pressure.

The major objective of the research reported in this thesis was, consequently, to model the dynamical behaviour of the FJ-TVC system and develop a robust controller for tracking control of the desired trajectory. Within this framework, a custom-design experimental test-rig of the FJ-TVC system was built by including its dominant features, which is also the main strength of this thesis. Although the design criteria of the test-rig were defined in Section 6.1, one of the approaches about the test-rig design is crucial to discuss in detail. The genuine FJ-TVC model is a single-body system consisting of the flexible joint integrated to the nozzle. Nevertheless, the experimental test-rig provided for the studies in the thesis was designed as a multi-body system including compression springs to simulate the rotational motion of the flexible joint and the frame-in-frame gimbal mechanism for the vertical motion of the nozzle. This novel design approach was investigated since the modelling and manufacturing of the elastomer material are of the different field of the research. Additionally, it was considered that single-body models without flexible joints are not able to allow pivot point displacement in any direction, which has been attempted to design by using the spherical joint mechanism in the literature, see (Li et al., 2011; Yu and Shu, 2017), and raised potential notable misalignment issues in practice due to the negligence of nozzle translation in its longitudinal axis.

Another strength of this thesis appears to be the first study to benchmark the controller performances of the FJ-TVC system within a more accurate dynamic model by implementing in a real-time HWIL system. Nonetheless, there are some assumptions that dynamic modelling is derived based on and need changing to be applied for the genuine FJ-TVC system. First of all, due to the modelling of a multi-body system, there exists different mass and moment of inertia parameters for each link, which, however, has to be updated for a single-body system with an overall mass and inertia by following the same procedure in the mathematical model derivation. Secondly, the gravity acceleration was taken as a constant in the upright direction, $g \approx 9.8$ m/s^2, which was the average value near Earth's surface. However, the systems like spacecraft and launcher systems use an Inertial Measurement Unit (IMU) compatible with World Geodetic System (WGS-84). The gravity acceleration, therefore, has to be a variable provided by the IMU system.

In accordance with the above-mentioned aim and objectives, the several technical steps were followed to propose a conceptual theoretical and practical framework, which were:

1. To overview the FJ-TVC systems and identify the relevant studies and gaps in the existing research.

2. To develop a more accurate dynamic model for the FJ-TVC system including previously neglected terms.

3. To simulate and assess a conventional control scheme where a PID controller with phase-lead compensator and Bang-Bang control which was the most feasible controller to emerge from the literature review.

4. To simulate and assess a model-based controller alternatively in which CTCL method was the widely used technique amongst the model-based controllers developed for the nonlinear manipulators (Lewis et al., 2003).

5. To design and manufacture a test-rig of the FJ-TVC system.

6. To integrate the dSPACE real-time HWIL system and software components into the experimental test setup including the custom-designed FJ-TVC test-rig.

7. To integrate and calibrate the electronic sensors into the experimental test setup for the feedback control.

8. To conduct experimental tests for the verification of simulation based control performance outputs.

The development stages are aligned with the chapters of thesis. A detail of each chapter is provided next.

Chapter 2 overviewed TVC systems and highlighted the significance of the FJ-TVC type. It was described that several distinguishing features of the FJ-TVC make it a unique solution for the control of specific applications such as launchers and spacecrafts. These features were having a longer lifespan, absence of moving mechanical parts, demanding less maintenance and requiring less power for low steering angles. In addition, the identification of relevant methods and gaps in the existing research were provided. Publications, which develop controllers for the trajectory tracking of the TVC system, assumed that the nozzle is fixed by spherical joint mechanism and only orientates in the yaw- and pitch-axes. Moreover, most of them applied conventional control techniques and did not consider the modelling uncertainties although it was a substantial part of the robust control design.

In Chapter 3, a novel dynamic modelling of the FJ-TVC system was developed to account for the orientation of nozzle and avoid the misalignments due to the displacement of pivot point in the vertical direction. This was a major step in developing the system that has a similar dynamic model to the FJ-TVC system. To do this, commonly used mathematical modelling methods were overviewed briefly first, then the advantages of the Lagrange's energy equation for multi-body systems were discussed. Providing very compact equations even for the complex systems was the most crucial feature of Lagrange's energy approach as it considers the system model as a whole. It was also discussed that the resultant closed-form expression obtained within this method was suitable to be directly used in the controller design, where the joint displacements and required torques can be evaluated in a straightforward way.

Chapter 4 then addressed the next critical development stage which was the controller design for the trajectory tracking of the FJ-TVC system. The first step was to give a brief review of conventional and modern control techniques including their advantages, limitations and up-to-date research. Then, the theoretical evaluation of the three developed controllers were given in detail, i.e., PID controller with phase-lead compensator and Bang-Bang control, PD-CTCL and H_∞-CTCL, respectively. The PID controller with phase-lead compensator and Bang-Bang control was the most feasible controller in terms of straightforward design procedures, high accurate tracking control performance and stability, which was developed for the FJ-TVC system in the literature. As an alternative, a model-based controller CTCL method was developed which can compensate the nonlinear dynamic terms, decouple the interactions between the degrees of freedom and ensure globally asymptotic stability. Since this controller also enabled different control methods in its outer loop design, conventional PD-CTCL and robust H_∞-CTCL were developed for this particular controller. The crucial part of this stage was the derivation of the optimisation problem in H_∞-CTCL design, which was derived with the LMI based approach. This approach has become a well-known solution in last decades, playing the similar crucial role as Lyapunov and Riccati equations played in the modern engineering theory.

In Chapter 5, the results of simulation studies by using the developed controllers in Chapter 4 were given. Each controller was implemented in the MATLAB Simulink environment within two different system models, where the initial model used nominal model of the FJ-TVC system, whereas the alternative included terms to represent the uncertainties in addition to its nominal model. The simulation results for the initial plant model showed that all the developed controllers achieve a good tracking performance where the steady state errors were less than 0.02% and the settling time was around 0.05 secs for the 2% error tolerance band. Conversely, in the alternative model, the uncertainties were assumed in polytopic form and modelled by using the Monte-Carlo simulation where the maximum and minimum values of the vertices corresponding to the polytopic form were evaluated. In particular, the normal distribution was considered in the Monte-Carlo analysis and the worst-case effects of the uncertainties were modelled. Then, the simulation studies were performed again for the alternative model and the control performance degradation of each controller were discussed. It was concluded that even though H_∞ CTCL maintains its superiority for over the developed controllers, the conventional approaches could not satisfy the control performance requirements. Therefore, it was clearly shown that the disturbances due to the uncertainties and unmodelled dynamics were decreased to a lower level with robust H_∞-CTCL design.

Chapter 6 described the development process of the FJ-TVC experimental test setup with an eight-step procedure. The prototype design of the FJ-TVC test-rig was the first step, then followed by the specification of the actuators and electronic sensors, the integration of hardware and software components, the embedding of the developed

control algorithm into the hardware, the building of a real-time interface and the calibration of the sensors, respectively. Amongst these steps, the most complicated and critical process was the CAD design of the FJ-TVC test-rig. In the prototype design, the first crucial point was the flexible joint mechanism, which was replicated by using the four-symmetrically aligned compression springs instead of molded elastomer and curved metal plates. Therefore, the spring torque of the flexible joint was provided by the mechanical springs such that when the angle of nozzle increases, the counter-load of the joint increased similarly. Secondly, it was an inovative step that the displacement of the nozzle was designed in 3-DoF, where the developed frame-in-frame gimbal assembly included the orientation of nozzle in yaw- and pitch-axes, then its integration into a sliding mechanism provided motion in the vertical direction. The custom-design test-rig of the FJ-TVC system with these features is a unique solution in this specific field. In addition, the distinguishing specifications of the dSPACE were also detailed in the chapter, where it was emphasised that it is a very competetive hardware for the real-time fast prototyping. Lastly, the calibration prodecures were given to get reliable data from the feedback sensors, and their calibration models were designed in MATLAB Simulink.

The final chapter conducted experimental tests in the developed experimental test system and applied benchmarking to evaluate the tracking control performance of the previously simulated controllers. The verification tests of each controller were performed at two different pivot positions of the nozzle which were 0mm and 4mm, respectively. The parameters measured were the angular errors at yaw-axis and its variation under pivot point displacement. The orientation of the nozzle at the origin point was controlled with the three developed controllers seperately, and it was concluded that all the controllers give feasible tracking control performance in terms of angular error. It was also emphasised that Robust $\mathcal{H}_\infty$-CTCL was the best solution amongst the controllers tested. Conversely, after the experiments were tested again for the 4mm pivot point position, the results from the PID controller with phase-lead compensator and Bang-Bang control, and PD-CTCL methods were out of the acceptable range of the angular error as the errors were almost doubled when compared to previous tests. However, $\mathcal{H}_\infty$-CTCL maintained its performance in the similar level and achieved an excellent tracking control performance where the infinity norm of the angular error was evaluated as 0.09 during the 10 seconds test cycle.

In summary, the research in this thesis developed a novel dynamic model for the FJ-TVC system and designed conventional and model-based controllers in a simulation environment for the trajectory tracking of the nozzle where $\mathcal{H}_\infty$-CTCL satisfied the required performance goals. The verification tests of the developed controllers were also conducted on the experimental test setup for two different test cases, and concluded that $\mathcal{H}_\infty$-CTCL is capable of minimising the uncertainties and achieves excellent trajectory tracking. However, it was unfortunate that the thesis have some weaknesses which can

be criticised due the following reasons: Firstly, more experimental tests should be performed under different scenarios. Secondly, the benchmarking of the controller designs should be carried out within different controller parameters. Additionally, the structure of the FJ-TVC test-rig developed for the laboratory tests had some constraints in terms of forces applied by the actuators, which, therefore, has been led to the limited boundry conditions for the test plan. Moreover, some attempts have been made to investigate the main purpose of the Phase-lead compensator in the implementation of the PID-BB controller, however, it has not been supported by adequate experimental tests. Therefore, it can be concluded that the lack of compensator might not affect the controller performance, which needs more analysis to achieve improved results. Also, for the $\mathcal{H}_\infty$-CTCL design, the theoretical background of the sensitivity and co-sensitivity functions are not covered, where only several studies and textbooks, providing comprehensive analysis and well-known methods such as μ analysis and loop-shaping method, were cited for further details. All these weaknesses rely majorly on the time-constraints in the study. Furthermore, the obvious difficulties on the designing of the FJ-TVC system test-rig, the derivation of mathematical model of the system and the building a test setup including the HWIL system to perform designed controllers on the system caused a wider schedule than the planned. The results, therefore, should be considered from this perspective. Consequently, the future work involves the short and long term plans to fill these gaps in the field.

The next section explains the future studies of this research.

8.1 Future Work

To achieve a further increase in dynamic model and robust controller for the FJ-TVC system, further research within this project should be carried out. Future work can be divided into short- and long-term goals. Short-term goals are more straightforward to evaluate and easier to implement, whereas long-term goals require further modelling and development processes.

The short-term future work will focus on further improvement of the dynamic modelling of FJ-TVC. Although the derived model matches with the dynamical behaviour of the FJ-TVC system, there are still some terms that needs to be considered to provide accurate mathematical models for use in controller design.

Firstly, the friction force between the mechanical parts was neglected in the dynamic model, however it can be crucial when the friction constant and the applied load is in considerable level. The example of this could arise in the joint linking the actuator to the hinge point of the nozzle.

Moreover, the friction torque in the bearing was not included in the dynamic model. If the environmental condition is severe, which is highly possible for the FJ-TVC system, the procedure for the coating process in the bearing increases, and hence it causes the rotational torque to increase dramatically. The solid lubrication is one of the available processes for such systems and hence the modelling of rotational torque is required.

Additionally, it was assumed that the elastomer material is uniformly distributed in the flexible joint structure. It meant that the spring torque has an exactly the same behaviour at different angular positions of the flexible joint. Nevertheless, a uniform distribution is not 100% achievable due to the molding processes and the structural inspection of the flexible joint is an expensive procedure in addition to requring several different processes where most of them taking a quite long time. Therefore, the variation of the spring torque should be modelled in the dynamic model. This is also practical in the prototype design which can be provided by using the compression springs with different spring constants. Additionally, the four-symmetrically aligned compression springs were used within the prototype design of this research, however, if the number of springs could be increased to eight in addition to their different spring constants, more accurate and reliable system will be modelled.

Lastly, model validation is a crucial step to confirm that the developed model actually meets its requirements. Even though each feedback sensor used in the model are calibrated to give more reliable results, model validation enables the researchers to determine the overall error accumulated by the error tolerances of subcomponents.

The long-term future work will firstly concentrate on the improvement of the control performance results from the short-term goals. To do this, the bound of uncertainties will be further extended to include unmodelled effects which are emphasised above in detail. Furthermore, in addition to the uncertainty model development, interplay between linear/non-linear aspects of the system model will be benchmarked. A commonly known approach, the Monte-Carlo analysis will be used for the modelling of the uncertainties.

Another long-term future work will be modelling of the disturbances resulting from vibration. In aerospace applications, especially, the systems having a high power engine are exposed to high frequency vibrations in addition to the aerodynamical effects. Absorbers are designed to surpass these effects, nevertheless, the modelling of these disturbances is a necessary step in applied systems to achieve a robust controller. In the FJ-TVC system, the flexible-joint mechansim is behaving as an absorber on its own for high frequency vibrations, however, the minimisation of the low frequency disturbances to a lower level is possible by a robust controller considering these effects.

Moreover, long-term future work will require an original flexible-joint mechanism with the combination of alternate layers of elastomer material and curved metal plates to verify the test results from the scaled prototype. This requires the identification of the materials for elastomer, sealing and metal plates; the design of layers in terms of their

thickness and quantity; the structural analysis to satisfy the required physical and operational requirements; and applying of the molding processes, respectively. Additionally, the manufacturing and coating processes within a high grade metal alloys and protective chemical ingredients will also be required for the nozzle and the other components in the system for the further tests as explained next.

Furthermore, environmental tests within the upgraded FJ-TVC system will be conducted in the test chambers. These tests will be demonstrating the particular range of temperature, pressure, and vibration conditions, respectively. Also, the physical and control performance requirements will be verified under different combination of these environmental conditions in the test chambers.

Lastly, more experimental tests will be performed for the benchmarking of the control algorithms over the several different desired trajectories having low and high frequencies. Additionally, for each set of test, different controller parameters will be applied, i.e., by choosing of different weighting functions for the loop-shaping design to incorporate the performance/robustness trade-off with the guaranteed stability properties of $\mathcal{H}_\infty$ design method. All the result will be tabulated for the variations of different pivot point positions at x-axis, which can be listed as x_1, x_2, x_3 at 1 mm, 2 mm, 3 mm, respectively, in addition to the cases at 0 mm and 4 mm. Also, further measurement techniques will be utilised to evaluate the orientation of the nozzle more accurately, where the 3-D Digital Image Correlation (DIC) method is one of the solutions.

Appendix A

Linearised Model of the FJ-TVC System

The linearised state-space model is given as $\dot{\boldsymbol{x}} = \boldsymbol{A_{lin}}\boldsymbol{x} + \boldsymbol{B_{lin}}\boldsymbol{u}$ where $\boldsymbol{x} = [d\ \theta_y\ \theta_z\ \dot{d}\ \dot{\theta_y}\ \dot{\theta_z}]^T$ and $\boldsymbol{u} = [F_y\ F_z]^T$. The matrix $\boldsymbol{A_{lin}}$ and $\boldsymbol{B_{lin}}$ are as follows:

$$\boldsymbol{A_{lin}} = \begin{bmatrix} 0 & 0 & 0 & 1 & 0 & 0 \\ 0 & 0 & 0 & 0 & 1 & 0 \\ 0 & 0 & 0 & 0 & 0 & 1 \\ a_{41} & 0 & 0 & 0 & 0 & 0 \\ 0 & a_{52} & 0 & 0 & 0 & 0 \\ 0 & 0 & a_{63} & 0 & 0 & 0 \end{bmatrix} \qquad \boldsymbol{B_{lin}} = \begin{bmatrix} 0 & 0 \\ 0 & 0 \\ 0 & 0 \\ b_{41} & b_{42} \\ b_{51} & 0 \\ 0 & b_{62} \end{bmatrix} \tag{A.1}$$

where

$$a_{41} = -\frac{k_2}{m_x}$$

$$a_{52} = -\frac{k_1 l_y^2 - g l_y m_y}{J_{yy} + m_y l_y^2 + m_z l_z^2}$$

$$a_{63} = -\frac{k_1 l_z^2 - g m_z l_z}{J_{zz} + m_z l_z^2}$$

$$b_{41} = -\frac{d + (d_{OB}\cos(\alpha_2))/d_{AC}}{m_x}$$

$$b_{42} = \frac{d + (d_{OB}\cos(\alpha_2))/d_{AB}}{m_x}$$

$$b_{51} = \frac{C_x(d_{AR} - (d_{OC}\sin(\alpha_2))/d_{AC}) + C_z(d + (d_{OC}\cos(\alpha_2))/d_{AC})}{J_{yy} + m_y l_y^2 + m_z l_z^2}$$

$$b_{62} = \frac{B_x(d_{AR} - (d_{OB}\sin(\alpha_2))/d_{AB}) + B_y(d + (d_{OB}\cos(\alpha_2))/d_{AB})}{J_{zz} + m_z l_z^2}$$

Appendix B

Physical and Geometrical Properties of the System

Table B.1 Physical and geometrical properties.

Parameter	Definition	Value	Unit
m_1	Mass of *Link-1*	0.349	kg
m_2	Mass of *Link-2*	0.83	kg
m_3	Mass of *Link-3*	2.073	kg
l_2	Length between the pivot point O and the CoG of the nozzle	0.16	m
l_3	Length between the pivot point O and the total CoG of *Link-2* and *Link-3*	0.11	m
k_1	Stiffness coefficient of spring-1	0.6093	N/m
k_2	Stiffness coefficient of spring-2	3.8148	N/m
d_{OB}	Length between the pivot point O and the hinge point B	0.258	m
d_{OC}	Length between the pivot point O and the hinge point C	0.258	m
d_{CD}	Length between the hinge points of the actuator-1, C and D	0.262	m
d_{AB}	Length between the hinge points of the actuator-2, A and B	0.262	m
d_{DR}	Length between the actuator-1 hinge point D and the reference point R	0.167	m
d_{AR}	Length between the actuator-2 hinge point A and the reference point R	0.167	m
C_x	Isometric length of the actuator-1 hinge point C over x-axis	0.220	m
C_z	Isometric length of the actuator-2 hinge point C over z-axis	0.134	m
B_x	Isometric length of the actuator-2 hinge point B over x-axis	0.220	m
B_y	Isometric length of the actuator-2 hinge point B over y-axis	0.134	m
J_{yy}	Moment of Inertia of *Link-2* about y-axis	1.823	kg.m^2
J_{zz}	Moment of Inertia of *Link-3* about z-axis	14.814	kg.m^2

Appendix C

BLDC Actuator Model

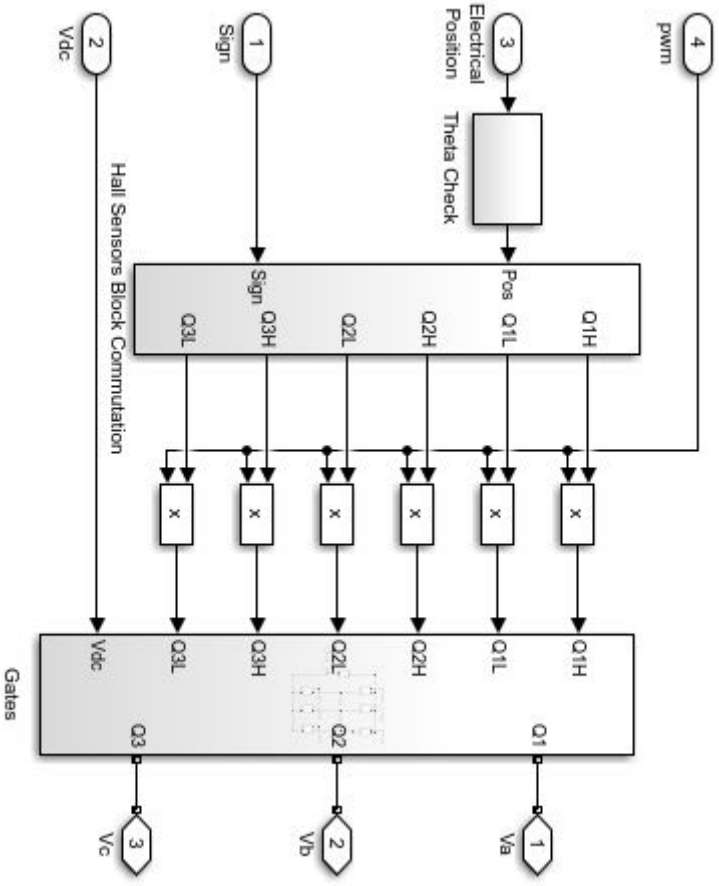

FIGURE C.1: Six-step inverter block

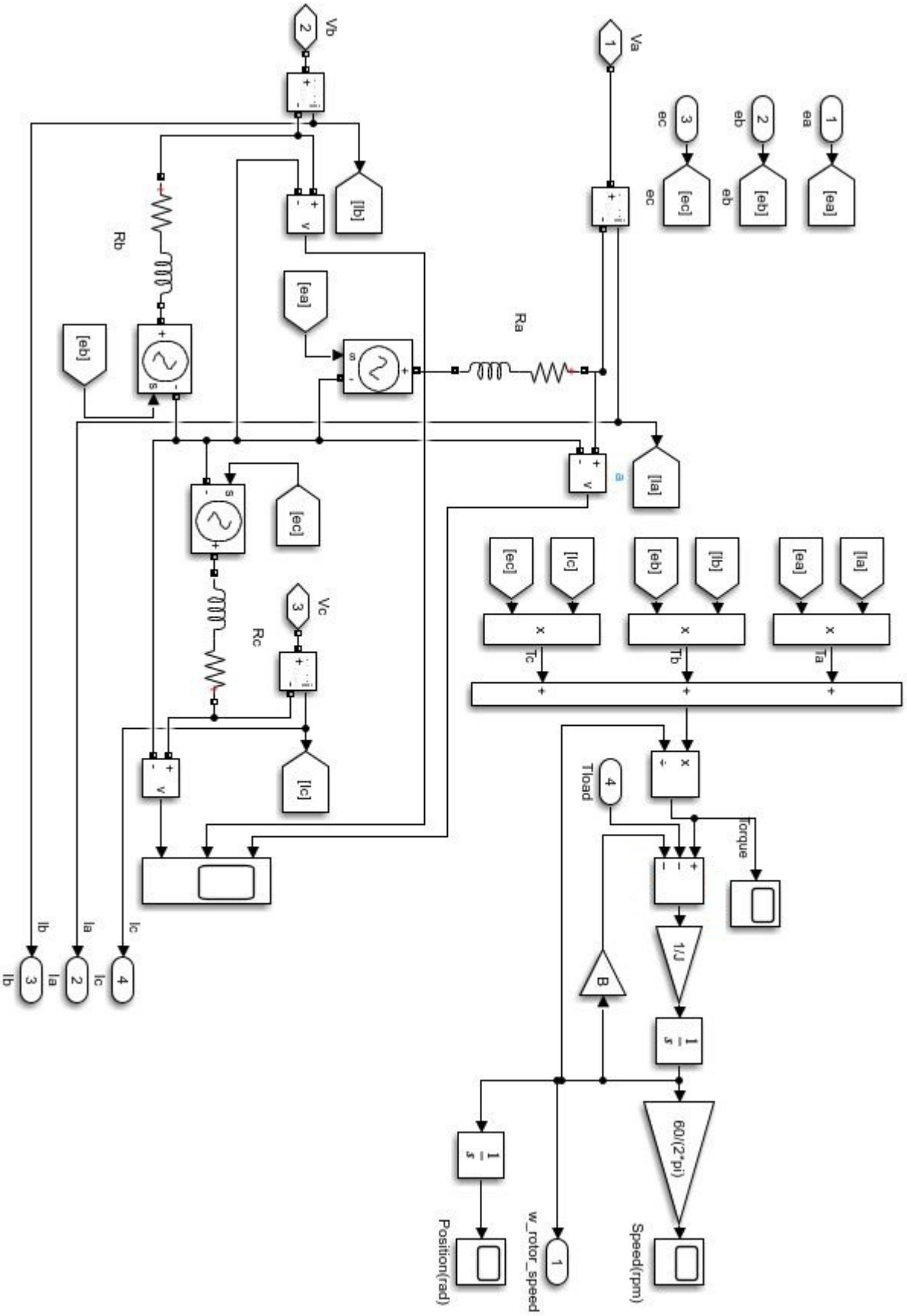

FIGURE C.2: BLDC actuator block

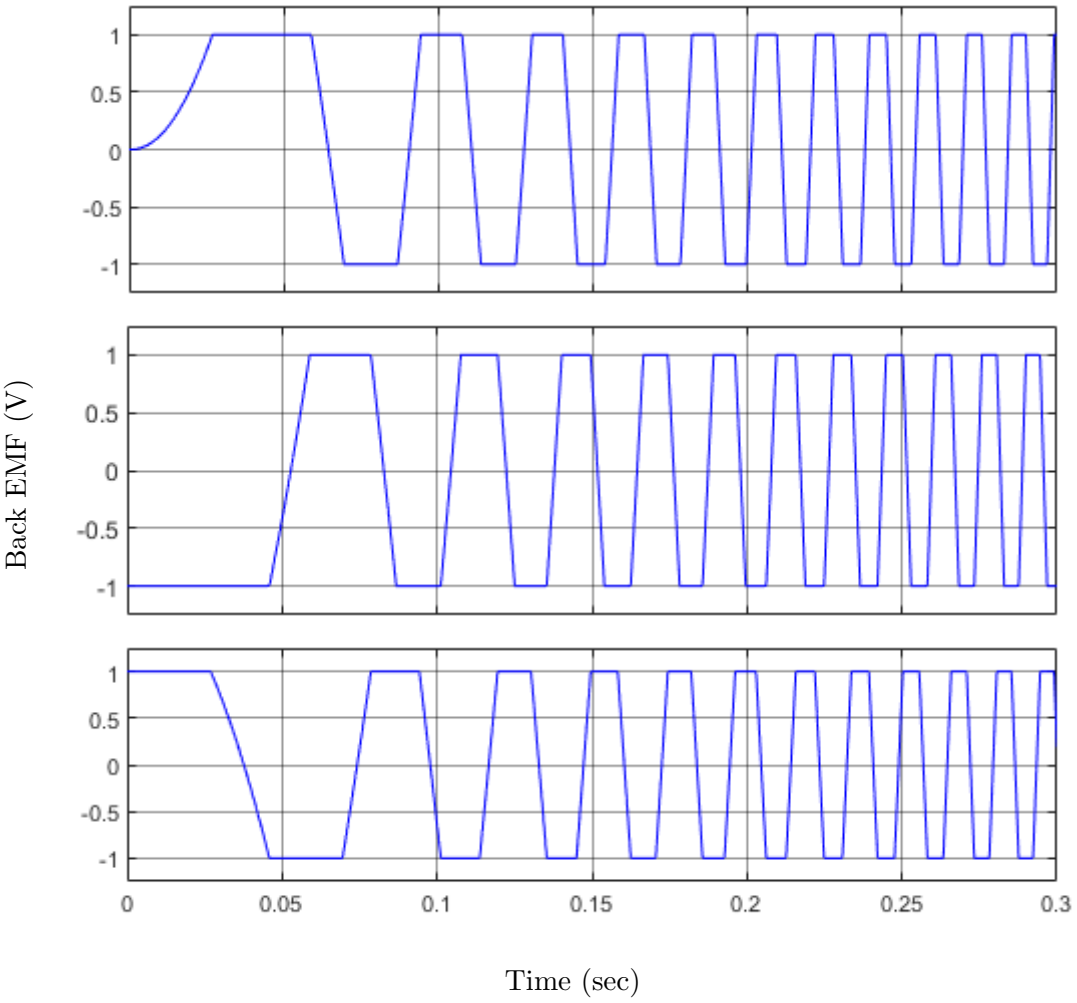

FIGURE C.3: Back EMF output

Bibliography

Aircav (2008). General dynamics f-16. [online] Retrieved from:https://www.aircav.com/recog/chp05/ch05aclist/f-16.html. [Accessed: 2022-05-01].

Althaffathan, M. (2019). Missile system. [online] Retrieved from: https://www.toppng.com/freeimage/missileImages120677. [Accessed: 2022-07-08].

Åström, K. J. and Hägglund, T. (1984). Automatic tuning of simple regulators with specifications on phase and amplitude margins. *Automatica*, 20(5):645–651.

Aydogan, A., Hasturk, O., and Rogers, E. (2019). Robust h_∞ computed torque control of flexible joint tvc systems. *IFAC-PapersOnLine*, 52(12):454–459.

Aydogan, A., Rogers, E., and Hasturk, O. (2018). Dynamic modeling and computed torque control of flexure jointed tvc systems. In *Dynamic Systems and Control Conference*, volume 51913, page V003T35A001. American Society of Mechanical Engineers.

Azar, A. T. and Serrano, F. E. (2015). Design and modeling of anti wind up pid controllers. In *Complex System Modelling and Control Through Intelligent Soft Computations*, pages 1–44. Springer.

Balu, R., Marathe, A., Paul, P., and Mukunda, H. (1991). Analysis of performance of a hot gas injection thrust vector control system. *Journal of Propulsion and Power*, 7(4):580–585.

Baruh, H. (2015). *Applied dynamics*. CRC press, Boca Raton, FL.

Beaven, R., Wright, M., and Seaward, D. (1996). Weighting function selection in the h-infinity design process. *Control Engineering Practice*, 4(5):625–633.

Beck, C. (1991). Computational issues in solving lmis. In *[1991] Proceedings of the 30th IEEE Conference on Decision and Control*, pages 1259–1260.

Bellini, A., Figalli, G., and Ulivi, G. (1989). Sliding mode control of a direct drive robot. In *Conference Record of the IEEE Industry Applications Society Annual Meeting*, pages 1685–1692. IEEE.

Biovia (2018). Solidworks, San Diego: Dassault systemes. [online] Retrieved from: https://3ds.com/products-services/biovia/products. [Accessed: 2018-01-15].

Cameron, J. M. and Book, W. J. (1997). Modeling mechanisms with nonholonomic joints using the Boltzmann-Hamel equations. *The International Journal of Robotics Research*, 16(1):47–59.

Canudas-de Wit, C., Siciliano, B., and Bastin, G. (1997). *Theory of robot control*. Springer, New York, NY.

Cao, Y. Y., Lin, Z., and Ward, D. (2002). An anti-wind up approach to enlarging domain of attraction for linear systems subject to actuator saturation. *IEEE Transactions on Automatic Control*, 47(1):140–145.

Chen, Y., Ma, G., Lin, S., and Gao, J. (2012). Adaptive fuzzy computed-torque control for robot manipulator with uncertain dynamics. *International Journal of Advanced Robotic Systems*, 9(6):237.

Chung, W., Fu, L.-C., and Hsu, S.-H. (2008). *Motion control*, pages 133–159. Springer Handbook of Robotics, New York, NY.

Chunguang, W., Guiyang, X., and Jianliang, G. (2020). Buckling instability of flexible joint under high pressure in solid rocket motor. *International Journal of Aerospace Engineering*, 2020.

Cline, D. (2021). Hamilton's Action Principle. [online] Retrieved from: https://phys.libretexts.org/@go/page/14199. [Accessed: 2021-05-16].

Cohen, G. (1953). Theoretical consideration of retarded control. *Transactions of the American Society of Mechanical Engineers*, 75:827–834.

Craig, J. J. (1986). *Introduction to Robotics: Mechanics and Control*. Addison-Wesley, Boston, MA.

Diaz, F., Dominguez, O., and Ramos-Velasco, L. E. (2012). Sliding computed torque control based on passivity for a haptic device: Phantom premium 1.0. In *World Automation Congress 2012*, pages 1–6. IEEE.

Dibenedetto, E. (2011). *Classical mechanics: theory and mathematical modeling*. Springer, New York, NY.

Doyle, J., Packard, A., and Zhou, K. (1991). Review of lfts, lmis, and μ. *Proceedings of the 30th IEEE Conference on Decision and Control*.

Duan, G.-R. and Yu, H.-H. (2013). *LMIs in control systems analysis, design and applications*. CRC press.

Elegante, T. and Bowman, R. (2012). *Nozzle fabrication for the Space Shuttle Solid Rocket Motor*. AIAA, Las Vegas, NV.

Ensworth, C. (2013). Thrust vector control for nuclear thermal rockets. In *49th Propulsion and Control Systems Conference*, page 4075. American Institute of Aeronatics and Astronautics.

etechnog.com (2021). Potentiometer diagram. [online] Retrieved from: https://www.etechnog.com/2021/07/potentiometer-diagram-symbol-construction.html. [Accessed: 2022-06-09].

Facciano, A. B., Sybold, K. G., Westberry-Kutz, T. L., and Widmer, D. O. (1999). Jet vane control system prototype hardware development for the evolved seasparrow missile. Technical report, Raytheon Missile Systems.

Gahinet, P. and Apkarian, P. (1994). A linear matrix inequality approach to h-infinity control. *International journal of robust and nonlinear control*, 4(4):421–448.

Galeani, S., Tarbouriech, S., Turner, M., and Zaccarian, L. (2009). A tutorial on modern anti-windup design. In *2009 European Control Conference*, pages 306–323.

Ghrab, N. and Kallel, H. (2013). Comparative study between robust control of robotic manipulators by static and dynamic neural networks. *International Scholarly Research Notices*, 2013.

Goodwin, G. C., Graebe, S. F., Salgado, M. E., et al. (2000). *Control system design*, volume 240. Prentice Hall, Hoboken, NJ.

Han, S. M. and Benaroya, H. (2002). *Nonlinear and stochastic dynamics of compliant offshore structures*, volume 98. Springer Science & Business Media, New York, NY.

Helton, J. W. and Merino, O. (1998). *Classical control using H-infinity methods: theory, optimization, and design*. SIAM.

Herbert, J. T. and Reinhardt, C. M. (1974). Thrust vector control flex joints commercial applications. *SAE Transactions*, pages 2912–2920.

Hibbeler, R. C. (2004). *Engineering mechanics: dynamics*. Pearson Education.

Hu, J., Bohn, C., and Wu, H. (2000). Systematic h-infinity weighting function selection and its application to the real-time control of a vertical take-off aircraft. *Control Engineering Practice*, 8(3):241–252.

Huang, A.-C. and Chien, M.-C. (2010). *Adaptive control of robot manipulators: a unified regressor-free approach*. World scientific.

Iwasaki, T. and Skelton, R. E. (1994). All controllers for the general h-infinity control problem: Lmi existence conditions and state space formulas. *Automatica*, 30(8):1307–1317.

Jeon, C. H., Cheon, Y. J., Kim, J.-S., Lee, J., and Sung, S. W. (2010). Relay feedback methods combining sub-relays to reduce harmonics. *Journal of Process Control*, 20(2):228–234.

Jiméneze, A. and Icaza, D. (2000). Thrust vectoring system control concept. *IFAC Proceedings Volumes*, 33(6):235–244.

Kasabov, N. K. (1996). *Foundations of neural networks, fuzzy systems, and knowledge engineering*. MIT Press, Cambridge, MA.

Kim, Y. H., Lewis, F. L., and Dawson, D. M. (2000). Intelligent optimal control of robotic manipulators using neural networks. *Automatica*, 36(9):1355–1364.

Kolhe, J. P., Shaheed, M., Chandar, T., and Talole, S. (2013). Robust control of robot manipulators based on uncertainty and disturbance estimation. *International Journal of Robust and Nonlinear Control*, 23(1):104–122.

Lampani, L., Angelini, F., Bernabei, M., Marocco, R., Fabrizi, M., and Gaundenzi, P. (2012). Robust control of robot manipulators based on uncertainty and disturbance estimation. *The Journal of Aerospace Science, Technology and Systems*, 91(1):2.

Lazić, D. V. and Ristanović, M. R. (2007). Electrohydraulic thrust vector control of twin rocket engines with position feedback via angular transducers. *Control Engineering Practice*, 15(5):583–594.

Lewis, F. L., Dawson, D. M., and Abdallah, C. T. (2003). *Robot manipulator control: theory and practice*. CRC Press, Boca Raton, FL.

Li, Y., Lu, H., Tian, S., Jiao, Z., and Chen, J.-T. (2011). Posture control of electromechanical-actuator-based thrust vector system for aircraft engine. *IEEE Transactions on Industrial Electronics*, 59(9):3561–3571.

Löfberg, J. (2012). Automatic robust convex programming. *Optimization Methods and Software*, 27(1):115–129.

Lu, H., Li, Y., Tian, S., and Nie, Z. (2010). Improved hybrid robust control method for the electromechanical actuator in aircrafts. *Chinese Journal of Mechanical Engineering*, 23(4):443–450.

Ma, K. and Ghasemi-Nejhad, M. N. (2005). Precision positioning of a parallel manipulator for spacecraft thrust vector control. *Journal of Guidance, Control, and Dynamics*, 28(1):185–188.

Melo, J. I. G., Caicedo, J. D. P., and Miyagi, P. E. (2013). Design consideration and kinematic development of a thrust vector control system for a liquid propellant rocket. In *International Congress of Mechanical Engineering. Brazil, ABCM.*

Mohan, C. R., Ramanathan, J., Kumar, S., and Gupta, A. (2011). Characterisation of materials used in flex bearings of large solid rocket motors. *Defence Science Journal*, 61(3):264.

Morin, D. (2008). *Introduction to classical mechanics: with problems and solutions*. Cambridge University Press.

Nguyen-Tuong, D., Seeger, M., and Peters, J. (2008). Computed torque control with nonparametric regression models. In *2008 American Control Conference*, pages 212–217. IEEE.

Pham, D., Ghanbarzadeh, A., Koc, E., Otri, S., Rahim, S., and Zaidi, M. (2005). The bees algorithm technical note. *Manufacturing Engineering Centre, Cardiff University, UK*.

Pictures, A. (2019). Royal Air Force Panavia Tornado, jet deflector. [online] Retrieved from: http://www.airplane-pictures.net/photo/74613/zd793-uk-air–panavia-tornado-gr-4-4. [Accessed: 2019-04-09].

Prattico, F., Dzahir, M. A. M., and Yamamoto, S.-i. (2014). Computed-torque method for the control of a 2 dof orthosis actuated through pneumatic artificial muscles: a specific case for the rehabilitation of the lower limb. *Medical Physics*.

Prescott, B. and Macocha, M. (1996). Nozzle design. *Progress in Astronautics and Aeronautics*, 170:137–187.

Rahmani, M. and Ghanbari, A. (2016). Computed torque control of a caterpillar robot manipulator using neural network. In *Advanced Engineering Forum*, volume 15, pages 106–118. Trans Tech Publ.

Sabet, S., Dabiri, A., Armstrong, D. G., and Poursina, M. (2017). Computed torque control of the stewart platform with uncertainty for lower extremity robotic rehabilitation. In *2017 American Control Conference*, pages 5058–5064. IEEE.

Sahin, M. (2022). Optimization of model predictive control weights for control of permanent magnet synchronous motor by using the multi objective bees algorithm. *Model-Based Control Engineering: Recent Design and Implementations for Varied Applications*, page 75.

Salloum, R., Arvan, M. R., and Moaveni, B. (2016). Identification, uncertainty modeling and robust controller design for an electromechanical actuator. *Proceedings of the Institution of Mechanical Engineers, Part C: Journal of Mechanical Engineering Science*, 230(20):3631–3641.

Schaefermeyer, M. R. (2011). *Aerodynamic thrust vectoring for attitude control of a vertically thrusting jet engine*. All Graduate Theses and Dissertations. 1237.

Schinstock, D. E., Scott, D. A., and Haskew, T. A. (1998). Modeling and estimation for electromechanical thrust vector control of rocket engines. *Journal of Propulsion and Power*, 14(4):440–446.

Seborg, D. E., Edgar, T. F., Mellichamp, D. A., and Doyle III, F. J. (2016). *Process dynamics and control*. John Wiley and Sons, New York, NY.

Shang, W.-W., Cong, S., and Ge, Y. (2012). Adaptive computed torque control for a parallel manipulator with redundant actuation. *Robotica*, 30(3):457–466.

Shi, J., Liu, H., and Bajçinca, N. (2008). Robust control of robotic manipulators based on integral sliding mode. *International Journal of Control*, 81(10):1537–1548.

Skogestad, S. and Postlethwaite, I. (2005). *Multivariable feedback control: analysis and design*. john Wiley & sons.

Söğütcü, B. and Sümer, B. (2019). Experimental and numerical investigation of a jet vane of thrust vector control system. In *AIAA Propulsion and Energy 2019 Forum*, page 3880.

Sommerfeld, A. (1952). *The Lectures on Theoretical Physics*. Academic Press, Cambridge, MA.

Sparkfun (2021). Rotary potentiometer. [online] Retrieved from: https://www.sparkfun.com/products/9939. [Accessed: 2022-05-06].

Spong, M. W., Hutchinson, S., and Vidyasagar, M. (2006). Robot modeling and control. *Industrial Robot: An International Journal*.

Spong, M. W. and Vidyasagar, M. (2008). *Robot dynamics and control*. John Wiley and Sons, New York, NY.

Stobart, R., Kuperman, A., and Zhong, Q.-C. (2011). Uncertainty and disturbance estimator–based control for uncertain lti-siso systems with state delays. *Journal of Dynamic Systems, Measurement, and Control*, 133(2).

Sutton, G. P. and Biblarz, O. (2016). *Rocket propulsion elements*. John Wiley and Sons, Hoboken, NY.

Swain, D., Biswal, S. K., Thomas, B. P., Babu, S. S., and Philip, J. (2019). Performance characterization of a flexible nozzle system (fns) of a large solid rocket booster using 3-d dic. *Experimental Techniques*, 43(4):429–443.

Udawatta, L., Watanabe, K., Izumi, K., and Kiguchi, K. (2003). Control of underactuated robot manipulators using switching computed torque method: Ga based approach. *Soft Computing*, 8(1):51–60.

Wang, Q.-G., Lee, T. H., and Chong, L. (2002). *Relay feedback: analysis, identification and control*. Springer Science and Business Media.

wikimedia.org (2021). TVC system, f-16. [online] Retrieved from: https://commons.wikimedia.org/wiki/File:F-16-3-Yokota-Tokyo.jpg. [Accessed: 2021-07-25].

Wikipedia (2021a). The Poznan museum of armaments, poland. [online] Retrieved from: https://en.wikipedia.org/wiki/Scudmissile. [Accessed: 2021-05-16].

Wikipedia (2021b). Jet vane mechanism, v-2 missile. [online] Retrieved from: https://en.wikipedia.org/wiki/V-2-rocket. [Accessed: 2021-07-19].

Willsky, A. S. and Young, I. T. (1997). *Signals and systems*. Prentice-Hall International.

wired.com (2019). Rocket test preperations, jet vane. [online] Retrieved from: https://www.wired.com/2011/12/rocket-test-preparations. [Accessed: 2019-04-09].

Woodberry, R. (1975). Flexible joints for thrust vector control. In *11th Propulsion Conference*, page 1221.

Yu, B. and Shu, W. (2017). A novel control approach for a thrust vector system with an electromechanical actuator. *IEEE Access*, 5:15542–15550.

Yuce, B., Packianather, M. S., Mastrocinque, E., Pham, D. T., and Lambiase, A. (2013). Honey bees inspired optimization method: the bees algorithm. *Insects*, 4(4):646–662.

Zelei, A., Kovács, L. L., and Stépán, G. (2011). Computed torque control of an under-actuated service robot platform modeled by natural coordinates. *Communications in Nonlinear Science and Numerical Simulation*, 16(5):2205–2217.

Ziegler, J. G., Nichols, N. B., et al. (1942). Optimum settings for automatic controllers. *trans. ASME*, 64(11):12–20.